รายงานวิจัยฉบับสมบูรณ์

โครงการ สมบัติเชิงแสงของจุดควอนตัมที่เรียงเป็นแนวเส้นตรง

OPTICAL PROPERTIES OF LINEARLY ALIGNED QUANTUM DOTS

โดย อาจารย์ ดร. ชนินทร์ วิศวินธานนท์ และคณะ

กรกฎาคม ๒๕๕๒

สัญญาเลขที่ MRG4880160

รายงานวิจัยฉบับสมบูรณ์

โครงการ สมบัติเชิงแสงของจุดควอนตัมที่เรียงเป็นแนวเส้นตรง

OPTICAL PROPERTIES OF LINEARLY ALIGNED QUANTUM DOTS

คณะผู้วิจัย	สังกัด
1. อาจารย์ ดร.ชนินทร์ วิศวินธานนท์	**จุฬาลงกรณ์มหาวิทยาลัย**
2. ศาสตราจารย์ ดร.สมศักดิ์ ปัญญาแก้ว	**จุฬาลงกรณ์มหาวิทยาลัย**
3. นายศุภโชค ไทยน้อย	**จุฬาลงกรณ์มหาวิทยาลัย**
4. **นายพรชัย ช่างม่วง**	**จุฬาลงกรณ์มหาวิทยาลัย**
5. **นางสาวนันทิดา ชิตสเว**	**จุฬาลงกรณ์มหาวิทยาลัย**
6. **นางสาวสุวารี สุรประภาพิชย์**	**จุฬาลงกรณ์มหาวิทยาลัย**

สนับสนุนโดย สำนักงานคณะกรรมการการอุดมศึกษา และสำนักงานกองทุนสนับสนุนการวิจัย

(ความเห็นในรายงานนี้เป็นของผู้วิจัย สกอ. และ สกว. ไม่จำเป็นต้องเห็นด้วยเสมอไป)

Acknowledgements

The researchers of this project would like to acknowledge Office of the Higher Education Commission (OHEC) and Thailand Research Fund (TRF) for their main financial support to this project. The researchers also would like to thank the Japan International Cooperation Agency (JICA) for ASEAN University Network / South-East Asia Engineering Education Development Network (AUN/SEED-Net), Asian Office for Aerospace Research and Development (AOARD) of the Air Forces of the United States of America, National Nanotechnology Center (NANOTEC) of Thailand, Chulalongkorn University, and University of Tokyo, for their subsidiary financial support and cooperation.

บทคัดย่อ

รหัสโครงการ: MRG4880160

ชื่อโครงการ: สมบัติเชิงแสงของจุดควอนตัมที่เรียงเป็นแนวเส้นตรง

ชื่อนักวิจัย: อาจารย์ ดร.ชนินทร์ วิศวินธานนท์ (จุฬาลงกรณ์มหาวิทยาลัย) และคณะ

ที่อยู่อีเมล: Chanin.W@chula.ac.th

ระยะเวลาโครงการ: 1 มิถุนายน 2548 – 31 พฤษภาคม 2550

โครงการวิจัยนี้มีวัตถุประสงค์คือ เพื่อศึกษาสมบัติเชิงแสงของโครงสร้างจุดควอนตัมที่เรียงกันเป็นเส้นตรงในแนวข้าง 3 แบบ ได้แก่ จุดควอนตัมคู่ จุดควอนตัมที่เรียงกันเป็นเส้นตรง และจุดควอนตัมที่เรียงกันเป็นเส้นตารางไขว้ โดยเน้นศึกษาสมบัติด้านโพลาไรเซชันเชิงแสงของโครงสร้างดังกล่าวเป็นสำคัญ โดยวิเคราะห์สมบัติดังกล่าวทั้งจากการคำนวณทางทฤษฎี และจากการวัดสเปกตรัมการเปล่งแสงของชิ้นงานตัวอย่าง ผลการคำนวณพบว่าหากจุดควอนตัมอยู่ใกล้กันมากขึ้น จุดควอนตัมมีขนาดเล็กลง และ/หรือจุดควอนตัมเรียงกันเป็นจำนวนมากขึ้น จะส่งผลให้ระดับขั้นโพลาไรเซชันเชิงเส้น (degree of linear polarization) ยิ่งมีค่าเพิ่มขึ้น แต่ในกรณีที่เป็นจุดควอนตัมโดด ระดับขั้นโพลาไรเซชันจะขึ้นอยู่กับสัณฐานของจุดควอนตัม เช่น ถ้าจุดควอนตัมมีสัณฐานเป็นทรงรีในทิศทางใดทิศทางหนึ่ง แสงที่เปล่งออกมาจากจุดควอนตัมนั้นๆ ก็อาจมีค่าระดับขั้นโพลาไรเซชันที่ไม่เป็นศูนย์ได้ ผลการทดลองพบว่า ระดับขั้นโพลาไรเซชันของจุดควอนตัมคู่และจุดควอนตัมที่เรียงกันเป็นเส้นตรงมีค่าเปลี่ยนไปตามอุณหภูมิ พฤติกรรมเช่นนี้อธิบายได้ว่าเป็นผลเนื่องจากการคู่ควบกัน (coupling) ของจุดควอนตัม แต่ค่าระดับขั้นโพลาไรเซชันที่วัดได้จากจุดควอนตัมที่เรียงกันเป็นเส้นตารางไขว้ไม่ขึ้นกับอุณหภูมิ ซึ่งเมื่อศึกษาภาพถ่ายจากกล้องจุลทรรศน์ชนิดแรงอะตอม (atomic-force microscope) พบว่าจุดควอนตัมในชิ้นงานตัวอย่างชนิดนี้เรียงกันเป็นแถวยาว แต่จุดควอนตัมไม่อยู่ใกล้กันเพียงพอที่จะก่อให้เกิดการคู่ควบกัน แสดงว่าค่าระดับขั้นโพลาไรเซชันที่เกิดขึ้นนั้นมีสาเหตุมาจากสัณฐานที่ไม่เป็นเอกรูป (non-uniform) ของจุดควอนตัมแต่ละจุด การศึกษาเปรียบเทียบและวิเคราะห์ผลที่รวบรวมได้เหล่านี้ทำให้เราเข้าใจฟิสิกส์ของสมบัติโพลาไรเซชันเชิงแสงของโครงสร้างระดับนาโนเมตรเหล่านี้ได้ดียิ่งขึ้น ซึ่งจะเป็นองค์ความรู้พื้นฐานส่วนหนึ่งที่จะนำไปสู่การประดิษฐ์สิ่งประดิษฐ์ทางแสงที่มีประสิทธิภาพสูงสำหรับโลกในยุคนาโนเทคโนโลยีต่อไป.

คำสำคัญ: จุดควอนตัม การปลูกผลึกด้วยลำโมเลกุล การเปล่งแสง ระดับขั้นโพลาไรเซชันเชิงเส้น การคู่ควบ

Abstract

Project Code: MRG4880160

Project Title: Optical Properties of Linearly Aligned Quantum Dots

Principal Investigator: Chanin Wissawinthanon (Chulalongkorn University) ***et al.***

E-mail Address: Chanin.W@chula.ac.th

Project Period: 1 June 2005 – 31 May 2007

This project was aimed to investigate the optical properties—emphasizing on the linear optical polarization property—of three kinds of quantum dot (QD) structures, namely, binary quantum dots (bi-QDs), linearly aligned quantum dots (LAQDs), and QDs aligned on a cross-hatch pattern. Such property was investigated by means of photoluminescence spectroscopy as well as theoretical calculation. It was found out from calculation that linear polarization degree (PD) of the LAQDs strongly depends on spacing, size, and number of QDs in the alignment. In particular, closer spacing, smaller dot size, or more number of QDs in the alignment gives rise to a higher PD value. For isolated QDs, the extent of shape isotropy strongly affects the PD. In the experimental point of view, optical properties of the three kinds of structures were investigated by means of temperature-dependent-, excitation-power-dependent-, and polarization-resolved photoluminescence spectroscopy. Measurements on a bi-QD sample and two LAQD samples reveal that the temperature-dependent PD for these nanostructures originates from coupling among the QDs. On the other hand, QDs on a cross-hatch pattern did not show the temperature-dependent behavior; the amount of PD that was observed for this type of sample merely comes from the shape anisotropy of individual QDs. By comparing these results, the physics behind the observed behaviors of these nanostructures is better understood and this will help produce higher-efficiency devices for the era of nanotechnology.

Keywords: quantum dot, molecular-beam epitaxy, photoluminescence, linear optical polarization degree, coupling

TABLE OF CONTENTS

Page

Page

CHAPTER I

INTRODUCTION

1.1 Background

The late years of the twentieth century, years of evolution of science and technology, was filled with new things in the view point of physics and device application technology. In this event, semiconductors played as the heart of the evolution, and silicon has still remained its champion [1]. In the past and during these days, silicon technology is very influential in electronic device industry and most of the electronic devices are based on silicon. At the same time, the material and device technology has attained an amazing degree of sophistication. However, silicon's indirect bandgap nature and the poor efficiency of producing light emission are a significant difficulty for making optoelectronic devices from this material [2]. Silicon photodetectors are available in the market but they still have some disadvantages to be used at the present fiber-optic communication wavelengths [3]. There are some tremendous efforts to achieve light emission from engineered silicon structures [4]; the effective achievement is still very far from the technological point of view. It seems that the silicon technology and nowadays optoelectronic and photonic technology are not significantly matched to each other. Therefore, searching for suitable materials for optoelectronic devices became crucial in the optoelectronic technology.

Some interesting materials have been proved to be good for photonic or optoelectronic devices. Among these, GaAs and other III-V compound semiconductors, such as InAs and InP, have gained considerable attentions from the researchers due to their efficient coherent light emission property [5]. Nowadays, GaAs technology has become in full bloom and produced quite a good number of optoelectronic and electronic devices. The most important area of applications of optoelectronic devices is in fiber-optic communications, in which 1.3 μm and 1.55 μm are the chosen wavelengths [6]. In view of this, the quaternary alloy $In_{1-x}Ga_xAs_yP_{1-y}$ lattice-matched to InP [7] is applicable for making lasers, while ternary InGaAs lattice-matched to InP is employed in photodetectors [8].

The new direction for semiconductor material science and technology started from the development of MBE and MOCVD techniques [9-10]. The more popular

these fabrication techniques became, the less effort the scientists and engineers spent to search for novel and suitable materials. Instead of seeking new materials for new applications and for new wavelength ranges, now one tries to use various combinations of materials, control their composition and thickness, or synthesize new materials. The word "bandgap engineering" has become crucial, and almost all modern devices are the product of this technology. Both lattice-matched and lattice-mismatched pairs are now routinely grown, and thus it is difficult to say which material combination has which specific properties and is useful for which application. After that, scaling consideration became significant in the fabrication history. Reducing the device scale into a nanometer range results in a significant progress in the device applications. Semiconductor "nanostructures" have thus become crucial in nowadays technology.

1.2 Quantum Dots: the Artificial Atoms

In the last two decades, a new direction of modern research in physics and technology, broadly defined as "nanoscale science and technology", has been developed. Doing many research and studying new things in nanotechnology has revealed the new properties of matters, from bulk to the "quantum dot", together with the contemporary development of relevant device applications. The trend of reducing the size is typical of microelectronic industry, whose target is the fabrication of devices with fast working speed, low power consumption, and reduction of the occupied volume with high efficiency.

The fabrication, characterization and manipulation of nanometre-scale devices, so-called "quantum dot (QD) structures", is based on the three-dimensional quantum confinement of semiconductors with a lower energy bandgap E_g surrounded by higher-E_g materials [11]. A pronounced property of the QD is its formation of completely discrete quantum energy levels. The achievement of this structure is a clear example of the miniaturization approach in micro- and opto-electronics. The top-down fabrication method [12] and the bottom-up fabrication approach [13] lead to an achievement of very similar nano-objects whose optical and electronic properties are determined by the same quantum mechanical laws. Three-dimensional quantum confinement in semiconductors has been deeply investigated theoretically and experimentally [14]. Due to the discretized density of states of carriers inside

quantum dots, these objects are expected to bring significant progress, especially in optical and electronic device applications. The first predictions in 1982 by Arakawa and Sakaki about their application as active materials for semiconductor optical lasers and amplifiers suggested the possibility to obtain very high-gain, high-frequency operating devices with peculiar temperature stability [15]. Since then, numerous attempts have been performed in order to obtain defect-free quantum dots, whose structural, electronic, and optical properties can be technologically controlled and with which devices can be fabricated reliably and reproducibly.

The top-down method is a direct extension of the already well-established quantum-well epitaxial growth technique to quantum-dot systems. QDs were generated by localizing nanometer-size regions of quantum wells either by depleting the charges into the surrounding regions with electrostatic fields or by physically removing the neighboring heterostructure with etching procedures. Although many of the predicted properties were experimentally verified, such quantum dots were not suitable for the fabrication of most optoelectronic devices due to the high density of surface states created during the lithography and etching steps [16]. A breakthrough in the field of epitaxially grown nanostructures [17] was a possibility to control the growth conditions under which defect-free islands were formed onto mismatched or strained-layers based on III–V compound semiconductors. The optical properties of "undesired" clusters of InAs located on GaAs layers showing an intense and sharp photoluminescence revealed their quantum-dot-like behavior, and at present these self-organized or self-assembled islands have become the material of choice for the realization of novel optoelectronic devices.

1.3 Ordered Quantum Dots

Ordered QDs are of considerable contemporary interest due to their potential electronic and optoelectronic device applications [18]. Vertically aligned QDs are almost perfect in the view point of fabrication technology [19-20] while lateral alignment of QDs during self-assembly process is much less pronounced. Since laterally ordered QDs have been investigated through several mechanisms by many research groups [20-22], some technical limitation due to complexity of multiple processes and crystallographic defects has caused this type of structures to have degraded optical quality, and thus there is a delay in getting the laterally aligned QDs

with better optical quality. The important issue in ordered QD development is the design of the structure to produce more radiative photons even at room temperature, hence reducing the intensity loss due to non-radiative channels. The bottom-up or self-assembled approach is simple and defect-free to get good optical quality QDs. But in this method of growth on planar substrates, the QDs occur in the planar layers in a random manner. By modifying the standard growth technique, self-assembled laterally ordered QDs with high luminescence and narrow linewidth even at room temperature may be achieved. To obtain ordered quantum dots, two different methods are introduced in the fabrication technology: one is in which QDs are grown by varying growth parameters, and the other is in which QDs are grown on virtual substrates. Both of these techniques were used to grow the laterally aligned QDs investigated in this project work, and the detailed fabrication procedure will be discussed when relevant.

1.4 Ordered QDs for Quantum-Dot-Based Photonic Devices

Since the interest toward the three-dimensional quantum-confined semiconductor QDs was arisen from the need to improve the performance of semiconductor quantum-well lasers, most of the scientific and technological efforts in the past decades were addressed to the development of quantum-dot laser sources. In about ten years of research from the first demonstration of lasing at cryogenic temperatures, the quality of quantum-dot edge-emitting lasers has reached, and for several aspects overcome, quantum-well lasers, showing low thermal dependence of the threshold, high gain, high power emission, operation at room temperature with wavelength emission matching the critical telecommunication spectral windows around 1.3 μm and 1.55 μm [23-24]. Moreover, quantum-dot vertical cavity surface-emitting lasers (VCSELs) were also demonstrated at λ_{em} = 1.3 μm [25], owing to the possibility to grow fully epitaxial distributed Bragg reflectors exploiting alternate materials with high index contrast and low reticular mismatch (conditions not achievable with InP and InP compounds, the only materials used for emission in the second spectral window before the advent of QDs). The potential of GaAs-based quantum-dot lasers in replacing the more expensive InP-based quantum-well lasers is then clearly visible. Moreover, it is also worth mentioning different photonic devices such as surface-emitting quantum-dot inter-subband light sources and quantum-dot infrared (IR) photodetectors [26-27], which have been recently demonstrated. Although the benefits of self-assembled QDs have

been demonstrated in many photonic device applications, their random sizes and distributions give some difficulties in making a better device with better performance. For many practical applications, nanometer-scale QDs should be formed with a uniform size, well-controlled position, and uniform distribution. Believed to be able to improve the performance of some photonic devices like quantum-dot lasers and quantum-dot infrared photodetectors, ordered, coupled quantum dots have nowadays become of contemporary interest. For example, employing ordered quantum dots in photonic crystals was expected to make fabrication of such light-emitting photonic devices easier than utilizing randomly distributed quantum dots, while simultaneously boosting up the device performance [28-30].

1.5 Objectives

This project was aimed to study the optical properties of three kinds of laterally aligned quantum dots—binary quantum dots (bi-QDs), linearly aligned quantum dots (LAQDs), and QDs aligned on a cross-hatch pattern—which are self-assembly grown by various molecular-beam-epitaxial techniques. The research work was divided into two main parts: The first part emphasized on the optical properties of laterally aligned quantum dots from the theoretical point of view. The second part dealt with the investigation of laterally aligned quantum dots from the experimental point of view.

1.6 Scope of Work

To achieve the objectives mentioned above, first, the mathematical model of laterally aligned quantum-dot system was built up to be used in solving the Schrödinger equation and then specific computer programs were developed to solve such equation.

Experimental measurements were performed to obtain some optical properties, focusing on the linear polarization property, of photoluminescence (PL) from the laterally aligned quantum dots and then the experimental results were compared with theoretical ones.

This research also covered a study of the ground-state energy splitting of laterally aligned QDs which was the starting point of the polarization behavior.

1.7 Research Methodology

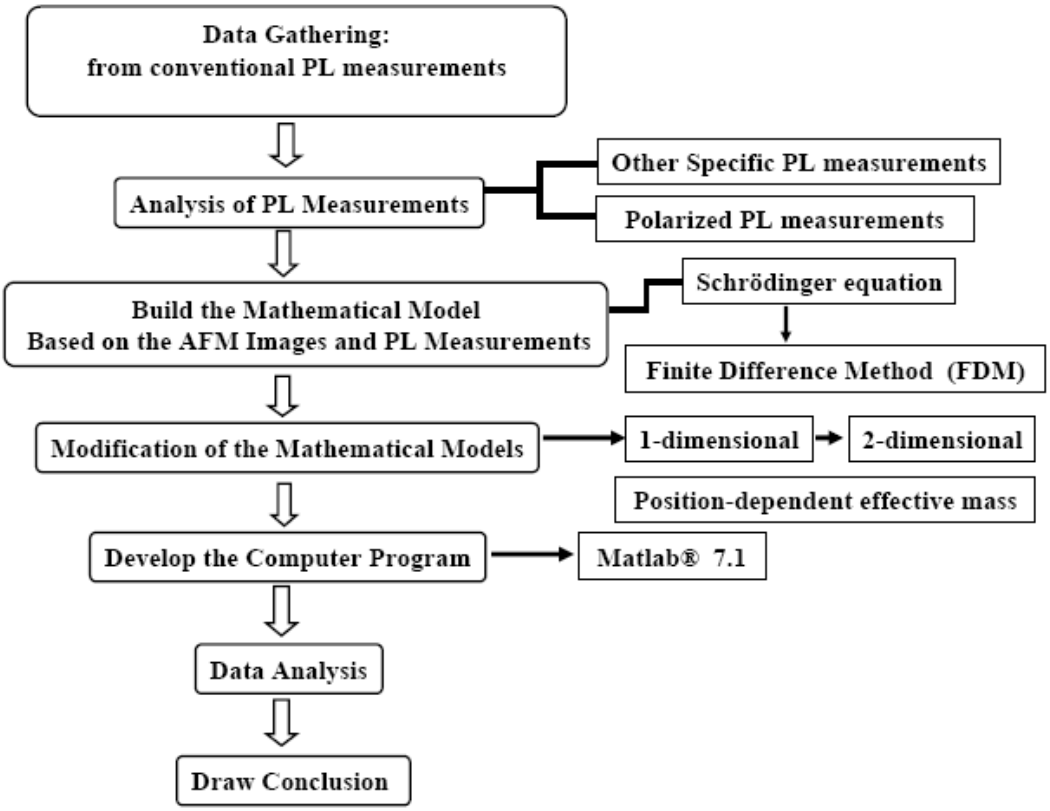

1.8 Significance of the Research

This research work investigated optical properties, focusing on the linear polarization property of laterally aligned quantum dots which is important for the polarization-sensitive photonic devices based on III-V semiconductor quantum dots.

1.9 Work Presented in This Report

In this report, the theoretical and experimental characterizations of laterally aligned QDs epitaxially grown by molecular-beam epitaxy (MBE) are presented. The polarization property of various laterally aligned quantum dot structures was investigated. This work proposed an idea of utilizing the polarization property of laterally aligned quantum dots for photonic device applications and proved that the polarization property and optical properties of the aligned quantum dots may be enhanced by optimizing the design and fabrication method.

In Chapter II, an overview of the physical properties of quantum dots is presented. In particular, the main characteristics and drawbacks of QDs grown by epitaxial techniques and their optical properties are highlighted. Chapter III concerns with theoretical calculations in which the finite-difference method is described and later on is used to solve the Schrödinger equation to eventually obtain the polarization characteristics of laterally aligned QDs. The theoretical characteristics of these quantum-dot systems are also discussed in detail. Chapter IV focuses on the spectroscopy and the associated macro-photoluminescence and micro-photoluminescence setups. The influence of the temperature, the excitation power and the structural effect on the optical properties of QDs are especially emphasized in that chapter. In Chapter V, the results obtained from optical characterization of various QD structures are presented. Such characterization is necessary and gives very useful information for future device designs and applications. The conclusion of this project is given in Chapter VI. Finally, the Appendix will deal with the main Matlab® program that was written and used in the theoretical part of this project.

CHAPTER II

LOW-DIMENSIONAL SEMICONDUCTOR NANOSTRUCTURES: QUANTUM CONFINEMENT AND ITS EFFECT ON OPTICAL PROPERTIES

2.1 Basic Concepts of Low-Dimensional Nanostructures

The content of this chapter deals with the dimensional confinement that affects the electronic and optical properties of semiconductor materials. One of the most noticeable characteristics of these semiconductor structures is delocalization of electrons that can spread their wavefunctions over a larger distance [31]. Over the past two decades, rapid progress in semiconductor fabrication technology, especially in the fabrication of nanostructures, has allowed semiconductor materials to be constructed with a confined electron structure. By reducing the size or dimension of a material into a micrometer and then to a nanometer scale of the order of the de Broglie wavelength of an electron, dramatic changes in electronic and optical properties were observed in these structures [32]. First, if one dimension is reduced into a nano-scale while the other dimensions remain large, then this structure is called a ***quantum well*** [33]. After that two dimensions are reduced while the other remains large, this structure is called a ***quantum wire*** [34]. The extreme case of this process is in which the size is reduced in all three dimensions into a nano-range, as a result, this structure is called a ***quantum dot*** [35]**,** and a donut-shaped quantum dot is called a ***quantum ring*** [36]. All these structures are associated with the name ***quantum*** because changes in electrical and optical properties of these structures after reducing their sizes arise from the quantum mechanical nature of physics as the consequences of the ultra small size. The electronic structures of bulk materials and atom-like nanostructures are different [37-38]. The electronic structures in the case of atom-like nanostructures are characterized by *discrete energy level*s while those of bulk crystal structures are characterized by *bands*. The density of states of bulk semiconductors and low-dimensional nanostructures may be calculated by using quantum mechanics. In that case the band offset between the low-dimensional nanostructures and the surrounding materials provide the energy potential to confine carriers [39-41].

To calculate the electronic states of bulk materials and nanostructures, the effective-mass approximation can effectively be used. The main assumption of the effective-mass approximation is that the envelope wavefunction does not significantly vary in the unit cell with a length scale of the nanostructure. This assumption can be applied to all low-dimensional nanostructures. Assuming the parabolic band dispersion, band-edge electron states of a semiconductor can then be described by the Schrödinger equation.

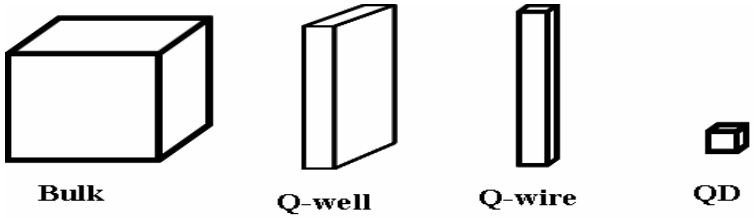

Figure 2.1 Progressive generation of rectangular nanostructures (After Ref. [37]).

Figure 2.2 Progressive generation of curvilinear nanostructures (After Ref. [37]).

Table 2.1 Quantum-confined behavior of semiconductor nanostructures.

Quantum structure	**Delocalization dimensions**	**Confinement dimensions**
Bulk	3(x,y,z)	0
Quantum well	2(x,y)	1(z)
Quantum wire	1(z)	2(x,y)
Quantum dot	0	3(x,y,z)

2.1 Bulk Material

In bulk, the conduction electrons are delocalized in a volume and their wavefunctions spread in three dimensions. By considering the electrons in bulk as free electron gas, the electrons are free to wander around the crystal without being influenced by the potential of the atomic nuclei. A free electron has a velocity v and a momentum $p = mv$. Its energy consists entirely of kinetic energy, and the potential energy tends to be zero ($V = 0$). Therefore, the total energy (E) of the bulk material can be considered as

$$E_{bulk} = E(k) = \frac{\hbar^2 k^2}{2m^*} \tag{2.1}$$

$$D_{bulk} = \frac{1}{2\pi^2}\left(\frac{2m^*}{\hbar^2}\right)^{\frac{3}{2}} E^{\frac{1}{2}} \tag{2.2}$$

where D is the density of states and k is electron wave number, $k = (k_x , k_y, k_z)$.

2.1.2 Quantum Wells

Quantum wells are a type of structure in which a thin layer of smaller-bandgap semiconductor is sandwiched between two layers of wider-bandgap semiconductors. The heterojunction between the smaller- and the wider-bandgap semiconductors forms a potential well confining the electrons and holes within the smaller-bandgap material region. So the electrons are quantized in the direction of confinement, say the z direction, and this becomes the model of particles in a one-dimensional box. The electronic energy levels in the other two dimensions are not discrete and are given by the effective-mass approximation as

$$E_{n,k_x,k_y} = E(c) + \frac{n^2\hbar^2}{8m_e^* l_z^2} + \frac{\hbar^2(k_x^2 + k_y^2)}{2m_e^*} \tag{2.3}$$

where $n = 1, 2, 3, \ldots$ are the quantum numbers, the first term $E(c)$ in the right-hand side is the energy corresponding to the bottom of the conduction band, the second term corresponding to the quantized energy, and the third term gives the kinetic

energy of the electron in the *x-y* plane in which electrons are free to move. The density of states for a quantum-well structure is given by

$$D_{Qwells}(E) = \frac{m}{\pi\hbar^2}\sum_i H(E - E_i) \tag{2.4}$$

where i = 1, 2, 3, …. and H (E-E_i) is the ***Heaviside's unit step*** function. It takes the value 0 when E is less than E_i, and 1 when E is equal to or greater than E_i. E_i is the i^{th} eigen-energy level within the quantum well.

2.1.3 Quantum Wires

Quantum wires represent two-dimensional confinements of electrons and holes. Such confinement permits free-electron behavior in only one direction, along the length of the wire, says, the *z* direction. For this reason, the system of quantum wires may be described as one-dimensional electron gas, where electrons are present in the conduction band. A quantum wire can be cylindrical with a circular cross section as well as rectangular or square in the lateral *x-y* plane. A representative model of a quantum wire here is a rectangular one with lateral dimensions l_x and l_y. The electronic energy levels of a quantum wire are given by

$$E_{n,k_x,k_y} = E(c) + \frac{n^2\hbar^2}{8m_e^* l_x^2} + \frac{n^2\hbar^2}{8m_e^* l_y^2} + \frac{\hbar^2 k_z^2}{2m_e^*} \tag{2.5}$$

The energy of the one-dimensional quantum wire consists of a sum of four parts. The first term is due to the continuous band value given by the effective-mass approximation. The second and the third terms mention the quantization of electrons in the confinement directions, and the fourth term gives the kinetic energy of the electron in the *z* direction where electron is free to move. For this case, the density of states is given by

$$D_{Qwires}(E) = \frac{1}{\pi}\left(\frac{2m}{\hbar^2}\right)^{\frac{1}{2}}\sum_i H\frac{n_i(E - E_i)}{(E - E_i)^{\frac{1}{2}}} \tag{2.6}$$

where once again, $H(E-E_i)$ is the Heaviside's unit step function, and n_i is the degeneracy factor. For quantum structures with dimensions lower than 2, it is possible for the same energy levels to occur for more than one arrangement of confined states. To account for this, a second factor $n_i(E)$ has been introduced.

2.1.4 Quantum Dots

A quantum dot represents the three-dimensional confinement of carriers; electrons and holes are confined in the three-dimensional quantum box, whose typical dimensions range from nanometers to tens of nanometers. The detail of the quantum dot will be discussed in next section. The electronic energy levels of the quantum dot are given by

$$E_n = \frac{\hbar^2}{8m_e^*}\left(\frac{n_x^2}{l_x^2}+\frac{n_y^2}{l_y^2}+\frac{n_z^2}{l_z^2}\right) \tag{2.7}$$

The density of states for the zero-dimensional quantum dot is

$$D_{Qdots}(E) = \sum_{E_n} \delta(E-E_n) \tag{2.8}$$

where δ (E-E_i) is the delta function (sharp peak) and $D(E)$ always has discrete values. A discrete value of $D(E)$ produces a sharp peak in the absorption and the emission spectrum of quantum dots even at room temperature. This kind of behavior is for the ideal case, however, due to other side effects, broadening of spectrum is generally observed in reality.

2.1.5 Quantum Rings

A quantum ring represents a donut-shaped quantum dot. It is similar to a quantum wire bent into a loop. A noticeable property of the quantum ring is that the magnetic field effect in a quantum ring can give a novel result for future nano-devices which are based on the magnetic field. The nature of the electronic state is strongly

affected by the magnetic flux and its properties are changed when the magnetic flux is penetrating into it. The energy distributions of electrons in bulk, quantum-well, quantum-wire and quantum-dot structures under a low carrier-density limit condition, where electrons obey the *Boltzmann's distribution statistics*, are illustrated in Fig. 2.3.

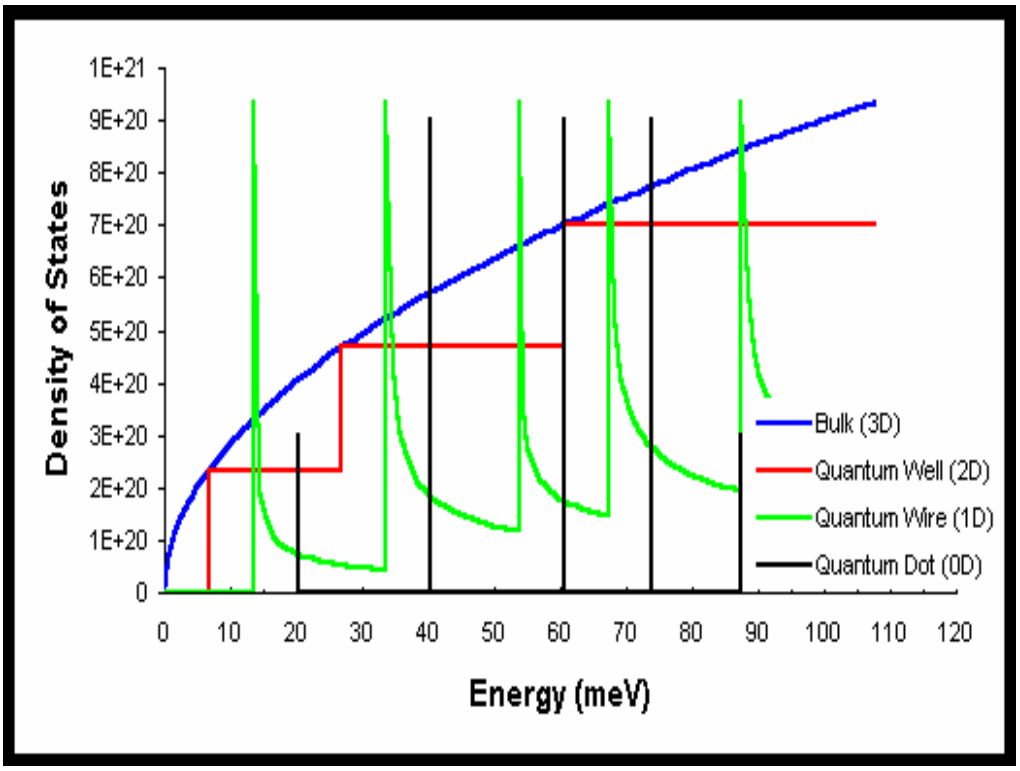

Figure 2.3 Nature of electron density of states in bulk, quantum well, quantum wire, and quantum dot.

2.2 Effect of Quantum Confinement on Optics of Semiconductor Nanostructures

Quantum confinement produces a number of important effects in the electronic and optical properties of semiconductor nanostructures. This effect is very useful for future electronic and optoelectronic device applications. Since this project is focused on optical characterizations of low-dimensional quantum dot structures, only the quantum confinement effect which is important in relation with the optical properties [37-38] will be discussed in this section. The optical processes of nanostructures are summarized in the tree diagram below.

Tree diagram: Optics of quantum-confined semiconductors

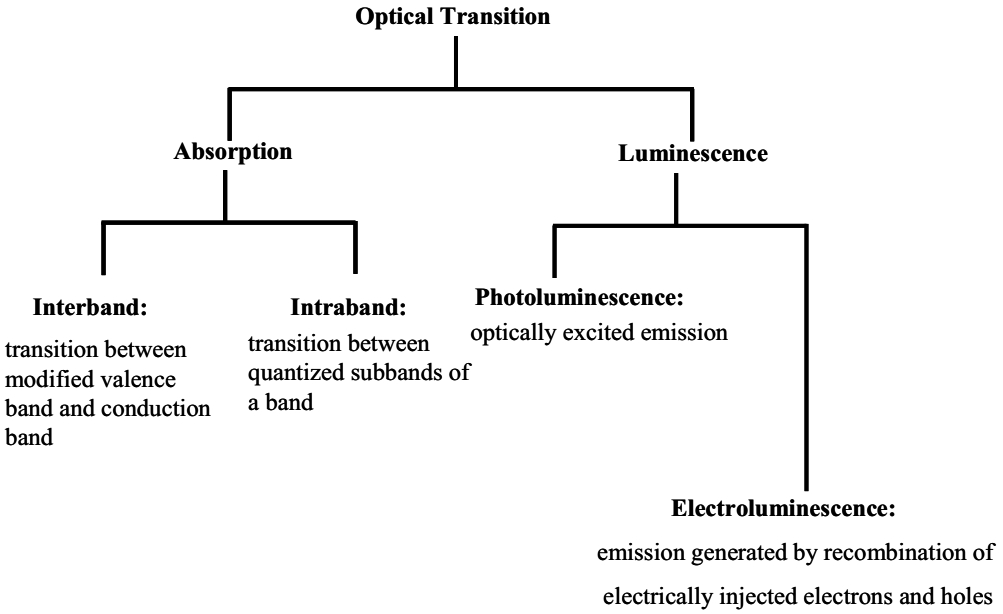

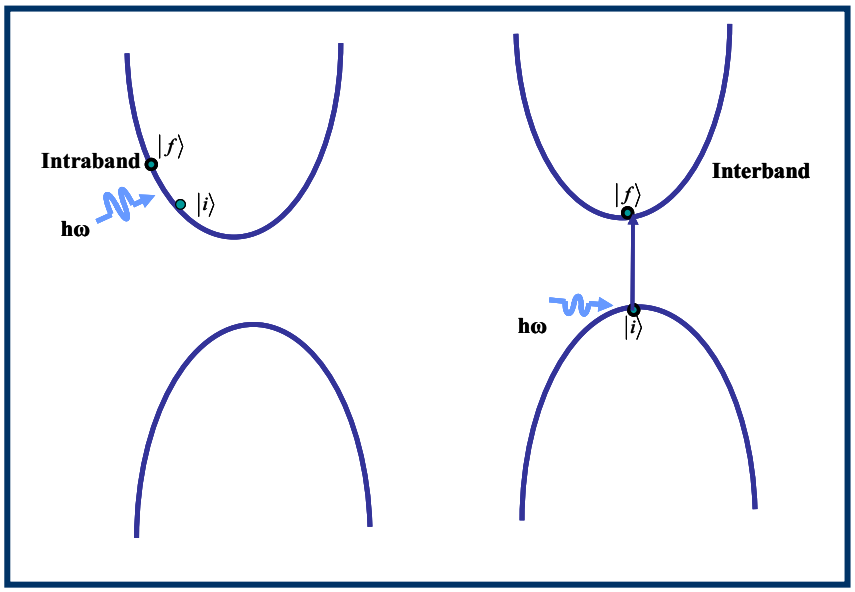

Figure 2.4 Intraband and interband scattering of an electron from an initial state to a finial state.

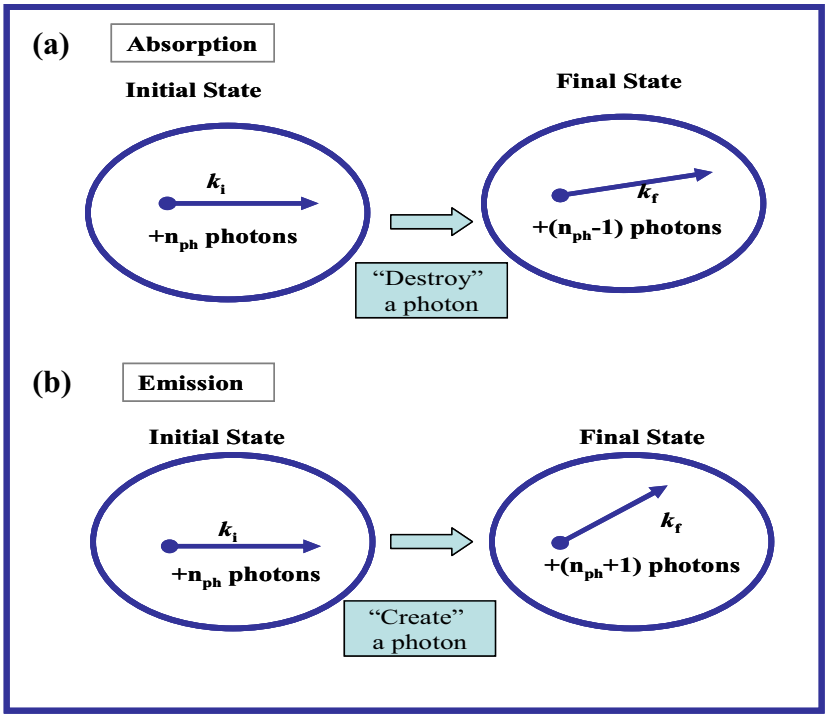

Figure 2.5 (a) Schematic diagram of an absorption process where a photon is absorbed (destroyed) and the energy and the momentum of the electron is altered (upper figure),
(b) The emission of a photon where a photon is created (lower figure).

2.2.1 Size Effect on Optical Properties

Many experimental studies proved that nanostructures of dimensions 1 to 10 nm exhibits fairly narrow optical transitions that are size-dependent. Since the quantum confinement affects the bandgap of the nanostructure, higher quantum confinement gives increasing bandgap as well as appearance of discrete subbands corresponding to quantization along the direction of confinement. Therefore, the structure of a certain size shows optical transition (absorption and emission) at a given frequency. When the size of the structure is increased, the bandgap decreases, and thus the optical resonance shifts to the lower frequency (longer wavelength), and finally approaching the bulk value for a large-enough size.

2.2.2 Increase of Oscillator Strength

As explained in Section 2.1, quantum confinement produces a major modification in the density of states, both for the valence band and the conduction bands. Instead of continuous, smooth distribution of the density of states, the energy is squeezed in a narrow energy range. This packing of energy states near the bandgap becomes more pronounced as the dimensions of confinement increase from bulk, to quantum well, quantum wire, and then quantum dot. For the quantum dots, the density of states has non-zero values only at discrete (quantized) energies. The oscillator strength of an optical transition for an interband transition depends on the joint density of states of energy levels in the conduction band and the valence band, between which the optical transition occurs. Furthermore, it also depends on the overlap of the envelope wavefunctions of electrons and holes. Both these factors produce a large enhancement of oscillator strength upon a quantum confinement. This effect is quite pronounced in quantum wires and quantum dots which are more confined structures (two-dimensionally and three-dimensionally, respectively).

2.2.3 New Intraband Transition

In bulk, the valence band consists of the light-hole band (LH), the heavy-hole band (HB) and the split-off band. The three subbands are separated by the spin-orbit interaction. The absorption of photons with the right energy can result in transition from LH-to-HH, SO-to-HH, or SO-to-LH band, depending on the doping and temperature of the sample or as the result of charge injection introduced by a bias field (e.g. photoinjection). In bulk, transition from one level to another level within the conduction band or the valence band requires a change of quasi-momentum and thus becomes allowed only by the coupling with lattice phonons, which can provide a momentum change. The probability for an intraband transition in bulk semiconductor to occur is low compared with an interband transition in which there is no requirement to change k value.

In quantum-confined nanostructures, there are subbands characterized by the different quantum numbers (n = 1, 2, 3, …) corresponding to quantization along the direction of confinement (growth). Thus, for the conduction band, the electron can jump from one sublevel to another without changing its quasi-momentum k. These

new transitions are in IR and have been utilized to produce inter-subband detectors and lasers. These intraband transitions still require the presence of a carrier in the conduction band (electron) or in the valence band (hole). The absorption coefficient for an intraband transition increases rapidly when the size of the nanostructure is decreased. However, for quantum wells, for example, the electronic states are no longer confined within the well, which therefore produces a leveling-off of the absorption coefficient.

2.2.4 Increased Exciton Binding Energy

Quantum confinement of electrons and holes also leads to enhanced binding energy between them and produces increased exciton binding energy compared with the exciton binding energy for bulk materials. For example, a simple theoretical model predicts that the Coulomb interaction between free electrons and holes in a two-dimensional system, or the quantum well, is four times higher than that in bulk. However, actual binding energy is somewhat smaller than in the bulk because the wavefunction of the carriers penetrates into the barrier nearby. This binding produces the excitonic state just below the bandgap, giving rise to the sharp excitonic peaks at temperatures where the exciton binding energy is higher than the thermal energy. Thus, excitonic resonances are very pronounced in quantum-confined structures and, in the strong confinement condition, can be seen even at room temperature.

2.2.5 Dielectric Confinement Effect

Quantum-confined structures also exhibit the dielectric confinement effect produced by the difference in the dielectric constant of the confined semiconductor region and the confining potential around it. However, quantum wells, quantum wires and quantum dots, depending on the method of fabricating and processing, may be embedded in the different semiconductor or a dielectric such as glass or polymer. These quantum structures may be encapsulated by organic ligands, dispersed in a solvent or simply surrounded by air. If the dielectric constant of the surrounding medium is significantly lower than that of the confined semiconductor region, there will be important manifestations derived from different dielectric confinements.

2.2.6 Increase of Transition Probability in Indirect-Bandgap Semiconductors

In the case of an indirect-bandgap semiconductor, the bottom of the conduction band and the top of the valence band do not have the same wave vector k. Thus, emission is not probable in the bulk form, for example, in bulk silicon. However, in a quantum-confined structure, confinement of the electrons produces a reduced uncertainty Δx and increased uncertainty Δk in its quasi-momentum. Confinement, therefore, relaxes the quasi-momentum Δk selection rule, and thus allowing the enhanced emission to be observed in porous silicon and silicon nano-particles.

2.2.7 Nonlinear Optical Properties Caused by the Quantum Confinement Effect

Quantum-confined materials also exhibit enhanced nonlinear optical effects, compared to the corresponding bulk materials. A primary effect is the intensity-dependent changes in optical absorption, derived from a number of processes such as phase-space filling and bandgap renormalization. These processes are manifested at high excitation intensities.

A new optical transition is manifested on binding of excitons to produce bi-excitons. Pronounced changes in optical spectra are observed by applying an electric field along the confinement direction. This is called the *quantum-confined Stark effect* and can be utilized in electro-optic modulator.

2.3 Quantum Dots and Physics Behind Them

Three-dimensional quantum-confined structures, that is, quantum dots (QDs), are solid-state systems that may consist of many atoms. Nevertheless, many experiments have shown in many ways that they behave like a simple quantum system. Here, only conduction-band electrons and valence-band holes are considered, and imagine that everything else can be incorporated into the effective potential acting on these particles, their effective masses, and the dielectric constant of the crystal. The goal here is to describe aspects of the behaviour of idealized quantum dots that are relevant to this project.

2.3.1 Energy Levels

Many theoretical calculations have been attempted to explain the energy levels of quantum dots. Among these, the most complicated numerical model is the model that includes realistic shapes and the effects of strain [42-44]. The parameters of the assumed structures strongly affect the result of the energy levels of the quantum dots. But, to gain a qualitative understanding, energy levels are often calculated by using the effective-mass approximation [45], which assumes a single electron in the conduction band of a periodic semiconductor and ignoring its spin. For a plane wave with momentum *k*, its wavefunction can be written as

$$\psi_e(r) = e^{ik.r} u_{e,k}(r) \tag{2.9}$$

where $u_{e,k}(r)$ is periodic: $u_{e,k}(r+R) = u_{e,k}(r)$, where *R* is any lattice vector. In the effective-mass approximation, the wavefunction of an electron that experiences a slowly varying potential in a direct-bandgap semiconductor is approximated as

$$\psi_e(r) = f(r) u_{e,0}(r) \tag{2.9-a}$$

where *f*(*r*) is the envelope function, which satisfies the Schrödinger equation:

$$\left[-\frac{\hbar^2}{2m^*} \nabla^2 + V(r) \right] f(r) = Ef(r) \tag{2.10}$$

where *m** is the effective mass, related to the curvature of the conduction band at $k = 0$, $V(r)$ is effective potential coming from different band offsets of different materials, and *E* is the energy of the state. In buried QDs (quantum-confined tiny region which is surrounded by another semiconductor material), the confining barrier *V* is of finite height as defined by the band offset of two different materials.

Let us assume that self assembled quantum dots are highly flattened in the growth direction (in *z* direction) comparing with lateral dimensions (*x* and *y* direction). It has been reported that the energy level spacing in the *z* direction can be fairly constant [46]. Thus commonly chosen potential for this kind of structure is

$$V(r) = \begin{cases} \frac{1}{2} m^* \omega_0^2 (x^2 + y^2) & \text{for } |z| < \frac{L}{2} \end{cases} \quad \text{(2.10-a)}$$

$$V(r) = +\infty \text{ for } |z| > \frac{L}{2} \quad \text{(2.10-b)}$$

where L defines the height of the quantum dots. The energy levels resulting from this Hamiltonian are [47]

$$E = (n_x + n_y + 1)\hbar\omega_0 + (\frac{\pi^2\hbar^2}{2m^* L^2})n_z^2 \quad \text{(2.10-c)}$$

where n_x and n_y are integers ≥ 0, and n_z is an integer ≥ 1. Usually, L is assumed to be small, so that only the n_z = 1 states are considered. For InAs quantum dots, the spacing $\hbar\omega_0$ between the lowest two electron energy levels is typically in the range of 30-80 meV. The relevant wavefunctions that satisfy Eq. 2.10 are:

$$f(R) = H_{n_x}(x) H_{n_y}(y) e^{-\frac{1}{2}\frac{m^*\omega_0}{\hbar}(x^2+y^2)} \cos(\frac{\pi z}{l}) \quad \text{(2.10-d)}$$

where H_n are the Hermite polynomials [47]. A schematic diagram of the energy levels is shown in Fig. 2.6.

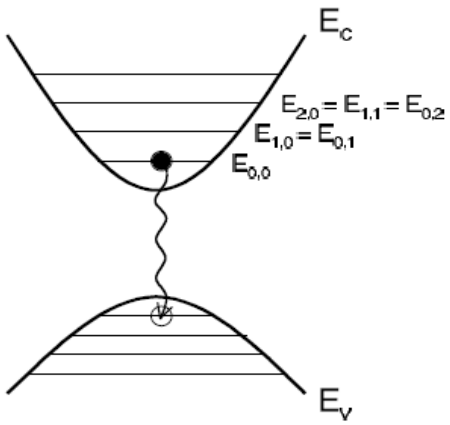

Figure 2.6 Energy band diagram of quantum dot: A radiative transition from the lowest energy level in the conduction band to the highest energy level in the valence band is indicated.

For electrons in the conduction band, the atomic orbital functions contained in $u_{e,0}(r)$ have *s*-like symmetry, and there is a spin degeneracy in the conduction band. There is complicated situation for the holes in the valence band, because the corresponding atomic orbital functions have *p*-like symmetry in the valence band. There are three bands (heavy-hole, light-hole, split-off) which can "mix" in the conduction band [45].

When studying quantum dots, only the heavy holes in the valence band have been taken into account in calculation, for simplicity. It is assumed that the highest valence-band state (the hole "ground state") has a heavy-hole nature when the quantization axis is taken to be *z*, the axis of symmetry. It is often further assumed that the splitting between the first heavy-hole state and the first light-hole state is large, so that the light-hole states can be neglected in the perturbation-theory calculations. The periodic component of the heavy-hole states can be written as $\left|m_j = 3/2\right\rangle = \left|m = 1, \uparrow\right\rangle, \left|m_j = -3/2\right\rangle = \left|m = 1, \downarrow\right\rangle$, where m and m_j are the z projections of the orbital angular momentum and the total angular momentum, respectively.

2.3.2 Spontaneous Emission

The spontaneous emission of electron-hole pairs inside quantum dots is described in this section. Scull *et al* [48] explained the quantum-optic portion of the quantum dot by the following equation, which uses the Hamiltonian describing a quantum dot interacting with modes of the electromagnetic field in the dipole approximation.

$$H = \sum_i E_i \left|i\right\rangle\left\langle i\right| + \sum_{k,\varepsilon} \hbar\omega_k a^{\dagger}_{k,\varepsilon} a_{k,\varepsilon} + \hbar \sum_{k,\varepsilon} \sum_{i,j} g_{ij,k\varepsilon} [a^{\dagger}_{k,\varepsilon} + a_{k,\varepsilon}] \left|j\right\rangle\left\langle i\right| \qquad (2.11)$$

where $\left|i\right\rangle, \left|j\right\rangle$ are quantum-dot levels with energies $E_{i,}$ E_j and $a_{k,\varepsilon}$ are the photon annihilation operators for wavevector k and polarization ε. The coupling coefficient $g_{ij,k\varepsilon}$ between the atom and field modes are given by the equation [48]

$$g_{ij,k\varepsilon} = \left(\frac{\omega_k}{2\varepsilon_0 \hbar V}\right)^{\frac{1}{2}} \varepsilon . \mu_{ij} \qquad (2.12)$$

where $\mu_{ij} = e\langle i|r|j\rangle$ is the atomic transition dipole moments, and V is the volume of the box chosen in quantizing the electromagnetic field. The spontaneous emission from the lowest-energy electron-hole state will be discussed in this section. When electron-hole pairs are injected into a quantum dot slowly (weak excitation), electrons and holes from the higher excited state rapidly relax to the lowest state via intraband transition with the help of phonon emission, after which, the conduction-band electrons return back to the valence band by the radiative recombination. The transition is primarily radiative and the luminescence due to such transition may be seen. The lifetime of the transition is normally in the order of 1 ns. Emission from higher excited states becomes prominent while the strong excitation is used. In such a case, the carriers are injected into the quantum dots quickly and the ground-state recombination is too fast to keep pace with the carrier injection, and thus, the quantum dots begin to be filled with carriers.

The lowest-energy state which consists of one electron-hole pair is supposed to be called "one-exciton" state and there are four terms in this one-exciton state, represented by $\{|\sigma, m_j|\}$ in which σ is the electron spin which value is $\sigma = \pm\frac{1}{2}$ and m_j is the total angular momentum (assuming heavy holes) which value is $m_j = \pm\frac{1}{2}$, both projected along the z axis Firstly, a *very small* quantum dot is considered to calculate the dipole moment for the transition, in which a non-interacting-particle approximation is used [48].

$$\mu_{ab} = e\delta_{\sigma,-\frac{m_j}{3}} \int \psi_e^*(r)\, r\, \psi_h(r) d^3r \tag{2.13}$$

where, ψ_e (r) and, ψ_h (r) are the total wavefunction of electron and hole. The δ function appears because the spin of the electron is conserved in a dipole transition. Next the valence band counterpart is inserted into above equation and the equation expands over lattice sites.

$$\mu_{ab} = \delta_{\sigma,-\frac{m_j}{3}} \int d^3r f^*(r) g(r) \frac{1}{\Omega} \int_{\Omega} u_{e,0}^*(r') er u_{h,m,0}(r') d^3r' \tag{2.14}$$

$$\mu_{ab} = \delta_{\sigma,-\frac{m_j}{3}} \int f^*(r) g(r) \mu_{cv} \frac{x + imy}{\sqrt{2}} d^3r' \tag{2.15}$$

where Ω is the volume of one unit cell, $m = \pm 1$ is the atomic orbital angular momentum of the hole (the same sign as m_j), and $f(r)$ and $g(r)$ are the electron and hole envelope function in the effective-mass approximation, respectively. In the second equation, the integral is replaced by a μ_{cv}, which is a standard material parameter, multiplied by a unit vector corresponding to the orbital angular momentum of the hole. The first term in the above equation is the spin conservation term. It indicates the existence of the bright and dark excitons. For dark excitons, the spins do not match and an open transition cannot occur until the spin of either electron or hole gets flipped. For bright excitons, the spin of the electron match with the spin of the hole. The last term gives the vector dimension of the dipole moment, leading to the polarization selection rule. The angular momentum of the atomic orbital wavefunction of the hole is transferred to the total angular of the emitted photon. The transition strength depends on the overlap between the electron and hole wavefunction. The Hamiltonian in the above equation can be satisfied by using the following equation.

$$H = \hbar\omega_{ab}|a\rangle\langle a| + \sum_{k,\varepsilon}\hbar\omega_k a^{\dagger}_{k,\varepsilon}a_{k,\varepsilon} + \hbar\sum_{k,\varepsilon}(g^{*}_{k,\varepsilon}|a\rangle\langle b|a_{k,\varepsilon} + g_{k,\varepsilon}a^{\dagger}_{k,\varepsilon}|b\rangle\langle a|) \quad (2.16)$$

where $\hbar\omega_{ab}$ is the energy difference between the state $|a\rangle$ and $|b\rangle$, and $g_{k,\varepsilon} = g_{ba,k\varepsilon}$. In the initial state at time $t = 0$, the system consisting a bright exciton and zero photons is $|a\rangle|0\rangle$, where $|0\rangle$ denotes the vacuum state of the electromagnetic field. At finite time, this state evolves into,

$$|\psi(t)\rangle = c_a(t)e^{-i\omega_{ab}t}|a\rangle|0\rangle + \sum_{k,\varepsilon}c_{b,k,\varepsilon}(t)e^{-i\omega_k t}|b\rangle a^{\dagger}_{k,\varepsilon}|0\rangle \quad (2.17)$$

in which ω_k is the frequency of mode k**,** Schrödinger's equation with the Hamiltonian in Eq. 2.16 provides differential equations relating the complex functions $c_a(t)$ and $c_{b,k,\varepsilon}(t)$ which determine the time evolution of the state. These equations can be solved in the Weisskopf-Wigner approximation, which assumes that ω_k varies only little over the linewidth of the transition, which is true in our case ($\frac{\delta\omega}{\omega_{ab}} \approx 10^{-6}$). The result of this calculation is:

$$c_a(t>0) = e^{-(\Gamma/2)t} \tag{2.18}$$

and

$$c_{b,k,\varepsilon}(t>0) = g_{k,\varepsilon}\frac{1-e^{-i(\omega_{ab}-\omega_k)t-\Gamma t/2}}{i(\omega_{ab}-\omega_k)t+\Gamma t/2} \tag{2.19}$$

$$\Gamma = \frac{n\omega_{ab}^3\left|\mu_{ab}\right|^2}{3\pi\varepsilon_0\hbar c^3} \tag{2.20}$$

The final state of the emitted photon is

$$\left|\gamma\right\rangle = \sum_{k,\varepsilon} g_{k,\varepsilon}\frac{e^{-i\omega_k t}}{(\omega_k-\omega_{ab})+i\frac{\Gamma}{2}}a_{k,\varepsilon}^{\dagger}\left|0\right\rangle \tag{2.21}$$

The spatial form of the photon wave packet is obtained by taking the Fourier transform of the above result, using $a_{k,\varepsilon}^{\dagger} \propto \sum_r \exp(ik.r)a_{r,\varepsilon}^{\dagger}$. In the far field $(|k||r| >> 1)$, the result for the dipole with angular momentum projection *m* is

$$\left|\gamma\right\rangle = \sum_r \frac{\phi(ct-r)}{|r|}e^{(i\omega_{ab}-\frac{\Gamma}{2})(t-|r|/c)}\left(\hat{r}\times X_{lm}\right).a_r^{\dagger}\left|0\right\rangle \tag{2.22}$$

where φ is the unit step function and X_{lm} are the vector spherical harmonics. The angular dependence of this function is the same as for the electric field from a classical radiating dipole. The time dependence is a one-sided decaying exponential. The photon is in a pure quantum state.

The spontaneous emission rate Γ depends on the dipole moment μ_{ab}, which depends on the material parameter μ_{cv} and on the overlap between the electron and

hole envelope functions. The parameter $\frac{\mu_{cv}}{e}$ is approximately 1 nm, and can be estimated using $\frac{u_{cv}}{e} = \sqrt{\hbar^2 E_p / 2m_0 E_g^{\ 2}}$, where E_g is the bandgap and $E_p \approx 24$ eV is a parameter in the Kane model. Therefore when $1/\Gamma > 0.28$ ns, the spontaneous emission rates typically 0.5 ns or longer was observed.

For a larger quantum dot, the electron and the hole become correlated, due to the electrostatic interaction between them. The two particle envelope function $h(r,s)$ is needed to be use in calculation. In this situation, the overlap integral is replaced by $\int d^3 r h(r,r)$. For large quantum dots, where the natural exciton Bohr radius a_B^* is smaller than the quantum-dot radius a, the electron-hole overlap term can become larger than one, scaling as (a/a_B^*) 3/2. The spontaneous emission rate is thus enhanced for larger quantum dots.

Eventually, when the dot size becomes comparable to the wavelength of light in the crystal, the lifetime does not decrease further, but rather the emission becomes directional. The center-of-mass angular momentum of the exciton is transferred into the momentum of the emitted photon, as in quantum-well structures.

2.3.2 Polarization Property

By utilizing the electron and the hole wavefunctions obtained as outlined above, the polarization property for each transition can be theoretically calculated. The polarization property is determined with the localization of the wavefunctions of carriers. In bulk, the electrons and holes can move around in every direction without any restriction; the wavefunctions for them distribute uniformly, and thus the dipole moment which is determined by the overlap integral of the wavefunctions of electrons and holes has no directional dependence. Thus, the emission PL spectrum has no polarization property. When the movement of electrons and holes is restricted with the introduction of the quantum-confined structures, the wavefunctions tend to localize. Especially, the quantum-dot structure produces the complete localization of wavefunctions, which leads to the polarization of the luminescence for each transition [49].

CHAPTER III
NUMERICAL CALCULATION

3.1 Mathematical Approach

In this section, the theoretical calculation procedures as well as the mathematics behind the calculation are discussed. The mathematical model for the calculation was based on the AFM images of the LAQD system and on the results obtained from the PL measurements. It was observed that the quantum dots aligned in the $[1\bar{1}0]$ direction and that the size in the [001] direction (the growth direction) of each QD was 4 nm and the sizes in the [110] and $[1\bar{1}0]$ directions were both about 40 nm to 60 nm for aligned quantum dots, and about 20 nm for binary quantum dots. Generally, strong PL signal comes from the recombination between electrons and holes in the ground state, thus the main focus of the calculation was on the ground-state eigen-energy levels.

3.2 Mathematical Model

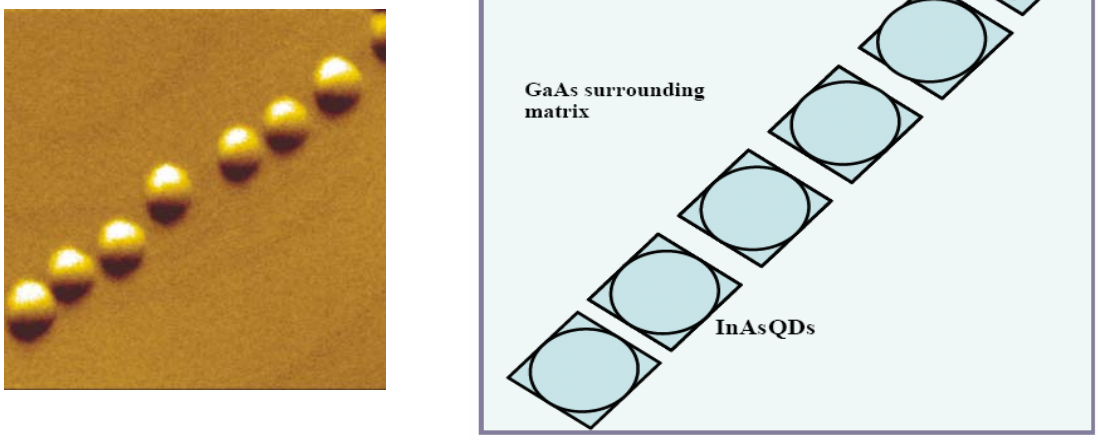

(a) **(b)**

Figure 3.1 (a) An AFM image of InAs/GaAs linearly aligned quantum dots, and (b) the corresponding schematic diagram.

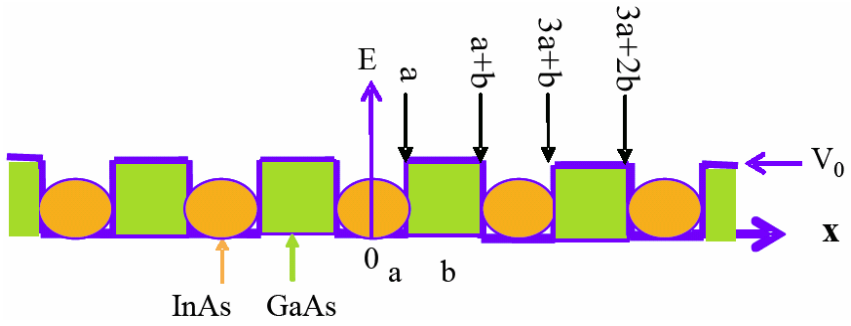

Figure 3.2 Schematic diagram of the model for linearly aligned quantum dots.

According to the AFM image, the top view of the QDs has a circular shape. The InAs QDs were embedded in the GaAs surrounding matrix (i.e., GaAs capping layer and substrate). In the calculation it was assumed for simplicity that all the QDs had the same size with the same spacing between them, so that the quantum-mechanical model of the LAQD system is similar to that of the periodic multiple quantum wells, as shown in Fig. 3.2, in which the quantum well regions correspond to the InAs quantum dots and the potential barriers correspond to the GaAs capping-layer material.

3.3 Theory

Since the quantum dots aligned along a straight line and the PL from them showed a certain degree of linear polarization, the relevant Schrödinger equation is one-dimensional, with three describing parameters, namely, the well width of size $2a$, the barrier width b, and the barrier height V_0. In as much as the PL is due mainly to the recombination of carriers in the ground state, the calculation was focused on the ground-state eigen-energies (E_0) only. The eigen-energy and the eigen-function (wavefunction) of a single carrier in semiconductor linearly aligned quantum dots can be calculated from the time-independent Schrödinger equation:

$$H\psi(x) = [-\frac{\hbar^2}{2m^*}\frac{\partial^2}{\partial x^2} + V(x)]\psi(x) = E\psi(x) \qquad (3.1)$$

In the above Eq. (3.1), m^* is the effective mass of the electron and $\hbar$ is the Planck's constant. $V(x)$ is the difference between the bandgap energy of InAs quantum

dots and the GaAs surrounding matrix, which are 1.12 eV and 1.43 eV (at room temperature), respectively. That is,

$$V(x) = \begin{cases} 0 & \begin{cases} x \in QDs \\ x \notin QDs \end{cases} \\ V_0 \end{cases}$$

$\psi(x)$ is the wavefunction that satisfies the appropriate boundary conditions. E is the eigen-energy of the system. Since recombination occurs for the carriers in the *bound states*, only the case for which $E < V_0$ was considered.

3.4 Numerical Method

The Schrödinger equation was solved using the finite difference method (FDM) written in the Matlab® programming language. The FDM was implemented using uniform grids for the one- and two-dimensional Schrödinger equations in rectangular coordinates.

3.4.1 One-Dimensional Schrödinger Equation

To solve the Eq. 3.1 numerically by using FDM, the wavefunction must be discretized first [50]. The wavefunction and the potential were discretized into many small grid points such that the x coordinates becomes $x_i = ih_0$, where the index i = 0, 1, 3 4, …, N (arbitrary integer), and h_0 is the separation between the adjacent grid points. This is illustrated in Fig. 3.3.

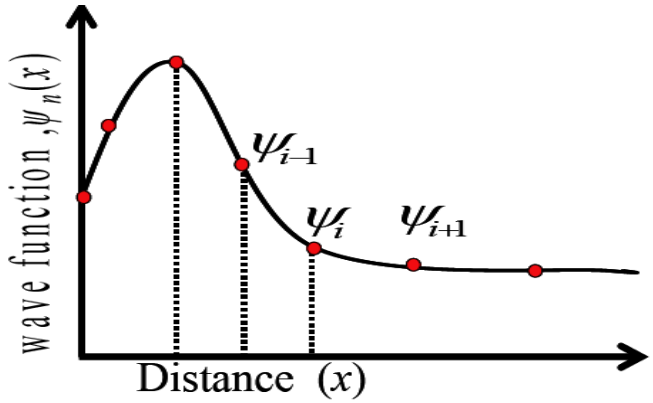

Figure 3.3 Three-point finite-difference approximation used to discretize the wavefunction and the potential energy.

By using a three-point finite-difference approximation, the second derivative of the discretized wavefunction became

$$\frac{d^2}{dx^2}\psi(x_i)=\frac{\psi(x_{i+1})-2\psi(x_i)+\psi(x_{i-1})}{h_0^2} \tag{3.2}$$

After substituting Eq. 3.2 into 3.1, the following matrix equation was obtained:

$$H\psi(x)=[-u_i\psi(x_{i+1})+d_i\psi(x_i)-u_i\psi(x_{i-1})]=E\psi(x_i) \tag{3.3}$$

In Eq. 3.3, the Hamiltonian is a symmetric tri-diagonal matrix. The diagonal matrix elements are

$$d_i=\frac{\hbar^2}{mh_0^2}+V(i) \tag{3.4}$$

and the adjacent off-diagonal matrix elements are

$$d_i=\frac{\hbar^2}{2mh_0^2} \tag{3.5}$$

Changing Eq. 3.3 into a matrix form yields the following equation

$$(H-EI)\psi=\begin{bmatrix} (d_1-E) & -u_2 & . & . & . & . & & \\ -u_2 & (d_2-E) & -u_3 & . & & & & \\ . & -u_3 & (d_3-E) & -u_4 & . & & & \\ . & . & -u_4 & (d_4-E) & . & . & & \\ . & . & & & . & . & & \\ . & . & & & . & . & . & \\ . & & & & & . & . & \\ & & & & & & -u_{N-1} & (d_1-E) \end{bmatrix}\begin{bmatrix} \psi_1 \\ \psi_2 \\ \psi_3 \\ \psi_4 \\ \\ \\ \\ \psi_{N-1} \end{bmatrix}=0 \tag{3.6}$$

where H is the Hamiltonian matrix and I is the identity matrix. By using Matlab® programming language the eigen-energies and eigen-functions of the one-dimensional quantum well problem were obtained.

For the present purpose, the semiconductor heterostructure model was used, and so the different effective masses were taken into account. Ben-Daniel and Duke's effective mass Hamiltonian was used in the Schrödinger equation:

$$H = -\frac{\hbar^2}{2}\frac{\partial}{\partial x}\left(\frac{1}{m^*(x)}\frac{\partial}{\partial x}\right) + V(x) \tag{3.7}$$

Discretization of the Schrödinger equation using Ben-Daniel and Duke's effective Hamiltonian [51-53] gives

$$\frac{-\hbar^2}{x^2}\left(\frac{\psi_{j+1}}{m^*_{i+1}+m^*_i} - \frac{\psi_j}{m^*_{i+1}+m^*_i} - \frac{\psi_j}{m^*_{i-1}+m^*_i} + \frac{\psi_{j-1}}{m^*_{i-1}+m^*_i}\right) + V_j\psi_i = E\psi_i \tag{3.8}$$

Eq. (3.8) can be constructed in a matrix form similar to the previous equation.

3.4.2 Two-Dimensional Rectangular Dots

For the two-dimensional case, the Hamiltonian of the Schrödinger equation has two variables.

.

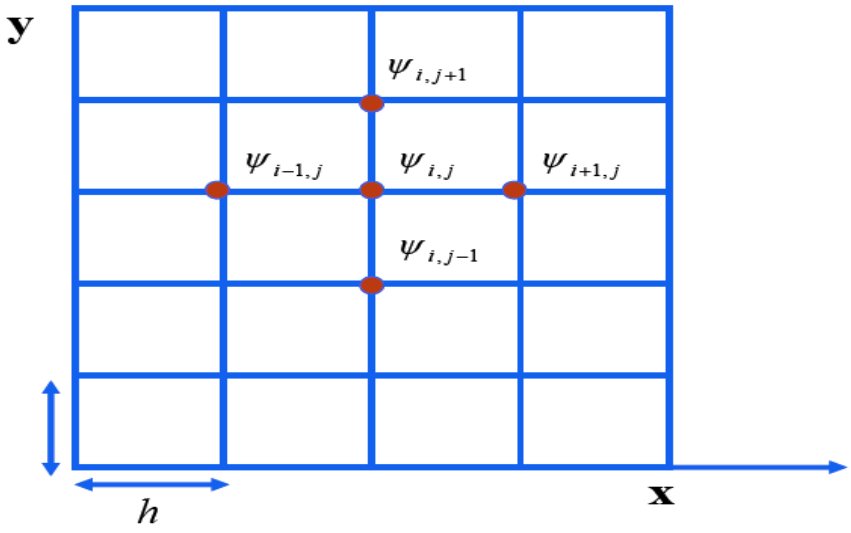

Figure 3.4 The discretized mesh points for the two-dimensional Schrödinger equation.

The two-dimensional Schrödinger equation was changed into the two-dimensional finite-difference form:

$$-\frac{\hbar^2}{2m^* h_0^2}\left[\{\psi_{i-1,j}-2\psi_{i,j}+\psi_{i+1,j}\}-2\psi_{i,j}+\{\psi_{i,j-1}-2\psi_{i,j}+\psi_{i,j+1}\}\right]+V_{ij}\psi_{i,j}=E\psi_{i,j} \tag{3.9}$$

Using different effective masses in the above equation leads to:

$$\frac{-\hbar^2}{h_0^2}\left(\frac{\psi_{i,j-1}}{m^*_{i,j-1}+m^*_{i,j}}+\frac{\psi_{i,j+1}}{m^*_{i,j+1}+m^*_{i,j}}+\frac{\psi_{i-1,j}}{m^*_{i-1,j}+m^*_{i,j}}+\frac{\psi_{i+1,j}}{m^*_{i+1,j}+m^*_{i,j}}-\right.$$
$$\left.\frac{\psi_{ij}}{m^*_{i,j+1}+m^*_{i,j}}-\frac{\psi_{ij}}{m^*_{i+1,j}+m^*_{i,j}}-\frac{\psi_{ij}}{m^*_{i-1,j}+m^*_{i,j}}-\frac{\psi_{ij}}{m^*_{i,j+1}+m^*_{i,j}}\right)+V_j\psi_i=E\psi_{ij} \tag{3.10}$$

The above differential equation can be changed into the following matrix form:

$$\begin{bmatrix}
(d_{11}-E) & -u & & u & & & & & \\
-u & (d_{12}-E) & -u & & u & & & & \\
 & -u & (d_{13}-E) & & & u & & & \\
u & & & (d_{21}-E) & -u & & u & & \\
 & u & & -u & (d_{22}-E) & -u & & u & \\
 & & u & & -u & (d_{23}-E) & -u & & u \\
 & & & u & & -u & (d_{31}-E) & & \\
 & & & & u & & & (d_{32}-E) & -u \\
 & & & & & u & & -u & (d_{33}-E)
\end{bmatrix}
\begin{bmatrix}\psi_{11}\\ \psi_{21}\\ \psi_{31}\\ \psi_{12}\\ \psi_{22}\\ \psi_{32}\\ \psi_{13}\\ \psi_{23}\\ \psi_{33}\end{bmatrix}=0 \tag{3.11}$$

Checking the Numerical Method

To check the accuracy of the numerical method thus developed, an analytical method was used for comparison. For simplicity, the binary QD system was considered. The wavefunctions and the derivative of the wavefunctions of the QDs were continuous at the boundaries. After manipulating the Hamiltonian equation, a transcendental equation was obtained. By using the graphical method or an aide by the computer program, the eigen-energies and eigen-functions of the system can be

obtained. By comparing these results with the numerical data, the accuracy of the numerical method could be then adjusted.

Table 3.1: Comparison between the analytical and the numerical methods.

Eigen-energy level	Analytical method	FDM 200 node points/nm	FDM 100 node points/nm	FDM 50 node points/nm
E_1	1.13573399	1.135722787087	1.135689165755	1.135554701534
E_2	1.159285852	1.159274775287	1.159241544238	1.159108640738
E_3	3.970491881	3.970465351407	3.970384186515	3.970059481673
E_4	4.203528034	4.203498010204	4.203398998420	4.203002901767

The results above are the four lowest eigen-energies of a bi-QD system with the well width 2 nm, the barrier width 2 nm, and the barrier high 5 eV. A 4000 × 4000 matrix was the largest matrix used in the calculations. From the above table, it can be clearly seen that the higher number of node points, the better the accuracy is.

3.5 Results and Discussion

3.5.1 Energy-Splitting Behavior

A computer program was written in Matlab® to numerically solve the equation that was written by Finite-Difference Method (FDM) with appropriate boundary conditions. Fig. 3.5 (a), (b) and (c) show the ground-state energy E_0 as a function of the barrier width b, for fixed values of the well width $2a$ = 20 nm and the barrier height V_0 = 0.31 eV, corresponding to the chain of four, five, and six quantum dots, respectively. As shown in Fig. 3.5, for fixed values of the well width and barrier height, the ground-state energy levels begin to split when the potential wells are close enough to each other so that coupling between them manifests, and the energy levels become degenerate when the wells are far enough from each other so that the coupled dots become similar to the single, individual dots. Note that in any case the splitting is maximum when the barrier width is zero (no barrier), in other words, all the quantum wells coalesce and become a single longer potential well having an integral

size of $n(2a)$, where n is the number of the constitutive wells. When this happens the top-most and the bottom-most of the splitting energy levels are identical to the first excited-state and ground-state energy levels of a single, isolated potential well of size $n(2a)$, respectively. Higher energy levels obtained from these calculations also show a similar trend.

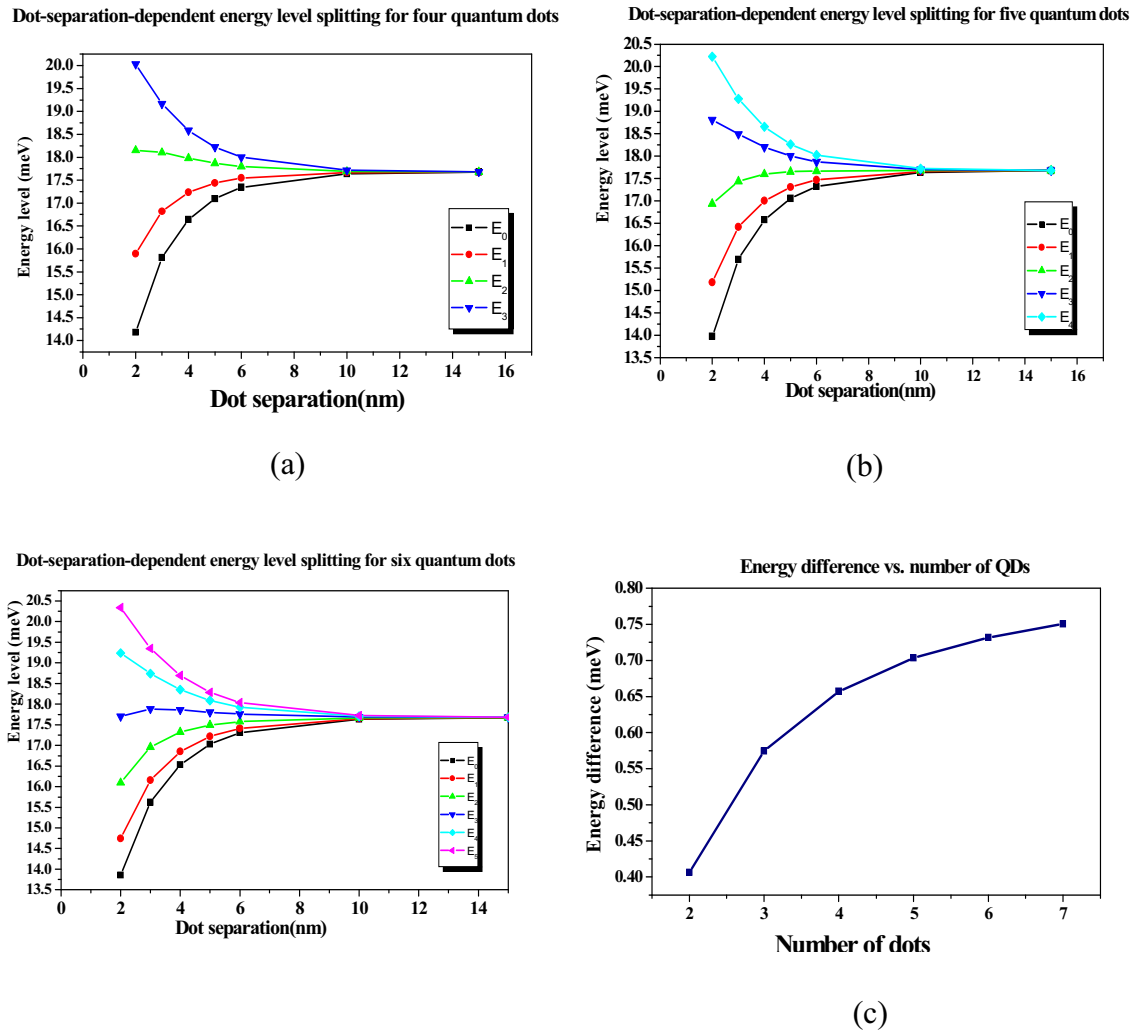

Figure 3.5 Dot-separation-dependent energy splitting behavior for (a) four, (b) five, and (c) six QDs; and (d) difference in energy of the top-most and the bottom-most ground-state levels versus the number of QDs.

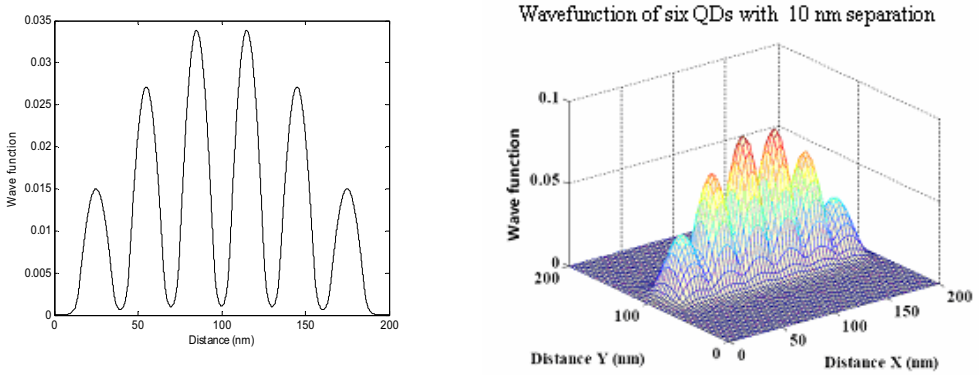

(a)

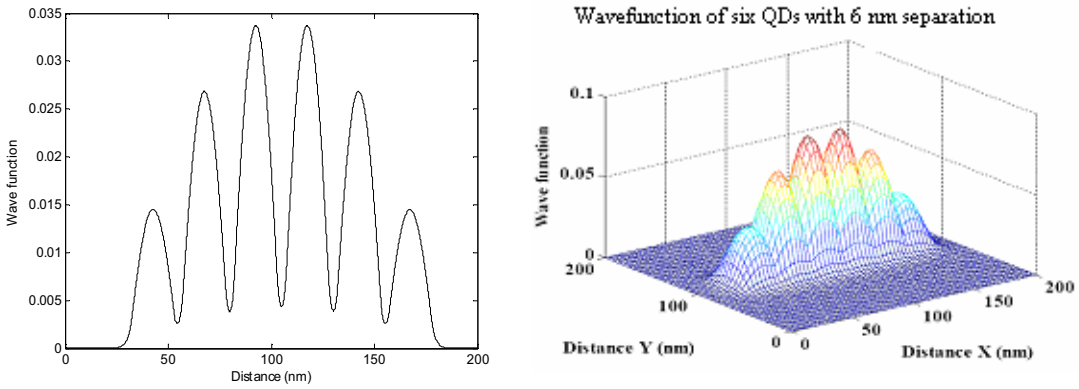

(b)

Figure 3.6 One-dimensional (left) and two-dimensional (right) coupling behavior of six coupled QDs with dot separation (a) 10 nm, and (b) 6 nm.

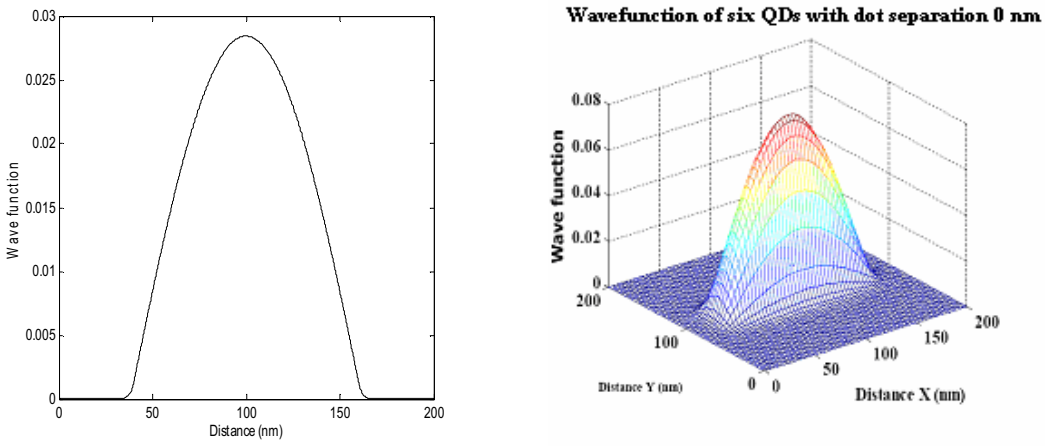

Figure 3.7 The maximum coupling caused by coalescence of six coupled QDs.

The coupling behavior of QDs can be clearly seen from the shape of the wavefunctions in the one-dimensional as well as in the two-dimensional case, as shown in Figs. 3.6 and 3.7. For the case of six square-shaped coupled quantum dots whose side is $2a$ = 20 nm, when the dot separation is 10 nm, coupling between the dots may be already seen, as in the Fig. 3.6 (a). When the dot separation becomes smaller, e.g., 6 nm, coupling between the dots becomes more pronounced, as in Fig. 3.6 (b). Coupling is maximum when the dots completely fuse together (zero separation), as shown in Fig. 3.7, and in this case the QD system looks like a quantum wire.

According to the calculations and the results obtained above, the coupling and energy splitting behaviors depend on separation between quantum dots. Controlling the energy splitting of the system is interesting for the polarization property. Polarization characteristic is to some extent related to the energy splitting and coupling among aligned quantum dots.

3.5.2 Effect of Coupling on the Linear Optical Polarization Property

The energy splitting of any coupled QD system is significant in the direction of the dot alignment. As the number of dots increases, the amount of energy splitting also increases. In two dimensions, if the quantum dots align, say, in the x direction, then the splitting of energy levels is significant in the x direction, there is virtually not much energy splitting in the y direction. Significant energy splitting in the x direction implies dominant linear polarization in the x direction. For a two-dimensional system, the optical intensity due to carrier transitions within the system may be found from the expression:

$$I_{if}^{(\theta)} \propto \int \psi_i(x,y) r_\theta \psi_f(x,y) dxdy \tag{3.12}$$

where r stands for the coordinate of the optical transition, θ stands for either the x or the y direction of polarization of light, ψ_i is the ground-state electron wavefunction, and ψ_f is the ground-state hole wavefunction. If QDs align in the x direction, the major contribution to the optical transition is the x component of the wavefunctions. By using the above equation, the degree of optical polarization anisotropy, or in short the “polarization degree” (PD) for two-dimensional systems may be determined as

$$PD = \left| \frac{I^x - I^y}{I^x + I^y} \right| \tag{3.13}$$

where I^x and I^y are the emission optical intensity in x and y direction, respectively.

3.5.2.1 Single Quantum Dots

First, single quantum dots of an isotropic shape (12 nm×12 nm) as well as elongated quantum dots whose size in the y direction was fixed to 12 nm and that in the x direction varied from 12 nm to 108 nm were investigated. The ground-state wavefunctions of the electron and the hole were calculated by solving Schrödinger equation using the finite-difference method, in which a uniform mesh was used in the x and y directions and 2 nm was equivalent to 1 mesh. The largest matrix size for this two-dimensional calculation was 3600 × 3600. The calculated electron wavefunction for isotropic quantum dots and elongated quantum dots are as shown in Fig. 3.8 and 3.9 respectively. Here, x and y directions correspond to the $[1\bar{1}0]$ and $[110]$ directions, respectively.

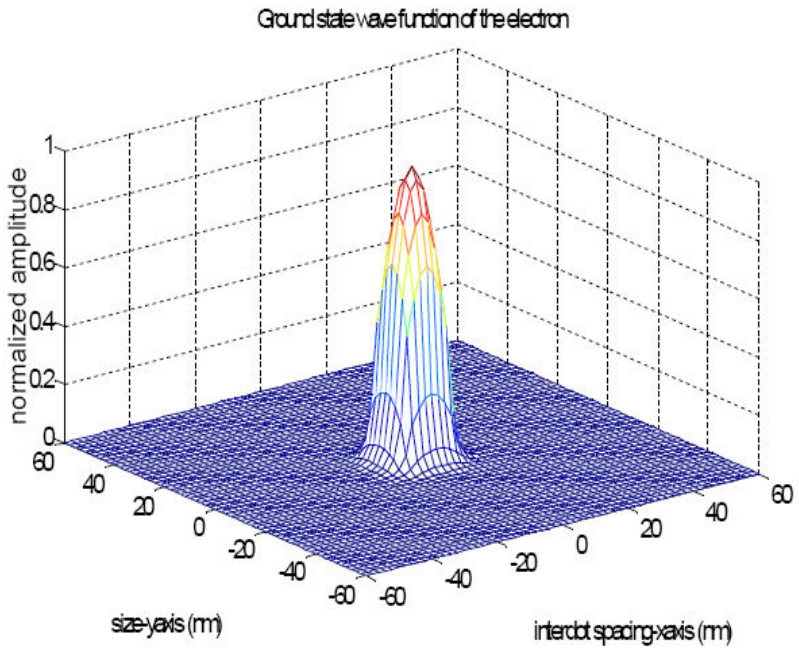

Figure 3.8 The ground-state electron wavefunction of an isotropic single quantum dot whose size is 12 nm × 12 nm.

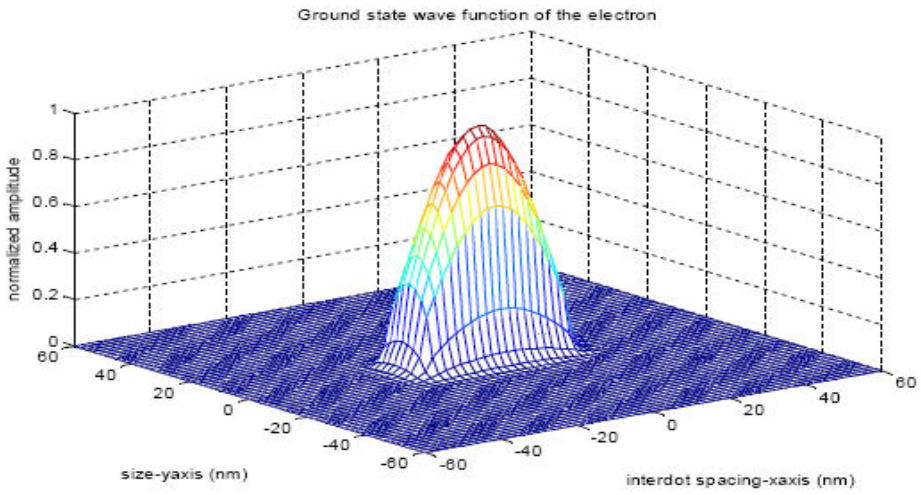

Figure 3.9 The ground-state electron wavefunction of an elongated QD (the size in the *x* direction was elongated to 36 nm while that in the *y* direction was maintained at 12 nm).

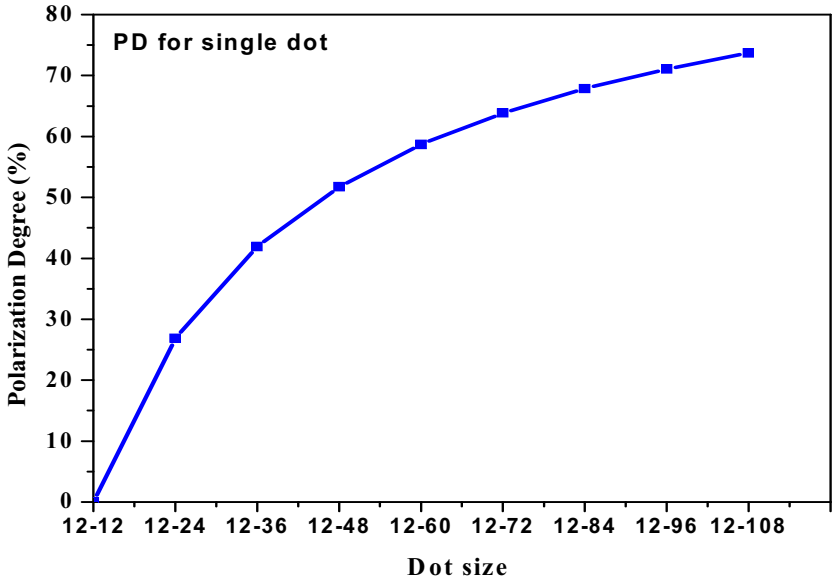

Figure 3.10 The polarization degree for a single QD whose size in the *x* direction was elongated from 12 nm to108 nm while that in the *y* direction was maintained at 12 nm.

Table 3.2: The polarization degree vs. dot aspect ratio of single QDs.

Dot aspect ratio (nm-nm)	**Polarization degree (%)**
12-12	0
12-24	24.88
12-36	41.92
12-48	51.97
12-60	58.92
12-72	64.14
12-84	67.61
12-96	71.85
12-108	73.96

The above calculation results (Table 3.2) show that when the size of the quantum dot is isotropic, that is, the size in the *x* and *y* directions are the same, then the transition probability in the *x* and the *y* directions are the same. For this case, the degree of polarization is zero. When the size of the quantum dot is elongated in the *x* direction, the transition in the *x* and the *y* directions are not the same. Elongated quantum dots thus show a certain degree of linear polarization (PD $\neq$ 0). When the dot size is elongated more and more in a certain direction, the PD increases.

3.5.2.2 Binary Quantum Dots

The wavefunctions in Figs. 3.12 and 3.13 are the calculation results which show the ground-state electron wavefunction of binary quantum dots which are aligned in the *x* direction, that is, the $[1\,\bar{1}0]$ direction. There was some barrier thickness between the two quantum dots and this thickness needed to be taken into account in the calculation. The spatial separation of the barrier strongly affects the "overlap integral" Γ, which measures the amount of overlapping between electron and hole wavefunctions and is defined as

$$\Gamma = \frac{\int_{-\frac{a}{2}}^{\frac{a}{2}} \int_{-\frac{d}{2}}^{\frac{d}{2}} \psi_e(x,y) \cdot \psi_h(x,y) dxdy}{\int_{-\frac{a}{2}}^{\frac{a}{2}} \int_{-\frac{d}{2}}^{\frac{d}{2}} dxdy} \tag{3.14}$$

where ψ_e is the ground-state wavefunction of the electron and ψ_h is the ground-state wavefunction of the hole. By integrating the dot product between the electron and the hole wavefunctions over all space, the overlap integral for the electron and hole wavefunctions was obtained. Here, *d* and *a* are the spatial separation and the size of the QDs, respectively. The schematic diagram for the above equation is depicted in Fig. 3.11.

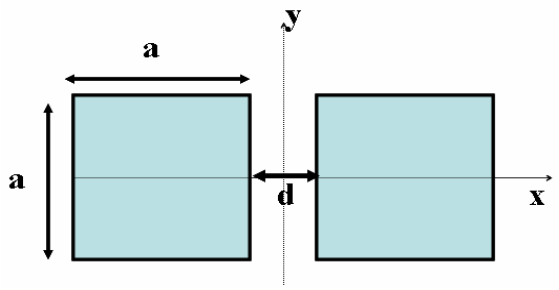

Figure 3.11 Schematic diagram of binary quantum dots, each of size **a**×**a** nm^2 and interdot spacing **d** nm.

Finally, the polarization degree for the bi-QDs may be calculated by

$$PD = \Gamma \times \left| \left(\frac{I^x - I^y}{I^x + I^y} \right) \right| \tag{3.16}$$

Eq. 3.16 was modified from Eq. 3.13 only by the multiplicative factor Γ, which needs to be taken into account for any coupled-QD systems. The degree of linear polarization (PD) of the binary quantum dots was calculated by using this last formula. Next, the number of quantum dots was increased in the *x* direction, while for the *y* direction only one dot was maintained. The thickness of the barrier between the two quantum dots in the *x* direction plays important role to determine the polarization degree of binary quantum dots. When the thickness of the barrier is smallest, the highest PD is obtained. The polarization degree tends to increase when the spatial separation between the two quantum dots decreases (see Table 3.3 and 3.14).

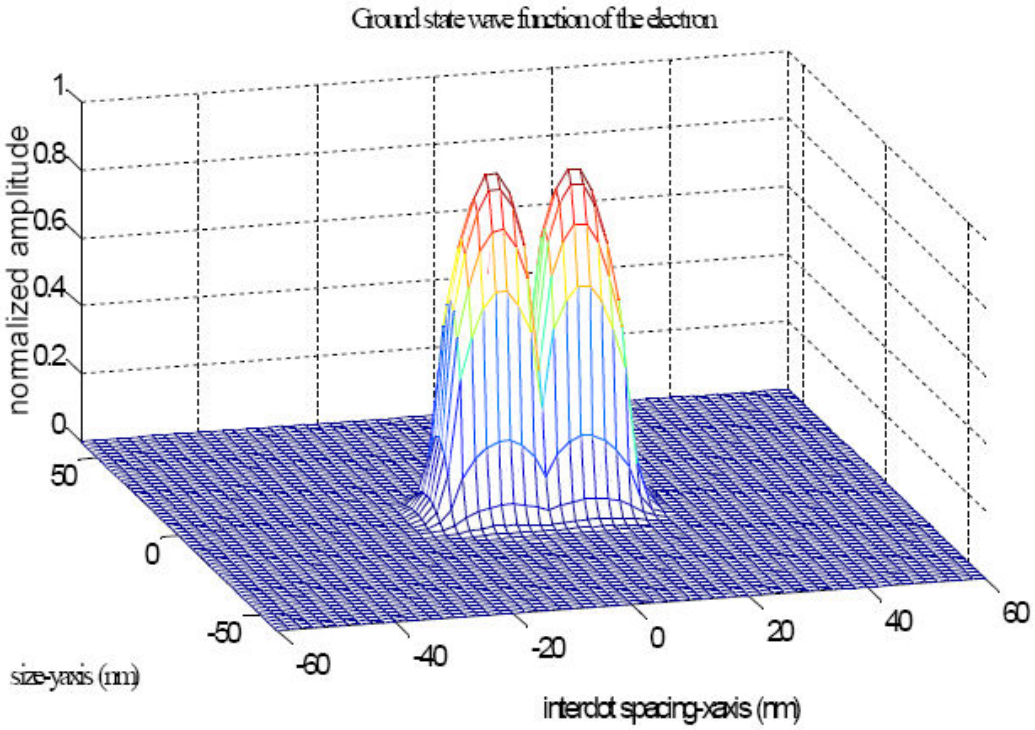

Figure 3.12 The ground-state electron wavefunction of binary quantum dots, each of size 12 nm × 12 nm with an interdot spacing of 2 nm.

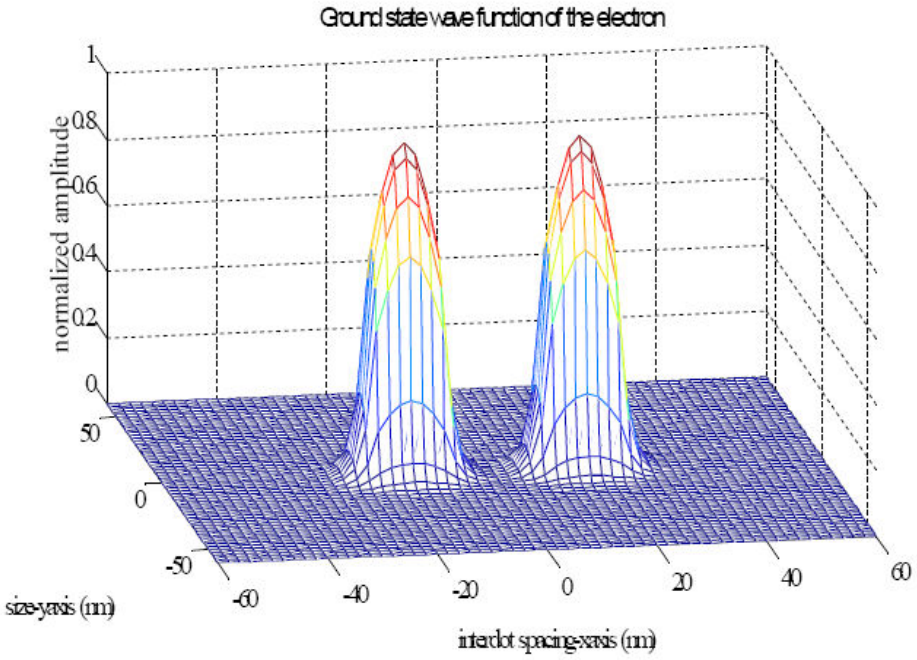

Figure 3.13 The ground-state electron wavefunction of binary quantum dots, each of size 12 nm × 12 nm with an interdot spacing of 12 nm.

Table 3.3: The polarization degree of binary quantum dots with various interdot spacings. The middle number refers to the interdot spacing that is, the barrier width between the dots.

Dot structure (nm-nm-nm)	**Polarization degree (%)**
12-0-12	26.88
12-2-12	13.44
12-6-12	6.12
12-10-12	4.40
12-14-12	3.51
12-18-12	2.95
12-22-12	2.55

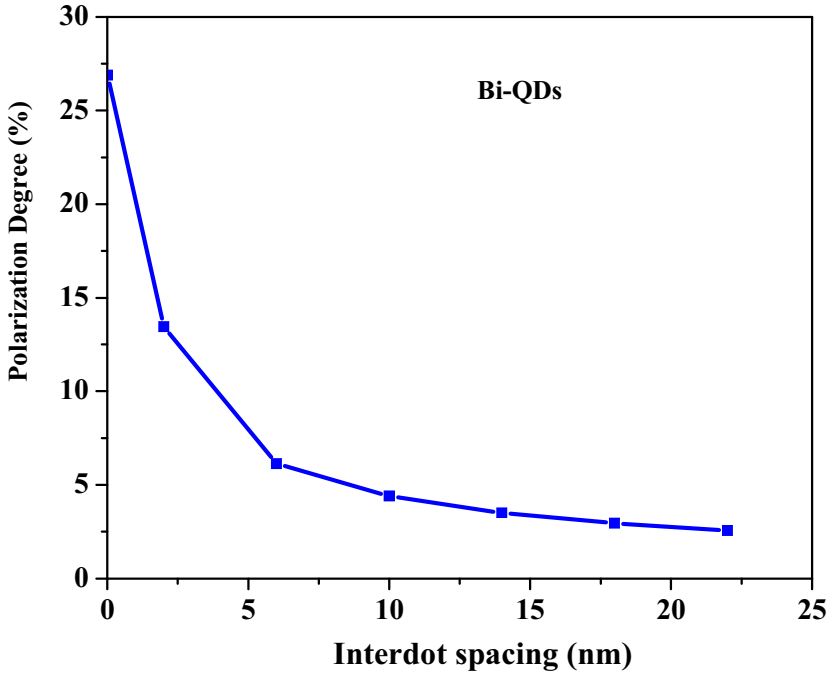

Figure 3.14 The polarization degree of binary quantum dots vs. their interdot spacing (the dot size was fixed at 12 nm × 12 nm and the interdot spacing was varied from 0 nm to 22 nm).

Table 3.4: The polarization degree of binary quantum dots with various dot sizes. The dot size was varied from 8 nm to 44 nm while the interdot spacing was fixed at 2 nm.

Dot size (nm-nm)	Polarization degree (%)
8-8	20.41
12-12	13.44
16-16	9.52
20-20	7.11
24-24	5.22
28-28	4.41
32-32	3.61
36-36	3.02
40-40	2.54
44-44	2.18

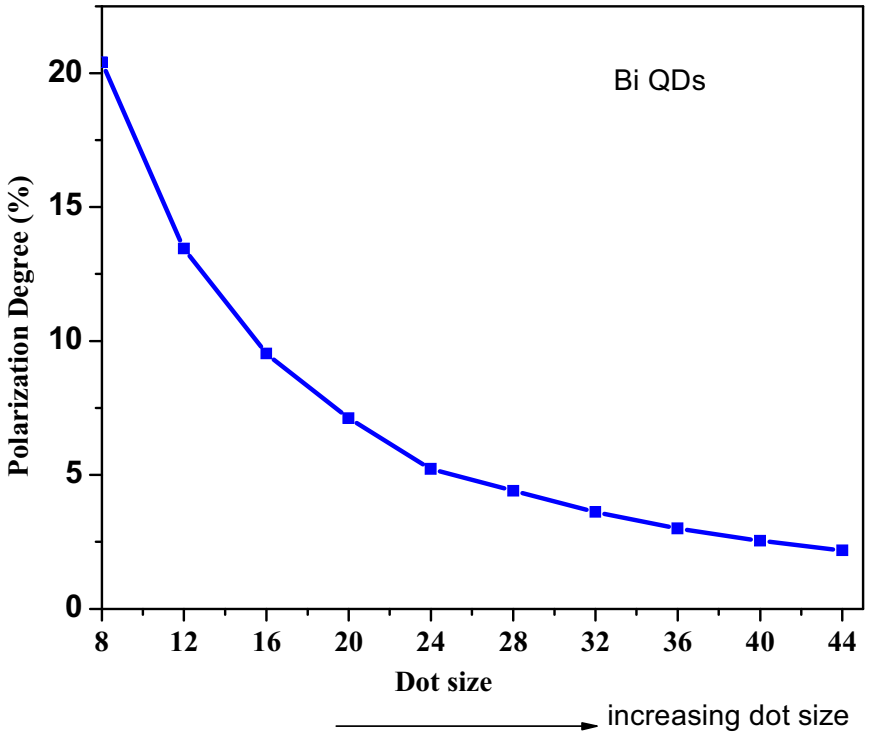

Figure 3.15 The polarization degree of binary quantum dots with various dot sizes. The dot size was varied from 8 nm to 44 nm while interdot spacing was fixed at 2 nm.

3.5.2.3 Increase of Polarization Degree with Number of QDs

Next, the number of the quantum dots aligned in the *x* direction was varied from two to seven quantum dots. In other words, the number of quantum dots was increased in the *x* direction and for the *y* direction the only one quantum dot was maintained. In this case, the thickness of the barrier, or the spacing, between aligned quantum dots was maintained at 2 nm. The degree of linear polarization of multiple aligned quantum dots was still calculated by using Eq. (3.16). It was found that when the number of quantum dots increased, the degree of polarization also increased, as shown in Table 3.5 and Fig. 3.16.

Table 3.5: The polarization degree vs. the number of QDs aligned in the *x* direction. The dot size was maintained at 12 nm × 12 nm (isotropic shape) and the interdot spacing between adjacent QDs was fixed at 2 nm. The number of dots increased in the *x* direction**.**

Number of dots	Polarization degree (%)
1	0.00
2	13.44
3	22.20
4	26.12
5	28.20
6	29.44
7	30.87

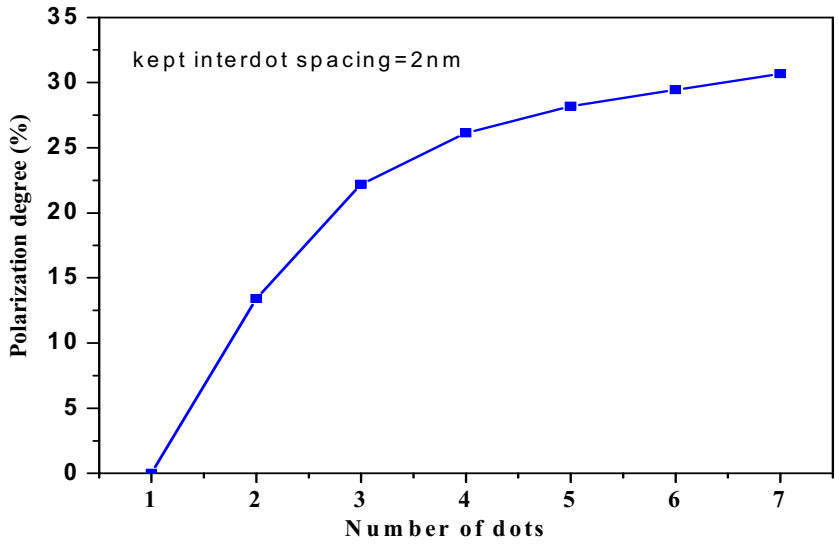

Figure 3.16 The polarization degree vs. the number of QDs aligned in the *x* direction. The dot size was maintained at 12 nm × 12 nm (isotropic shape) and the interdot spacing between adjacent QDs was fixed at 2 nm. The number of dots increased in the *x* direction**.**

3.6 Conclusion

The degree of linear polarization (PD) of the PL spectrum emitted from QD system was theoretically calculated by using the Schrödinger equation implemented using the finite-difference method (FDM). The degree of polarization is zero when the single dot has an isotropic shape. A certain degree of polarization is obtained when the dot is elongated in one direction. For binary quantum dots and linearly aligned quantum dots, the polarization degree strongly depends on spatial separation between adjacent dots. When the interdot spacing is smallest, the highest degree of polarization is obtained. The size of the individual quantum dots in the coupled system also affects the degree of polarization. See Table 3.5 and Fig. 3.15. Smaller quantum dots show a larger degree of coupling, and hence a larger degree of polarization. For larger isotropic quantum dots, the wave function is confined in the dot region and so the amount of wave function overlapping is small. In conclusion, to get a larger degree of linear polarization from the aligned quantum dots, a smaller dot size, and a very close spacing between adjacent dots, and a long dot alignment are preferred.

CHAPTER IV

PHOTOLUMINESCENCE SPECTROSCOPY

4.1 Photoluminescence

As mentioned in the Chapter II, photoluminescence (PL) is a well-known process and an important physical phenomenon used to characterize semiconductor structures. The main idea of PL spectroscopy is investigating the transition of photogenerated carriers between the valence-band and conduction-band states and the results reflect the conduction-band and valance-band structures, the dynamics of the carrier relaxation and recombination, the excitonic and the many-body effects, etc. [54-59]. However, the PL spectrum, which gives a number of such important information, is sometimes difficult to extract. In brief, PL occurs when a sample absorbs light of some wavelength and emits light at a specific wavelength depending on the material's specific structure, composition, and quality. This chapter will further describe the nature of photoluminescence, in relation to semiconductor materials, and its use in understanding structures under investigation.

This section first describes physics of PL by using the simplest electron picture. Then, a description using electron and hole energy bands and excitons will be examined. This more complicated description helps explain PL features of samples with complicated structures, such as those examined in this project work.

Photoluminescence is one of optical luminescence techniques which involve a system excited by electromagnetic (EM) radiation. Lasers can provide sufficient power to excite the carriers in the sample. Typically, the incident light used to excite the sample comes from a laser source with energy of $\hbar\omega_{laser}$. As the incident light (EM radiation) strikes on the sample, it causes electrons to jump up into excited states, as shown in Fig. 4.1, which is a typical energy diagram used to explain this process. When an excited electron returns to its initial state, it may generate a photon with energy $\hbar\omega_{PL}$ (and possibly multiple phonons with combined energies of $\hbar\Omega_{phonon}$) [60-64]. Due to the law of energy conservation, this can be expressed as

$$\hbar\omega_{laser} = \hbar\omega_{PL} + \hbar\Omega_{phonon} \tag{4.1}$$

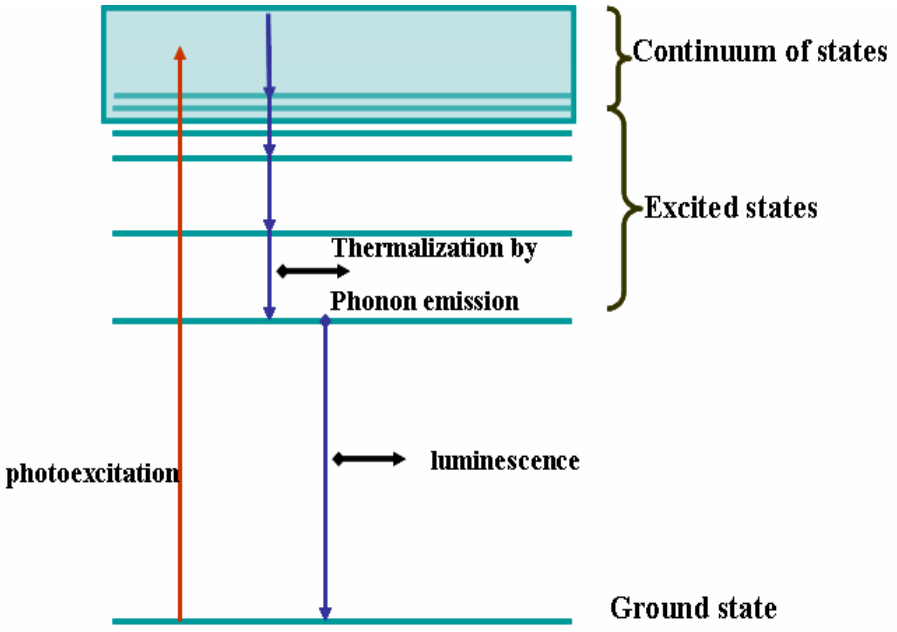

Figure 4.1 A typical energy diagram for electron system. As the incident light (EM radiation) strikes on the sample, it causes electrons to jump up into excited states.

Continuous-wave (cw) laser excitation was used to excite all samples in this project work. In this case, luminescence can be considered as a steady-state phenomenon, that is, the sample interacts with the excitation source and emits light continuously. The first part in the above process is optical absorption of the incident light. The amount of photon absorption by the material depends on the incident photons' wavelength (energy) of the source of excitation. Eq. 4.2 addresses the theoretical prediction of the absorption coefficient α for a direct-bandgap semiconductor.

$$\alpha = A(\hbar\omega + E_{gap})^p = A(\frac{\hbar c}{\lambda} + E_{gap})^p \qquad (4.2)$$

where A and p are constants for the particular material, $\hbar\omega$ is the photon energy of the laser light, and E_{gap} is the bandgap energy of the structure under excitation. Once the optical absorption has excited an electron to a higher energy state, the electron can relax to a lower energy state. Different processes may take part in this relaxation, which can be categorized as either *radiative processes* (such as PL) or *non-radiative processes* (such as phonon emission, capture by deep centers, or the Auger effect).

The rate of emission for radiative recombination depends on the amount of electron excitation via the absorption of this light. Eq. 4.3 explains the recombination process of the PL.

$$R = n_i n_f P_{if} \tag{4.3}$$

where n_i and n_f are the density of initial and final (empty) states, respectively; and P_{if} is the probability of a transition from the initial state to the final state.

Generally, the higher-energy excitation causes more phonons to be emitted before the luminescence occurs. Similarly, lower excitation energy tends to induce fewer phonon emissions. If the excitation energy is less than the energy difference between the ground state and the first excited state, then no optical absorption will occur, resulting in no PL. The above electron picture is not sufficient to explain many PL characteristics seen in structured semiconductors. A better explanation considers the optical absorption as a transition from the valence band to the conduction band. Emission then entails the movement of an electron from the minima of the conduction band to the maxima of the valence band. The optical absorption across bandgaps for a direct-bandgap material and an indirect-bandgap material are both shown in Fig. 4.2. As described in the Chapter II, the conduction band and the valence band correlate to free carriers, that is, electrons and holes, respectively. In fact, photoluminescence (Fig. 4.3) can be considered as the radiative recombination of conduction-band electrons with valence-band holes in semiconductors. When the excitation energy is less than the bandgap energy, no optical absorption will occur, and hence no PL.

PL can be observed from samples with structures that are more complicated in composition than just a bulk semiconductor material. It can be used to investigate how well the samples are grown, and to verify the material composition. This is because the energy differences measured by PL change with impurities and structures, as illustrated in Figs. 4.2, 4.3 and 4.4.

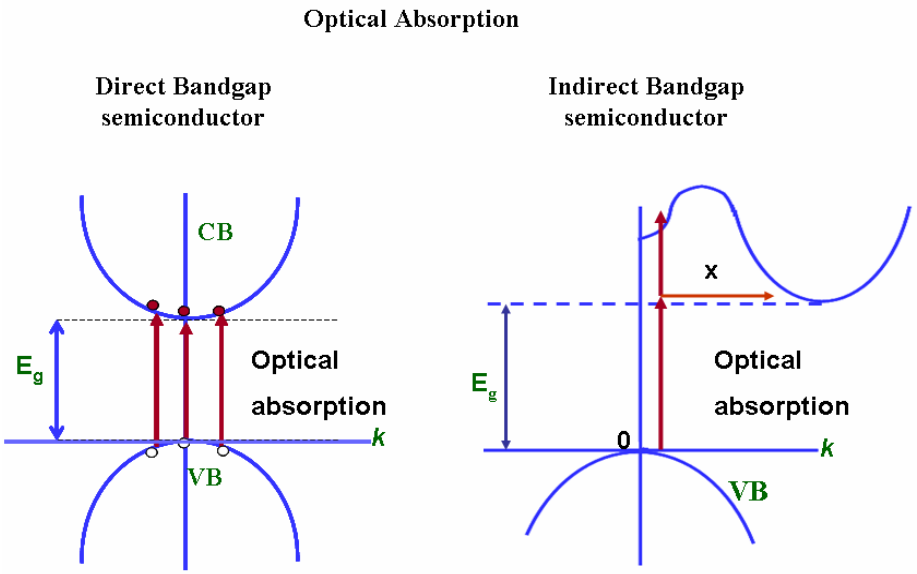

Figure 4.2 A typical energy absorption diagram in direct- and indirect-bandgap semiconductors: As the incident light (EM radiation) strikes on the sample, it causes electrons to jump up from the valance band into the conduction band. (After P. Bhattacharya, *Semiconductor Optoelectronic Devices*)

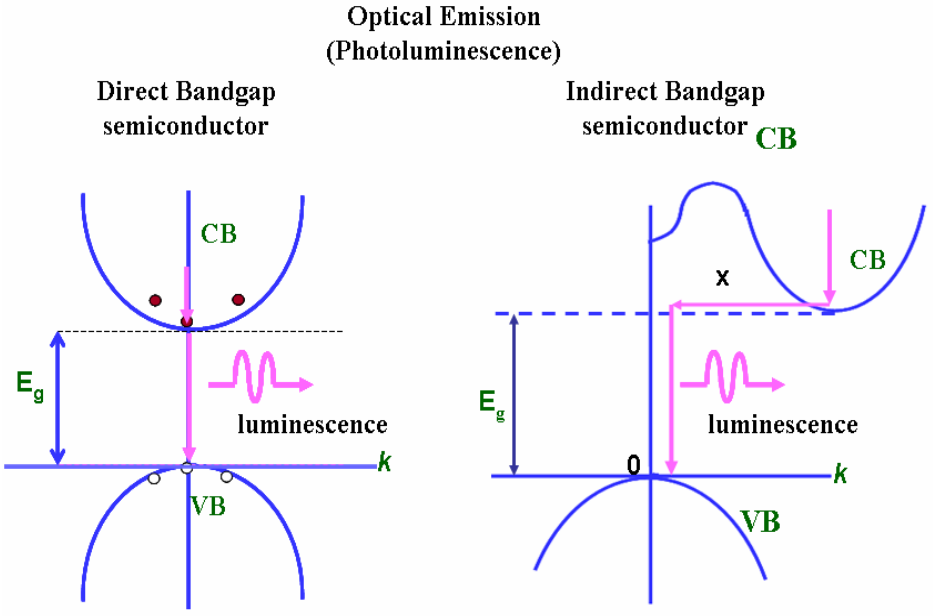

Figure 4.3 A typical energy emission diagram in direct- and indirect-bandgap semiconductors: As electrons come back to the initial state in the valence band, the electron and the holes recombine and emit photoluminescence (After P. Bhattacharya, *Semiconductor Optoelectronic Devices*)

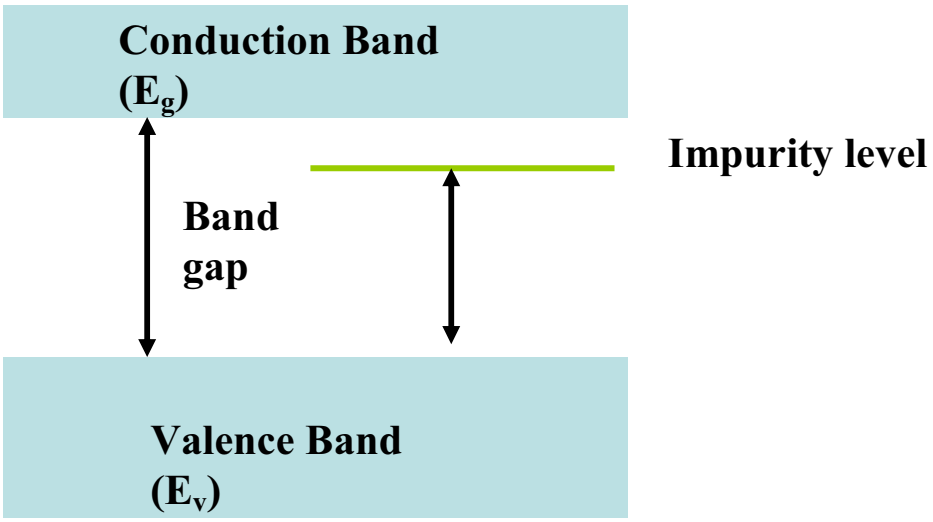

Figure 4.4 Bandgap energy changes due to impurity and other effects (After M. A. Omar, *Elementary Solid State Physics*)

4.2 Optical Excitation

With laser light to be used in the PL spectroscopy, three parameters must be considered: wavelength (excitation energy), intensity (excitation power), and polarization. There are two ways to optically excite quantum dots. These are *non-resonant excitation*, and *resonant excitation*.

In non-resonant excitation, which corresponds to excitation above GaAs bandgap in our case (Fig. 4.5), the energy of the laser was tuned above the GaAs bandgap, in particular, 1.87 eV (660 nm) was used. Electrons and holes were thus generated in the GaAs matrix surrounding the InAs quantum dots. In a random manner, a fraction of these carriers were captured first by the *wetting layer*, which behaves as a thin quantum well. They then fell into the higher excited states of quantum dots, finally most of them reached the electron and hole ground states before recombining. For weak excitation, the dominant intraband relaxation mechanism inside the quantum dot is thought to be phonon emission [52], although the relaxation rates typically seen are faster than theoretically expected. When the carrier density is higher, Auger processes (multi-carrier scattering) can also manifest. Above-bandgap excitation is convenient for several reasons. First, it is relatively efficient, since a large area of GaAs acts as the absorber and funnels the carriers into the quantum dots. For continuous-wave (cw)

excitation, appropriate pump powers were often just tens of microwatts in the setup used in this project. Also, since the laser wavelength (often 650 nm or 700 nm) was far detuned from the quantum-dot emission wavelength (900 nm), the reflected laser light passing through the beam splitter, which was in the same direction as the luminescence, was easily rejected using a color filter with 90**%** efficiency at the emission wavelength. Finally, by increasing the laser power, it was straightforward to investigate the multi-particle states of a quantum dot.

In resonant excitation, the laser is tuned to a higher transition energy within the quantum dot, as shown also in Fig. 4.5. A much larger laser power is required than for the above-band excitation, since the absorption cross-section of a single quantum dot is very small. In this project, all measurements were done under the non-resonant excitation (above-bandgap excitation).

The intensity of the PL signal depends on the excitation laser power also. The intensity of the excitation beam (the power of the laser) affects the PL peak intensity in a linear fashion until a saturation intensity is reached. Although this general description applies to all samples, the point at which these different features occur is sample-dependent.

In the non-resonant excitation above the GaAs bandgap used in this project work, the laser had the photon energy higher than the GaAs bandgap energy. The laser excited the carriers within the barrier region and diffused towards the InAs QDs in order to be captured and consequently relax and recombine at the QD ground energy state. Because the spin-flip process occurred in the GaAs region, the carriers did not have enough memory to recognize the polarization state of the excitation laser. Therefore, the measured polarization state of aligned quantum dot arrays was independent of that of the excitation source.

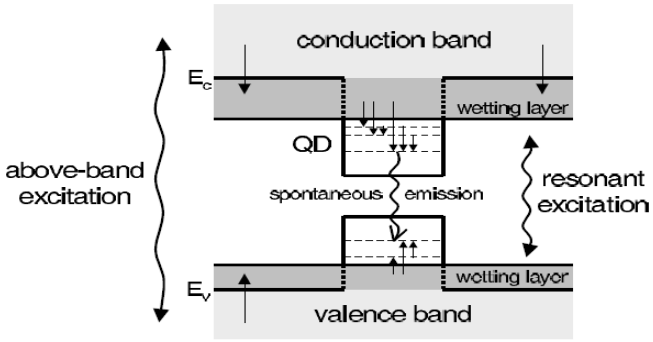

Figure 4.5 Non-resonant optical excitation. (After C. M. Santori, *Generation of Nonclassical Light Using Semiconductor Quantum Dots*)

4.3 Macro-Photoluminescence

The main tool for optical characterization in this research work was the photo-luminescence (PL) spectroscopy. A schematic of the macro-PL experimental setup is shown in Fig. 4.6. The samples were excited by the 514-nm line of an Ar^+ laser. The PL signal was resolved by a 1-meter monochromator. Typically, the entrance and the exit slit widths are 0.5 mm. The resolved light signal was detected by a liquid-N_2-cooled InGaAs detector (Hamamatsu's G7754-01 with 0.1-mm^2 active area). An optical beam chopper and the associated lock-in amplifier were used to enhance the signal by the standard lock-in technique. For low-temperature and temperature-dependent measurements, the sample was mounted on the cold finger of a closed-cycle cryostat.

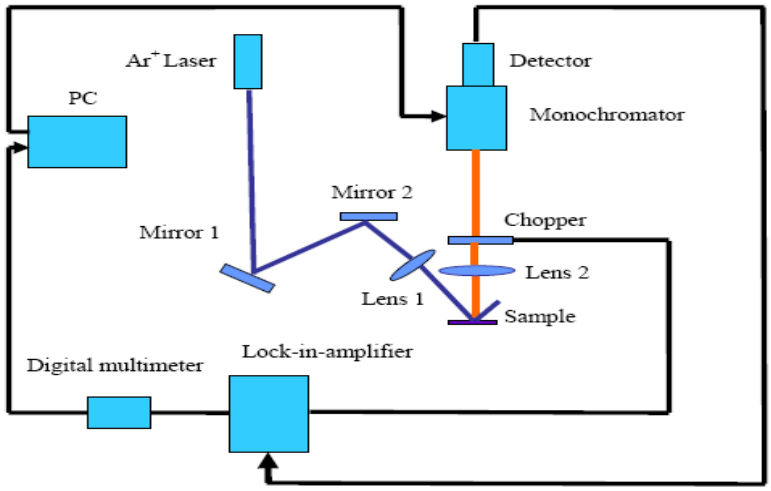

Figure 4.6 Macro-photoluminescence setup.

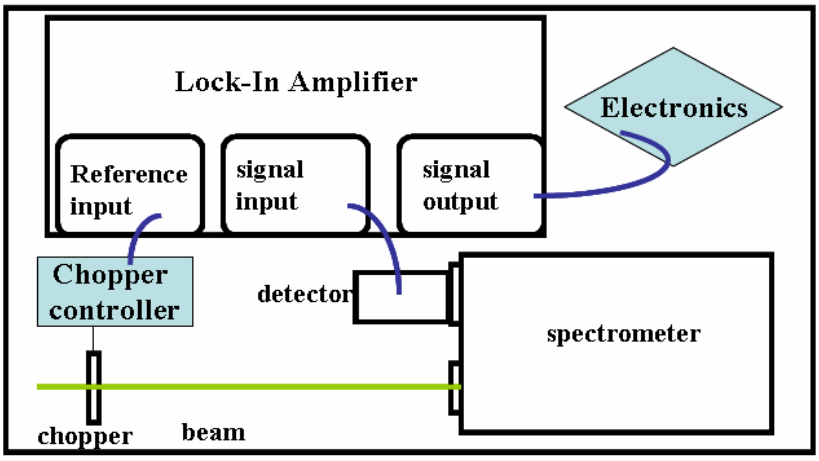

Figure 4.7 Standard lock-in technique.

Figure 4.7 shows the function and the essential parts of the lock-in technique. An optical chopper renders the optical beam into a series of square-wave pulses. This can be positioned either close to the laser source or immediately after the sample. With earlier placement of the chopper in the optical path, less noise is included in the chopped beam. This detection technique averages away any random non-chopped signal. The chopper controller sends a reference signal (square wave with the frequency that the beam is being chopped) to the lock-in amplifier. This sets the frequency to be detected by the lock-in and fixes the timing of the signal to allow phase-sensitive detection to occur.

4.4 Micro-Photoluminescence

4.4.1 Cryogenics

All the samples were held in a continuous-flow liquid-helium cryostat. A diagram of a typical continuous-flow cryostat is as shown in Fig. 4.8. The cryostat itself was mounted on a fairly steady two-axis translation stage, which allowed horizontal and vertical adjustments of the cryostat position. The sample was attached to a cold finger in a vacuum chamber.

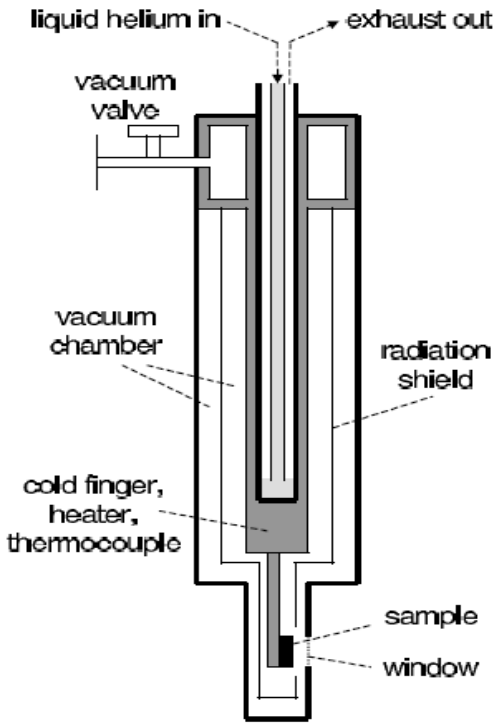

Figure 4.8 Cross-section of the cryostat.

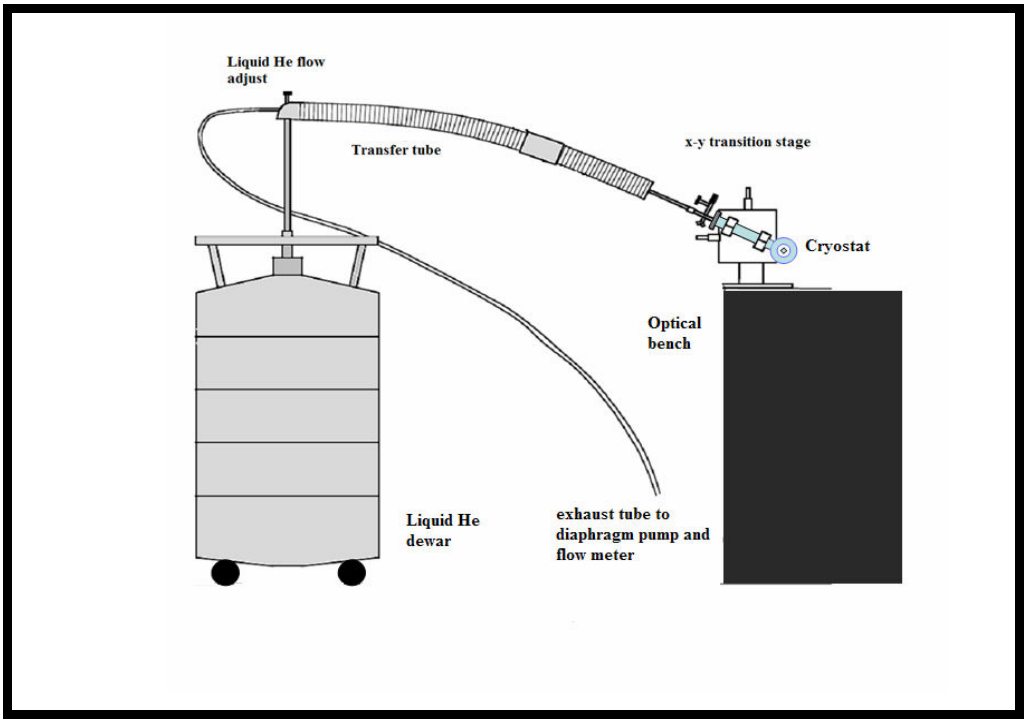

Figure 4.9 (a) A schematic diagram of the cooling system for the sample.

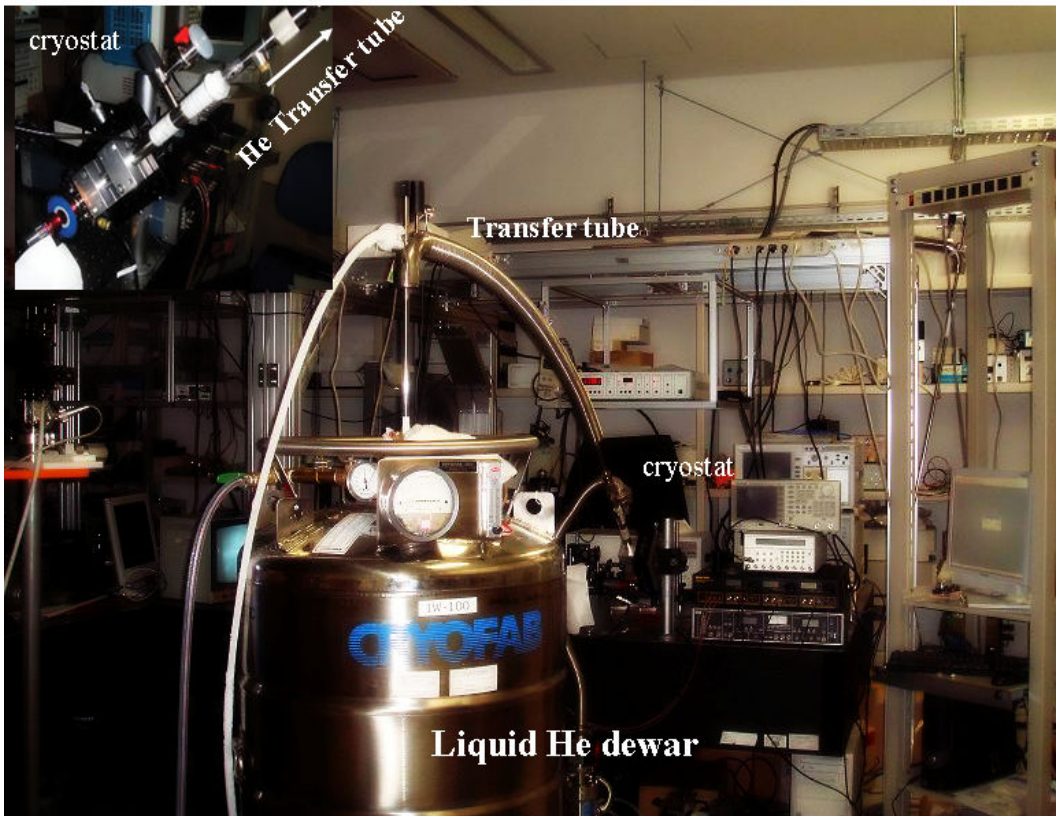

Figure 4.9 (b) Photo of the cooling system for the sample used in this project.

Liquid helium was delivered from a dewar, through a transfer tube, to the inside of the cold finger. The helium waste gas then exited from the cryostat. A window in the outside of the vacuum chamber allowed optical access to the sample. For this cryostat, the waste helium was pumped out through an outer shield of the transfer tube, so that the incoming helium was insulated, enhancing the measurement efficiency. The helium consumption rate for this cryostat could be around 1 L/hr.

4.4.2 Optical Setup

Measuring the light emission from an aligned quantum dot system can be done with a standard procedure. The essential components of the setup including the excitation part for sample and the part used to collect emission from quantum dots are shown in Fig. 4.11 (a) and (b). Only one 45%:45% beam splitter was used for all of the optical excitation path, the emission path and the illumination path. For the excitation part, 45% of the laser transmitted from the beam splitter was incident on the sample. The laser excitation was usually applied for normal excitation on the sample. By doing so, the first advantage was that the optical path of the laser and of the luminescence was the same. Also, the alignment for the emission part could be easily done. The laser spot size on the sample was typically about 1 to 2 μm in diameter. At the same time, 45% of the pump laser was passed through the beam splitter and was incident upon the photodetector. The amount of the laser light impinging on the photodetector, measured by an optical power meter, was the same amount as that of the laser which stroke upon the sample. By measuring the laser spot on the photodetector, the amount of laser that was incident upon the sample could be known. The semiconductor laser used in this setup provided a wavelength in the red-wavelength region of 660 nm. The highest optical power of the laser used was 60 mW.

An illumination technique was used to visualize the sample during the experiment (see Fig. 4.10). Light coming from the light source was captured by the first lens to produce a collimated beam, and then passed into a diaphragm. By adjusting the aperture of the diaphragm, the amount of light could be controlled. For the illumination part, the second lens helped to focus the light at the back of the objective lens after passing through a beam splitter. After passing through the objective lens, the light impinged on the sample. After that, the light reflected back from the sample came back in the same direction as the incident light. Another beam splitter (which is normally used with the visible light region) in the illumination optic path sent about half of the light to another path to the CCD camera. The third lens in front of the camera focused the reflected light from the sample to the slit of the CCD camera. Alignment of the optical components utilizing a microscope to optimize illumination was carried out following the Kohler illumination rules. The laser beam shape, size, and location on the sample were checked by monitoring the reflection

image on the CCD camera, on which the laser beam was illuminated together with a white light illumination by a tungsten lamp.

The emission from the sample was reflected in the same direction as the excitation laser through an objective lens, whose numerical aperture was 0.45 and focal length was 200 mm. There was a flip-mirror that sent the luminescence to the spectrometer, and the illumination light from the light source was already blocked by flipping up the mirror.

Another lens (focal length of 5cm) was placed in front of the spectrometer to collect all the PL emission. The purpose of placing this lens in front of the spectrometer was to collect all PL signal and focusing it to the spectrometer, and the *f*-number of this lens must match with that of the spectrometer. It was advantageous to insert two lenses after the sample so that the light emission after passing through the microscopic lens could create parallel rays, allowing Lens 2 (L2) to easily focus the light signal onto the spectrometer's slits. Lens 2 (L2) was placed on a hinge mount in order to be easily adjusted. Although it was assumed that the PL emission was from a point source, adjustment of the objective lens was not possible in this setup, however, since the lens L2 could always focus two parallel rays. For instance, the signal emitted from the sample could be affected by both the thickness and whether the signal originated from deep within the sample or near the surface, depending on the sample under investigation. Also, the index of refraction, which affected the divergence of the PL signal leaving the sample, was also sample-dependant. Hence, only L2 was needed to be moved to compensate for different samples' effects, without changing the position of objective lens. Therefore, this two-lens configuration facilitated matching the spectrometer's *f*-number and focusing the PL signal into the spectrometer.

In addition to the lenses shown in the above figures, it was practical to have multiple apertures in the system for alignment purposes, as shown in Fig. 4.11. Although these were meant to be static parts of the experiment, they could be moved and changed as needed. These apertures could block some of the laser light from reaching the sample; thus, their position and size would change the eventual intensity impinging on the sample. It is important for the user to be aware of the multiple

components in the system and the effect they have on the actual optical intensity reaching the sample.

Optical filters are another component that will affect the overall outcome of the experiment. The two most common types of filters used are neutral density (ND) filters and color filters. Figure 4.11 shows a color filter placed in front of the spectrometer's slit and an ND filter in front of the laser light before striking the sample. ND filters uniformly reduce the intensity of light over a relatively broad wavelength range. Moreover, the power incident on the sample was varied by introducing ND filters in the path of the incident pump beam, allowing the pump power to be varied from nanowatts to microwatts. Color filters either block or transmit specific wavelengths. These come in a few varieties: high-pass (which allows wavelengths higher than a certain threshold to pass through virtually unaffected), low-pass (which allows wavelengths lower than a threshold wavelength to pass through virtually unaffected), or band-pass (which allows wavelengths within a certain range pass through virtually unaffected). The ND filter was used to reduce the intensity of the laser beam; or to reduce the intensity of the PL signal entering the spectrometer. Color filters were used to block the laser beam's reflection or other stray light from entering the spectrometer, which would thereby either distort the PL spectra or saturate the detector.

Varying the spectrometer's slit widths (entrance and exit) produces several changes in the acquired spectra. The slit width affects the spectrometer's resolution and thus the resolution of the data. As the PL spectra of interest have linewidths much greater than the spectrometer resolution, the slits actually control the amount of light entering the spectrometer and the detector chamber. If the PL was not properly focused into the slits, having the slits closed too tight would prevent any PL from entering the spectrometer even if there is a signal that could be detected. If viewing a weak signal, having the slits too narrow might make the signal-to-noise ratio too small, making the spectra difficult to analyze. Conversely, if measuring a strong signal, having the slits too wide could saturate the detector, or at least push it into the nonlinear regime. Although ND filters could be placed into the system to prevent the latter, sometimes the former would require wide slits. The spectrometer's resolution has been measured using laser lines, which have widths much smaller than 1 nm. As shown in Fig. 4.11(a) and (b), the spectrometer consists of a 0.5 m monochromator

(Acton Spectra Pro 2500i) followed by a liquid-nitrogen-cooled CCD camera. The monochromator has three gratings, with groove densities 600 mm^{-1}, 1200 mm^{-1}, and 1800 mm^{-1}, giving approximate spectral coverage of 50 nm, 20 nm, and 10 nm, respectively. The highest resolution one can obtain with the 1800 mm^{-1}-groove grating is about 0.02 nm. The grating was rotated with high precision by a motor, controlled by a program through a computer. A mechanical shutter between the monochromator exit and the CCD camera was used to control exposure times. The light was sent to the monochromator using focusing lens. Since a typical entrance slit width for the highest resolution was only 15 μm, when collecting emission from objects containing several hundred quantum dots, the emission spectrum had a broadband appearance. In this case, all we can see is the overall distribution of quantum-dot emission energies.

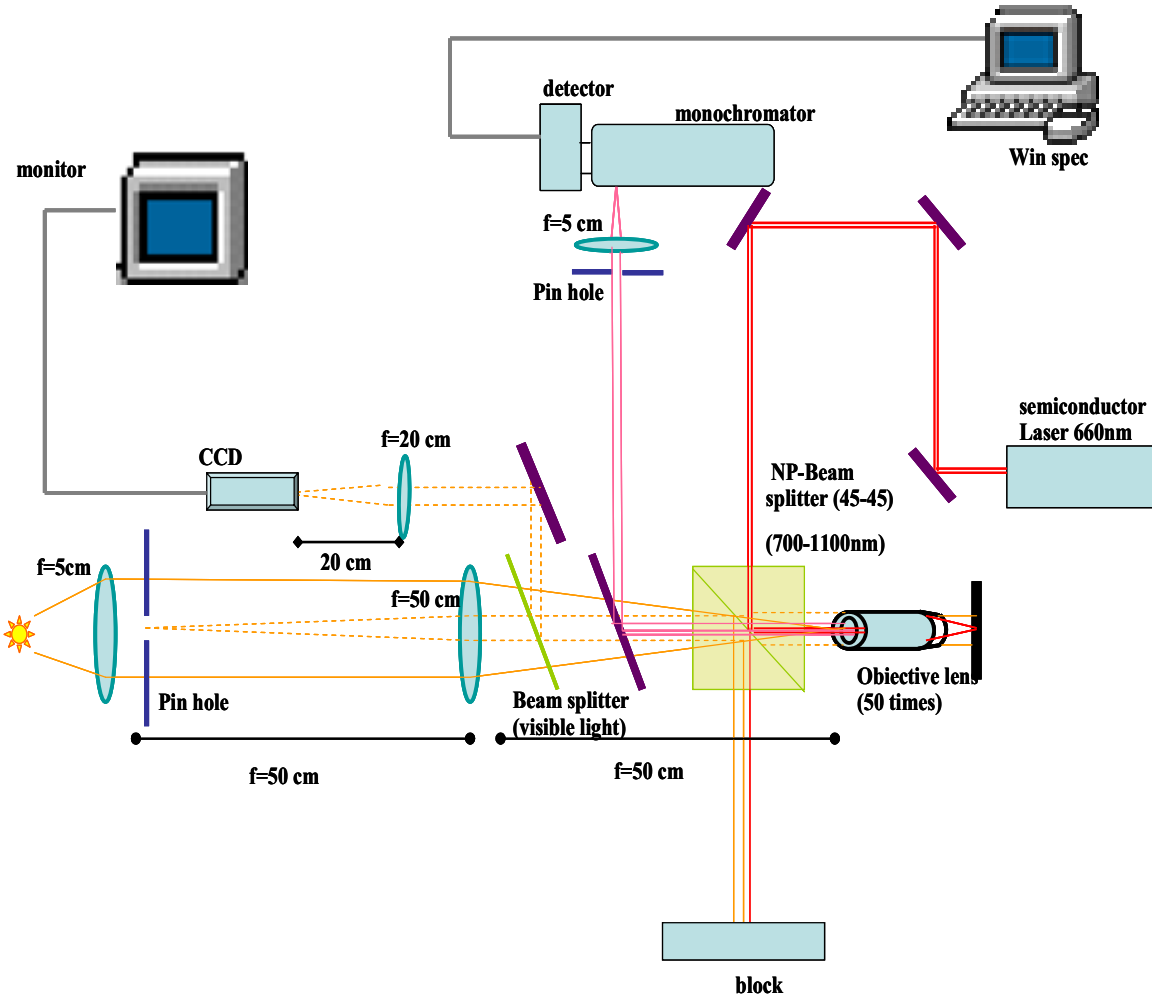

Figure 4.10 A schematic diagram of the micro-PL setup.

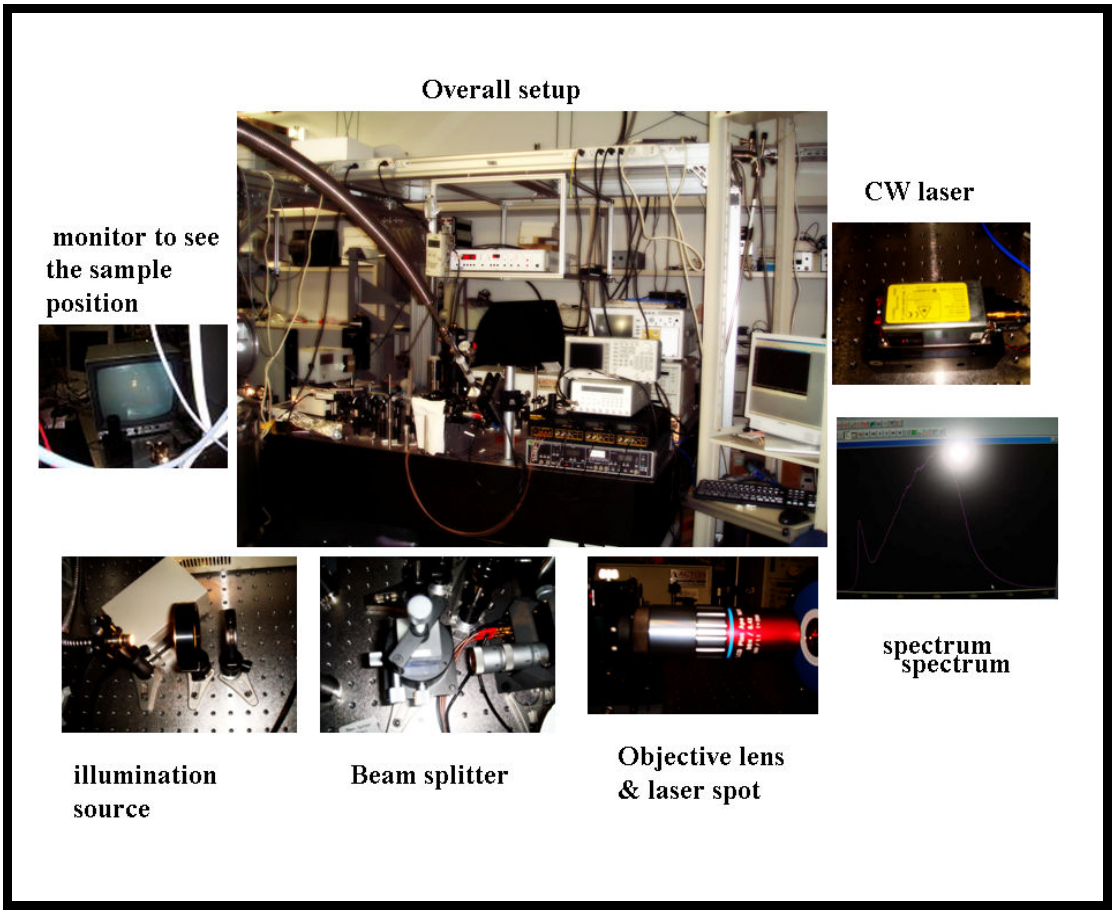

Figure 4.11(a) Photo of the micro-PL setup and its components.

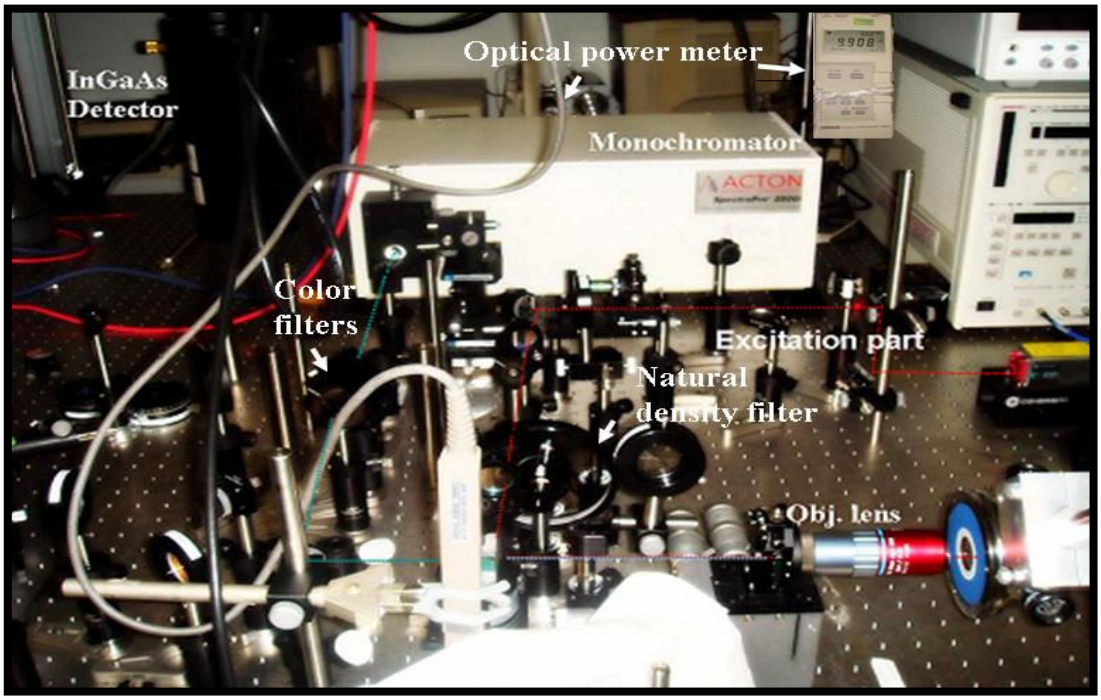

Figure 4.11 (b) Close-up photo of the micro-PL setup and its components.

4.4.3 Temperature Effect

An advantage of room-temperature measurement was that it can allow samples to be changed easily. These features are important for systems used in sample quality control. However, many effects in semiconductor materials can be examined only at cryogenic temperatures. For instance, phonon scattering reduces the lifetime of the carriers so that room-temperature PL of excitons is not possible. The linewidth of the PL is also broadened by these same effects for quantum-dot structures. Hence, it is practical to have the experimental arrangement such that either rapid room-temperature or more sensitive low-temperature measurements can be made. Using the aforementioned lens pair for the PL beam allowed minimal changes in the experimental layout when changing from one temperature measurement to the other, as demonstrated in the following Fig. 4.12.

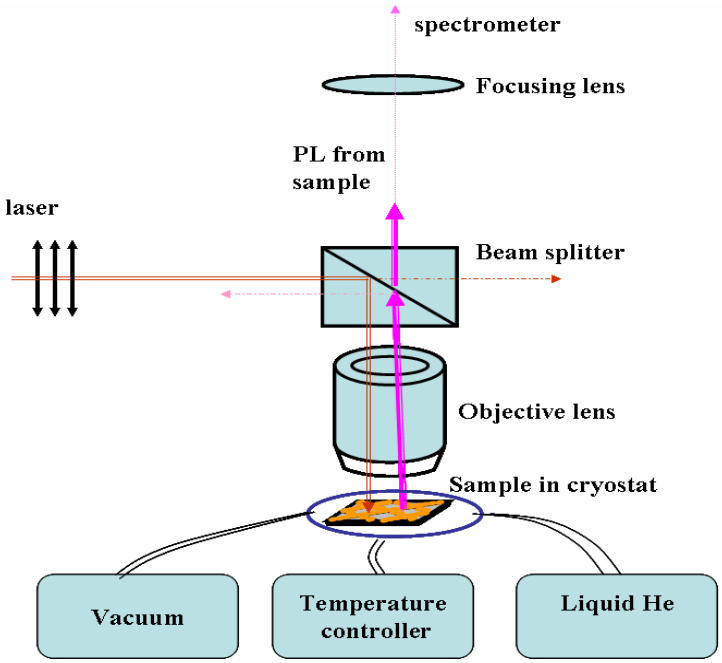

Figure 4.12 Schematic diagram of a setup for the temperature-dependent measurement.

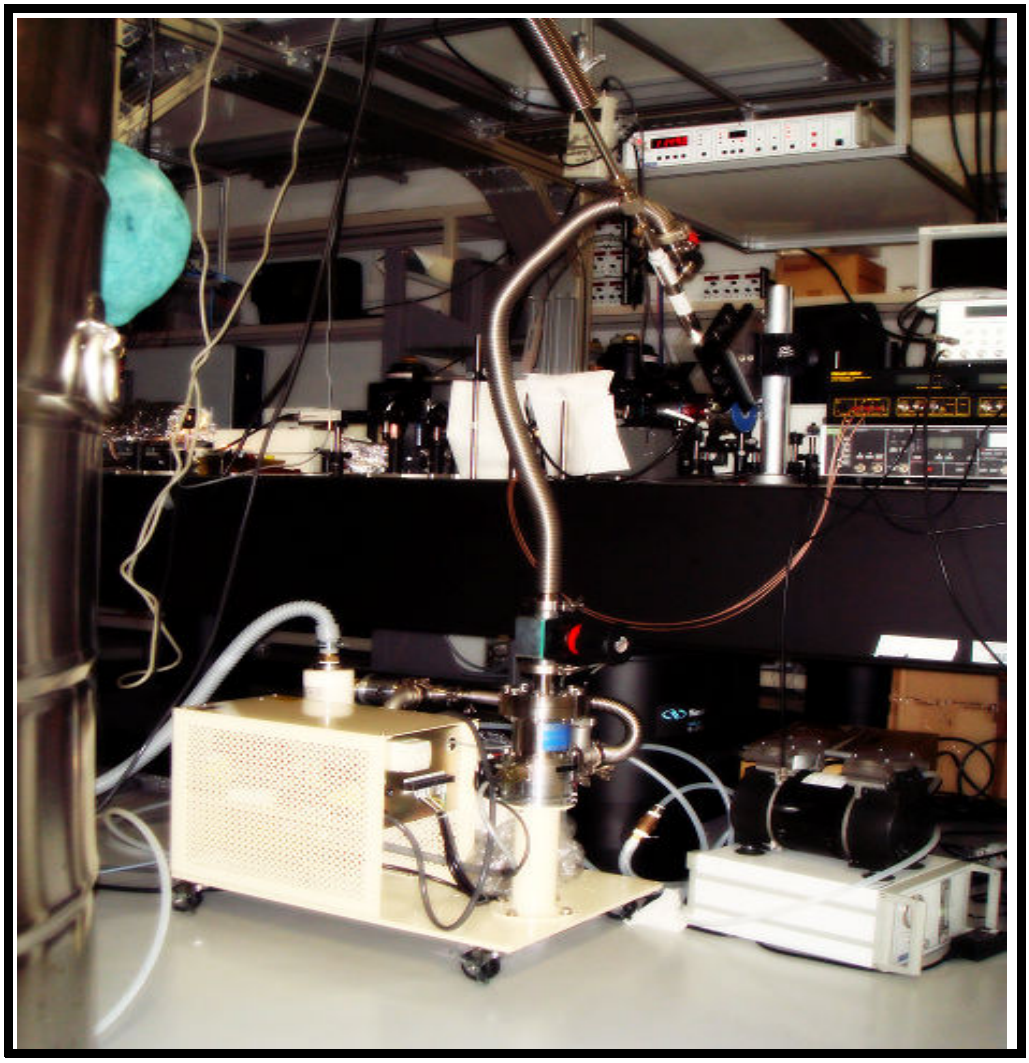

Figure 4.13 Photo of the temperature-dependent PL setup.

The temperature, monitored with a sensor mounted on the cold-finger, was controlled via Oxford 5035 Intelligent Temperature Controller, which was using a programmable integrate/differentiate circuit to supply current to a heater assembly which was also mounted on the cold-finger. This arrangement is depicted in Fig. 4.13. When the temperature was increased from 4 K to a higher temperature, there was some contamination around the optical window of the cryostat caused by the temperature increase. To get rid of this effect, the vacuum system was connected to the cryostat and used to pump out the contamination from the cryostat.

4.5 Polarized-PL Measurements

This measurement was one of the crucial measurements for characterizing the laterally aligned quantum dots. This section discusses some aspects of the components that were added to the previous experimental setup which affect the outcome and repeatability of the experiments. They will be described in relation to different aspects of the experimental layout: the laser light, the optics, the detection, and the sample chamber. Before discussing the experimental layout, some theoretical background for the polarization measurements will be presented.

4.5.1 Malus's law

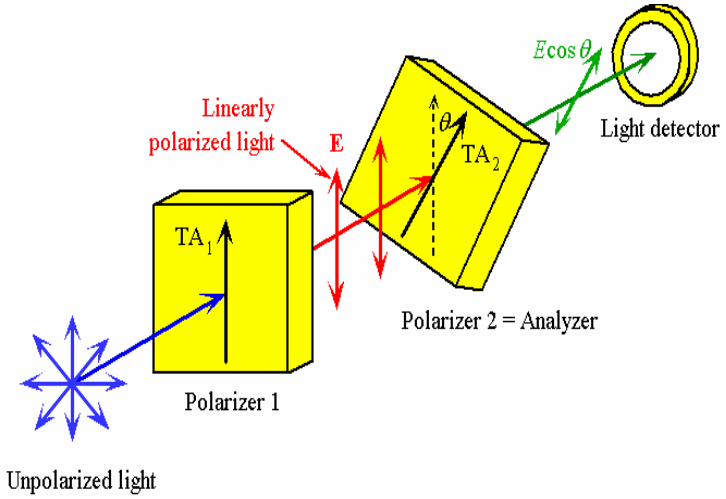

Figure 4.14 Explanation for linear polarization (After Ref. [65])

In Fig 4.14, randomly polarized light is incident on a polarizer 1 with a transmission axis TA1. Linearly polarized light from the polarizer is then incident on the analyzer. By rotating the transmission axis of the second polarizer, the polarization state of the incident beam can be analyzed. If the transmission axis of the second polarizer is at an angle θ to the field of the incident beam, then only the component of the $E \cos \theta$ will be allowed to pass through the polarizer 2. The intensity of light passing through the analyzer is proportional to the square of the electric field [65].

$$I = I_0 \cos^2 \theta \tag{4.4}$$

Therefore, the Malus's law relates the intensity of a linearly polarized light passing through a polarizer to the angle between the transmission axis and the electric field vector. This law was used to analyze the experimental results to confirm degree of linear polarization of the laterally aligned quantum dots investigated in this project.

4.5.2 Polarized-PL Experimental Setup

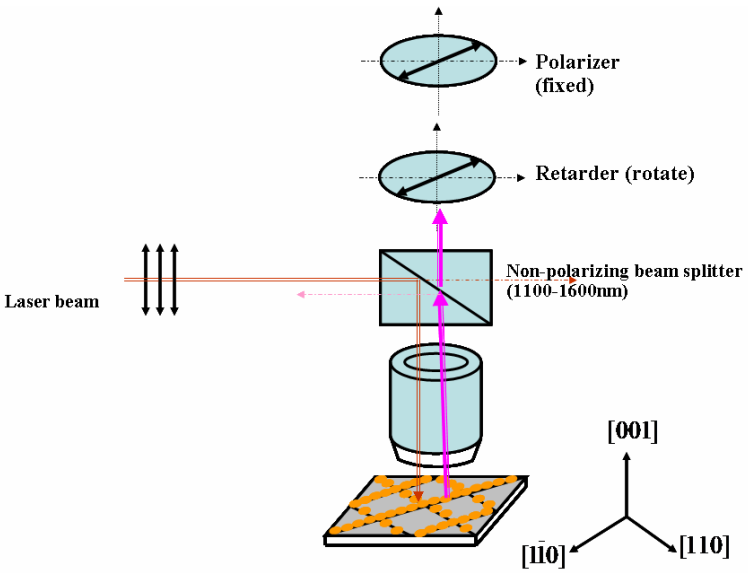

Figure 4.15 Experimental setup for polarization measurements.

The PL spectrum was collected by the objective lens, dispersed by the double-grating monochromater, and detected by an InGaAs detector, the same setup as mentioned before. The polarization characteristic measurement was carried out by fixing a polarizer, serving as the analyzer, which was placed in front of a detector. The output intensity of the detected signal from the photodetector was also displayed by a digital multimeter. To eliminate the artifacts from polarization-dependent efficiency of the monochromator, a half-wave plate was put in front of the monochromator. In the measurement, the transmission axis of the half wave plate was rotated until a maximum reading on the multimeter was obtained, and this was marked as the 0° polarization angle, which was used as the reference angle.

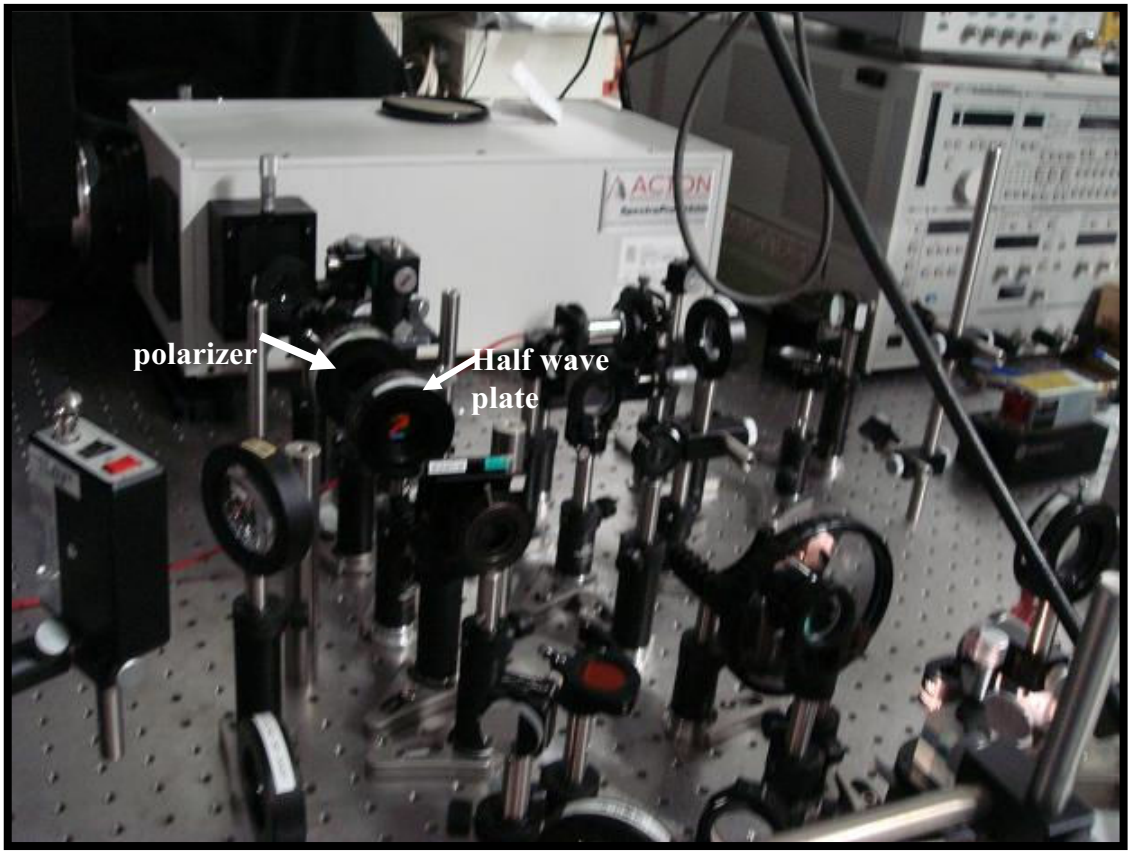

Figure 4.16 Photo of the polarization measurement setup.

In summary, many different factors contribute to the appearance of PL spectra. PL spectra can identify poor crystallinity by emitting weaker intensity. Another interesting behavior in PL spectroscopy is the full-width-at-half-maximum (FWHM) of the PL spectrum. This is because the FWHM may easily become broadened by structural impurities, such as interface roughness, composition, inhomogeneity, and partial strain relaxation, etc. A narrower PL peak can indicate a higher quality sample. However, identified PL behaviors overlap with other causes besides impurities. For instance, broadening, intensity reduction, and energy peak shifting can indicate strain relaxation. On the other hand, growth temperatures and laser excitation power can influence a peak shift to higher energy. The factors are summarized in the following table.

FWHM depends on	Peak energy depends on	Intensity of sample depends on
Temperature	Bandgap energy of material	Excitation laser power
Impurity concentration	Quantum confinement of the structure	Measurement temperature
Dot size homogeneity	Size of the nanostructure	Spectrometer slit width
Exciton binding energy	Measurement temperature	Alignment of the optical setup
Strain relaxation	Strain	
Sample quality		

In conclusion, PL spectroscopy is a useful, nondestructive technique which can be used to determine optical characteristics of the sample under investigation.

CHAPTER V

OPTICAL CHARACTERIZATION OF ALIGNED QUANTUM DOTS

5.1 Self-Assembly Crystal Growth

The quantum dots characterized in this project were produced by the crystal-growth method of molecular-beam epitaxy (MBE). In MBE, one begins with a high-quality substrate, heated and placed in an ultra-high vacuum. Sources of pure elements are heated so that a small flux of atoms evaporates and goes towards the substrate as a beam. These beams are turned on and off using shutters. Some of the atoms that strike the substrate stick to it, and due to the high temperature of the substrate, these atoms move across the surface until they find an energetically favorable resting place, typically along an atomic step. These steps propagate across the sample surface as single monolayers which are deposited onto the substrate. Optimal crystal growth depends on the atomic beam flux ratios, the substrate temperature, and the absence of contaminants.

The self-assembled InAs quantum dots illustrated in Fig. 5.1 was grown by technique known as Stranski-Krastanov growth mode [66]. Here, quantum dots form when InAs is grown on top of GaAs, due to the lattice size mismatch (the natural lattice size of InAs is 7% larger). The first one or two monolayers of InAs match the underlying GaAs lattice, but are under mechanical strain. This initial, smooth layer of InAs is called the "wetting layer." After a critical thickness (typically less than 2 monolayers), it becomes energetically favorable for the InAs layer to form islands. These are typically 4-7 nm thick and 20-40 nm in diameter, depending on the growth parameters. The density of islands depends on both the growth temperature and the amount of indium deposited, which can vary from 10 μm^{-2} to 500 μm^{-2}. By the aid of atomic-force microscope (AFM) images, surface morphology of uncapped InAs islands may be seen. For optical characterization of the quantum dot structures, a GaAs capping layer is grown on top.

The optical properties of quantum dots depend heavily on the growth process. The emission wavelength depends on both the size and the composition (how much GaAs is mixed into the InAs island). The eigen-energy-level spacings for these quantum structures also depend on these same factors. The fine structure splitting

depends on the amount of asymmetry in the shape of the structure and in the associated strain field [67]. The cleanliness of the growth might affect whether quantum dots start out neutral, or with extra charges.

In this chapter the optical characterizations of ordered quantum dots which were grown by using the thin-capping-and-regrowth technique and on virtual substrates are addressed.

5.2 Thin-Capping-and-Regrowth Technique

Recently, ordered InAs QDs grown on GaAs [001] substrate using a thin-capping-and-regrowth technique have been demonstrated [68]. First, the randomly distributed QDs were grown on a flat surface by using conventional growth technique. A thin GaAs layer was then capped on top of the QD layer. Because of the lattice mismatch between the QDs and the capping layer, the strain energy around the QDs is increased and In atoms migrate out from the QDs. As a result, a nano-hole appeared in the middle of each QD. By regrowing the QDs on the top of the nano-holes via the thin-capping process, nano-propeller QDs were formed. By repeating the thin-cap-and-regrowth method for three cycles, QDs thus formed aligned along in one direction, specifically the $[1\bar{1}0]$ direction. The following section discusses the optical characterizations of such aligned quantum dots, but the optical characterizations of as-grown QDs and of very-high-density QDs will be presented first, serving as the reference.

5.2.1 (a) As-grown QDs (Reference Sample)

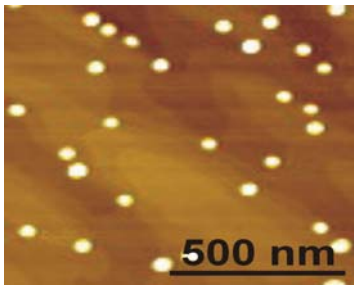

Figure 5.1 AFM image of as-grown InAs QDs grown on semi-insulating [001] GaAs substrate. (Suraprapapich *et al*., 2005)

According to AFM images, the as-grown InAs QDs are randomly distributed on the sample surface. The size of QDs appearing on the AFM images, is almost circular. For the optical characterization, two PL peaks were observed, as shown in Fig.5.2, and no polarization property was observed.

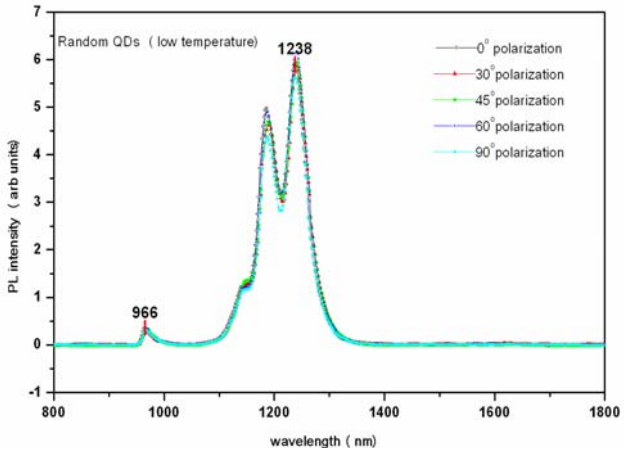

Figure 5.2 Polarization-resolved PL spectra of as-grown InAs QDs measured at 77 K.

5.2.1 (b) High-density QDs (Reference Sample)

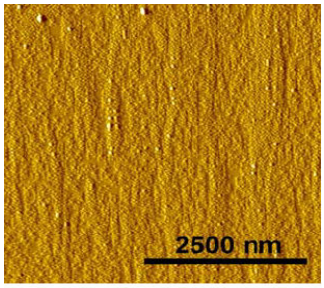

Figure 5.3 AFM image of high-density InAs QDs on semi-insulating [001] GaAs substrate grown by using the thin-capping-and-regrowth technique for 10 cycles. (Suraprapapich *et al.,* 2005)

According to AFM images, the InAs QDs are densely distributed on the sample surface. The actual size of the QDs is difficult to evaluate from the AFM images. The dot size uniformity is worse than the previous sample because of the high dot density. As expected, in optical characterization, a broad spectrum with no polarization characteristic was observed for this sample. Very small emission intensity difference

between parallel and perpendicular directions may come from the error of optics, which is about 0 - 4 %.

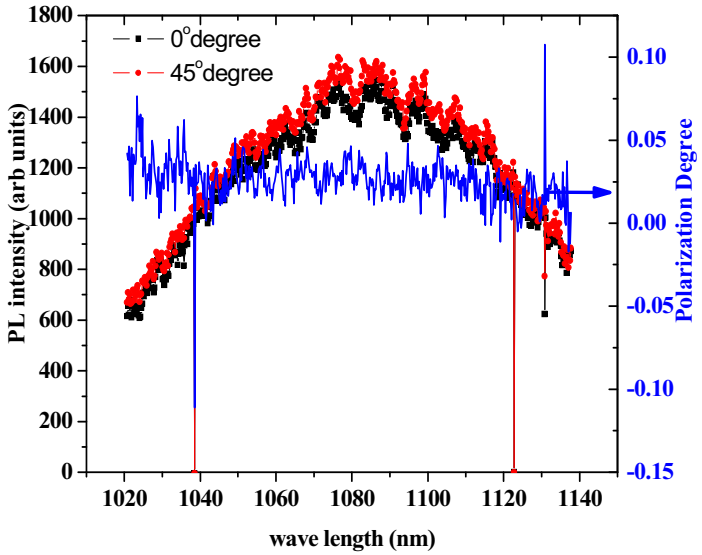

Figure 5.4 PL spectra of high-density InAs QDs measured at a low temperature (4 K) with the excitation power of 500 μW.

Table. 5.1: Summary of the optical characterization of as-grown QDs and high-density QDs.

	Peak (eV)		**FWHM (meV)**	
Temperature	RT	77 K	RT	77 K
As-grown QDs	0.992	1.01	29	28
High-density QDs	1.13	1.148	100	96

5.2.2 Binary Quantum Dots

When two semiconductor QDs are close to each other, carriers in the QDs begin to interact with one another. In particular, the wavefunctions of the carriers in the binary-QD system may overlap. Coupled quantum dots have been interested because of coupling and entanglement of quantized energy states between neighboring QDs. They possess a potential application for quantum information devices [69]. The formation of laterally coupled binary quantum dots may be achieved on the [001] GaAs substrate by gas-source MBE (GSMBE). First, a 300-nm GaAs buffer layer was deposited at 580°C, followed by a 1.8 ML of InAs QDs after reducing a substrate temperature to 500°C. Then the substrate temperature was reduced to 470°C and a 6 ML of thin GaAs capping layer was-grown on the randomly distributed QD layer. A similar routine leads to the modification of nano-templates for formation of quantum rings (QRs). At a regrowth thickness of 0.6 ML, binary quantum-dot molecules (Bi-QDMs) are formed at the rims of QRs on which preferable sites for quantum dots in the molecules to form are aligned along in $[1\bar{1}0]$ direction [70].

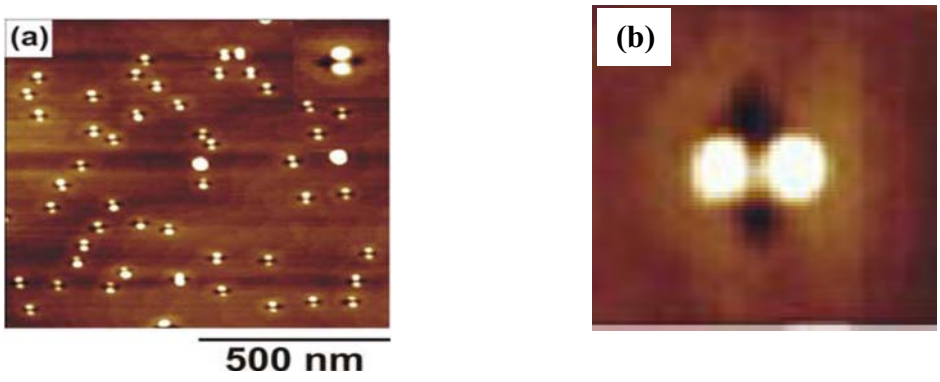

Figure 5.5 (a) AFM image of binary QDs, and (b) close-up image of binary QDs. (Suraprapapich *et al*., 2006)

According to AFM information, the two quantum dots are close together and the center-to-center distance between two QDs is 22 nm, the size of individual QDs on Bi-QDs is 20 nm, so that this system can be regarded as coupled quantum dots. The coupling effect in bi-QDs is expected to affect the optical properties of the structure. With the aid of photoluminescence spectroscopy, information about electronic levels

of these structures was subsequently investigated. Additional information from the polarization measurement results supports to learn the physics of this kind of nanostructure. In this section the average information of the sample and individual quantum dots are investigated using micro-photoluminescence. The coupling behavior of InAs bi-QDs are presented by means of temperature-dependent PL, excitation-power-dependent PL, and polarized PL measurements. Conventional PL measurements and polarized PL measurements were also performed for individual quantum dots in the bi-QD system.

5.2.2.1 Excitation-Power-Dependent PL Measurements

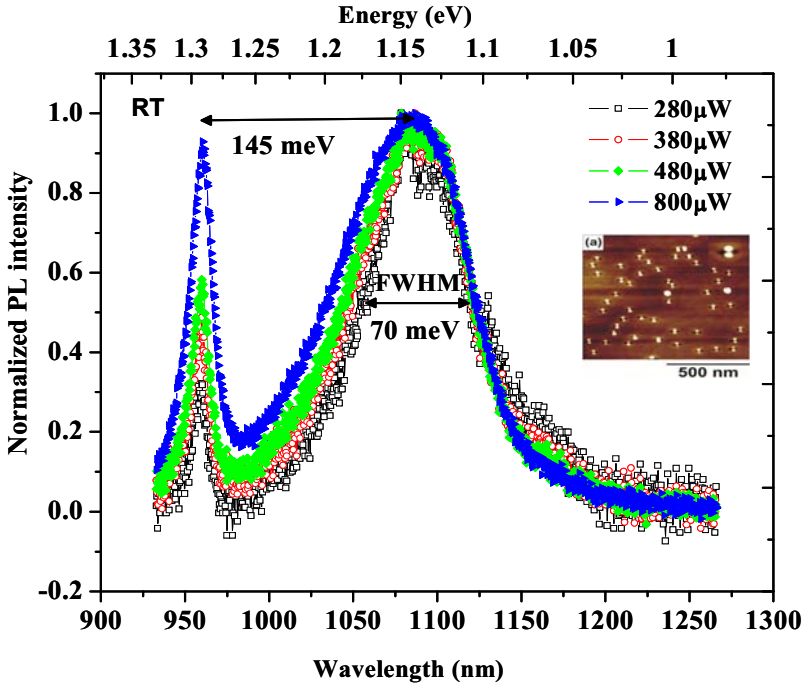

Figure 5.6 Excitation-power-dependent PL spectra of bi-QDs at room temperature.

Figure 5.6 shows various PL spectra at room temperature by using the laser excitation power ranging from 280 μW to 800 μW. The PL peak at 1100 nm (1.15 eV) was observed and the second peak around 953 nm (1.3 eV) distinctly occurred. The energy difference between the first peak and the second peak of about 145 meV is so large that it can not be considered as the excited state of QDs compared with typically 50-60 meV energy difference between the ground state and the excited state for isolated InAs quantum dots [71]. The second peak at 1.3 eV is attributed to the wetting layer of InAs quantum dots. A full-width-at-half-maximum (FWHM) of

around 70 meV is due to the size fluctuation and the thermal relaxation of carriers of QDs at a high temperature [72]. Strong PL intensity obtained for room-temperature measurement indicates that this structure can be utilized in light emitting device for room-temperature application.

To understand the physics of the bi-QD structure, low-temperature PL measurements were also carried out. At 10 K, the sample was excited by using different excitation powers as shown in Fig. 5.7. The PL spectrum can be fitted into two-Gaussian curves. To extract the two peaks out of the spectrum, the AFM images were then carefully investigated. The AFM images informed that the size of the bi-QDs is smaller than the single, isolated dots on the sample. Population of the smaller QDs (in bi-QDs) is 70% and that of merged QDs (larger size) is 30 % on this sample. The carrier confinement is better in smaller QDs and the luminescence intensity may be high. Thus, the peak at the higher energy side came from bi-QDs and the lower energy peak originated from merged singled QDs. The distance between the two peaks is around 60 meV. Further increasing the excitation powers lead to broader linewidths in the higher energy side, which is similar to the behavior observed from room-temperature measurement and is probably caused by the state filling effect [73]. Another consideration is that for uncorrelated QDs, state filling effect occurs at the first excited state of the QDs. Some literature reported experimentally that correlated quantum dots can give a broadened linewidth at the higher energy side. This kind of behavior is also observed in another coupled QDs sample [74].

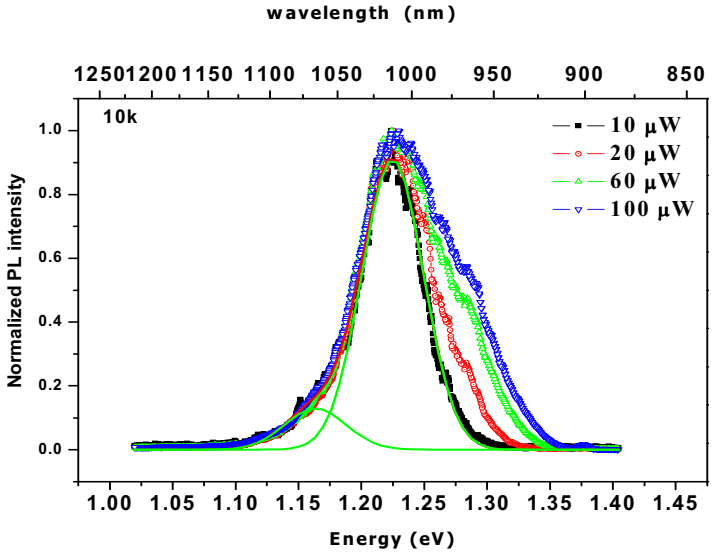

Figure 5.7 Excitation-power-dependent PL spectra at 10 K**.** The spectrum can be convoluted into two Gaussian peaks.

5.2.2.2 Temperature-Dependent PL Measurements

Figure 5.8 shows a temperature-dependent PL spectrum and Figure 5.9 shows the integrated PL intensity of bi-QDs. It is seen that: First, the PL spectral shape and the peak position are dependent on temperature. Second, the integrated PL intensity increases with the increasing temperature up to a certain temperature and then decreases with further increasing the temperature. In general, the PL intensity decreases with increasing temperature due to an enhancement of the non-radiative recombination process and a reduction of the excitonic transition with temperature [75]. One possible reason for an increase in the integrated PL intensity as well as a change of the peak position and the spectral linewidth is connected with the carrier dynamics [76]. In case of a coupled bi-QD system, the wavefunctions of the carriers in the adjacent QDs overlap with each other. This overlapping of wavefunctions is expected to relieve the phonon relaxation bottle neck by increasing the number of states related to carriers and so the integrated PL intensity increases with the increasing relaxation [77]. When the temperature goes up, the coupling and relaxation effect will increase because of the increasing electron-phonon interaction.

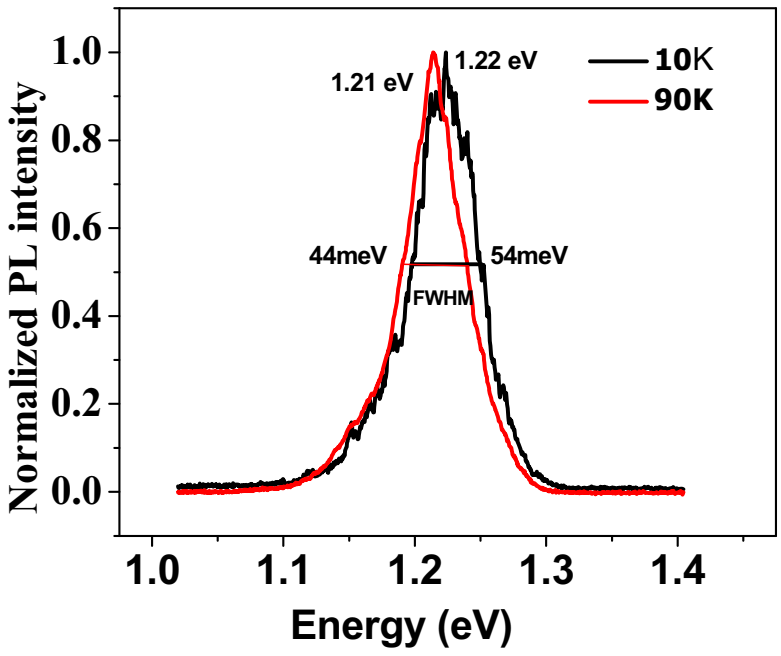

Figure 5.8 Temperature-dependent PL spectra of bi-QDs measured at 10 K and 90 K. The peak shift by 10 meV was clearly observed at 90 K.

As a result, the photogenerated carriers transfer and relax into the energetically lower energy state, and recombine there. Consequently, the PL peak is shifted to a lower energy level. Increasing photogenerated carriers in the lower energy level at higher temperature causes a higher PL intensity [78-79]. This process is also expected to cause a reduction in the FWHM of the PL spectrum. At 90 K, the integrated PL intensity is highest and the linewidth decreases to 44 meV compared with the 54 meV at 10 K. Further increasing the temperature, the linewidth increases again and the integrated PL intensity reduces. This is due to the electron-phonon scattering and thermal distribution [80].

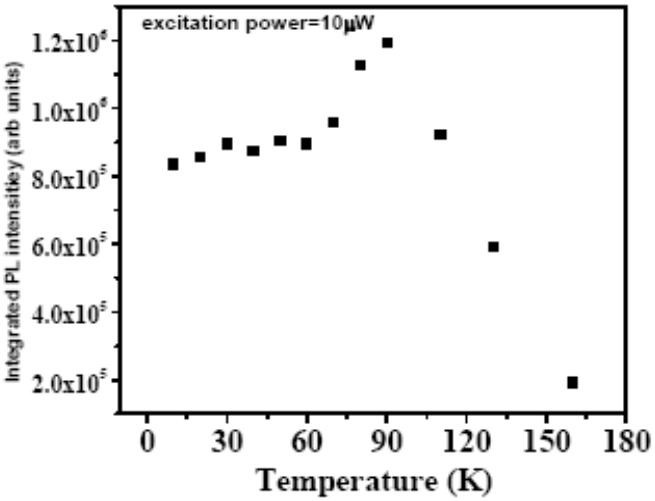

Figure 5.9 Temperature-dependent integrated PL intensity of bi-QDs. The temperature ranges from 4 K to 180 K, and the laser excitation power was held at 10 μW.

5.2.2.3 Polarization-Resolved PL Measurements

The polarization measurements were carried out to learn the detailed physics of the bi-QDs. At room-temperature measurement, the distinct linear polarization was not observed. At 10 K, the linear polarization degree was 7% and almost no polarization dependence was found for the PL emission from the GaAs substrate, however. The anisotropy was nearly constant over the whole energy spectrum indicating a homogenous uniform shape, orientation and strain distribution [81]. Further increasing the temperature, the polarization degree also increases, and at 50 K the polarization degree increases to a maximum value of 13%. Fig. 5.10 shows the

temperature-dependent polarization spectrum of bi-QDs, and Fig. 5.11 shows the polarization degree of bi-QDs change with the temperature. All polarization measurements were measured under non-resonant excitation in the barrier of GaAs and the detection time to measure the spectrum was 1 second.

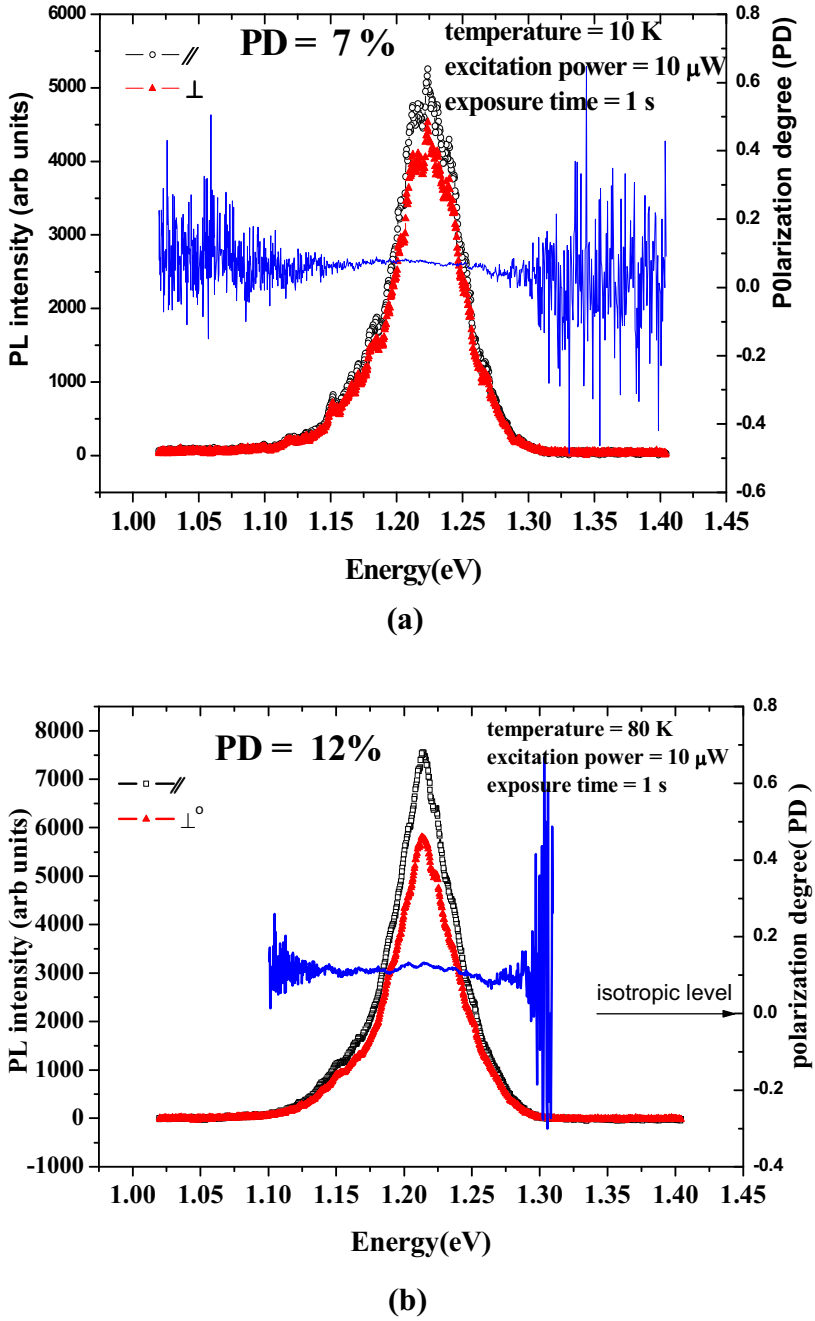

Figure 5.10 Temperature-dependent polarized PL spectra of binary QDs at (a) 10 K and (b) 80 K. When the temperature was increased, the shape of the spectrum changed and the polarization degree increased.

The temperature-dependent PL measurements show that the degree of linear polarization (PD) changes with the temperature. When temperature increases, the PD increases at first and attains the highest degree around 50 K. Between 50 K and 90 K, the polarization degree is almost constant, and above 90 K the polarization degree starts to decrease sharply. Therefore, the polarization degree in this binary QD is probably related to the carrier dynamics in the QDs [82]. This kind of polarization behavior is probably caused by the thermal dislocation of carriers from 0-D quantum dots state to the 2-D quantum well state with the increasing temperature. At low temperatures, the excitons are localized in the QDs. When the temperature was increased to a certain point, the localized carriers obtain enough energy to travel through the two coupled QDs. The coupling strength of the QDs becomes stronger and the QDs lost 0-D features and act like a 1-D quantum wire with an associated increase in polarization anisotropy [83]. When the temperature is high enough, optical polarization anisotropy is reduced. The mechanism of reducing PD is still unclear and need the some more experiments to decide the mechanism.

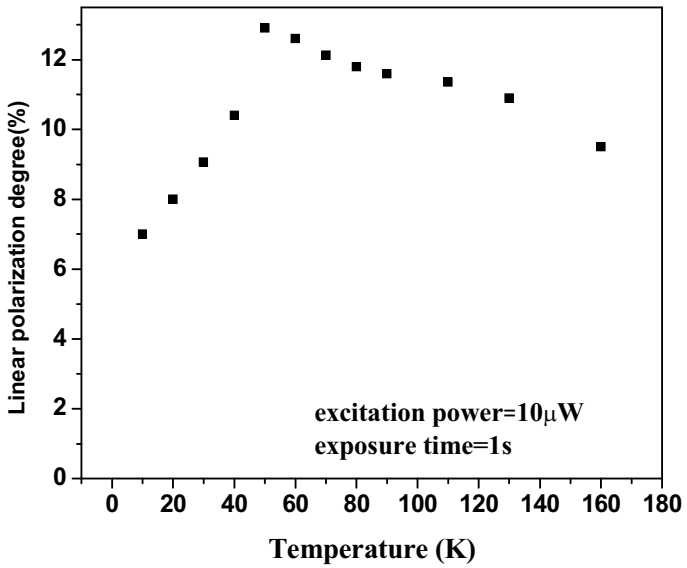

Figure 5.11 Temperature-dependent polarization degree of binary QDs; the temperature ranges from 4 K to 180 K, and the excitation power was held at 10 μW.

5.2.2.4 Single-Dot Spectroscopy

Optical spectroscopy studies of particular dot structures were performed to know the exact information of single QDs. The sample was held at 3.8 K in a continuous-flow cryostat. Individual PL spectra of single QD from the bi-QDs obtained under very low excitation power density while increasing the detection time into 90 s are shown in Fig. 5.12. At the lowest pump intensity, three emission peaks were observed at 1.133 eV, 1.135 eV and 1.136 eV, labeled as X1, X2 and X3, respectively. Usually, for a single dot, at low excitation power, only the exciton decay from the s-shell (shell with an orbital angular momentum L = 0) is observed. At high excitation powers, two or more excitons were present in any one dot. The origins of the peaks from the individual quantum dots were identified by measuring the power dependence of the spectra [84-86]. When the excitation power was increased, the spectral line X1, X2 and X3 increased with almost same intensity ratio. Another peak at around 1.134 eV appeared and was marked as XX.

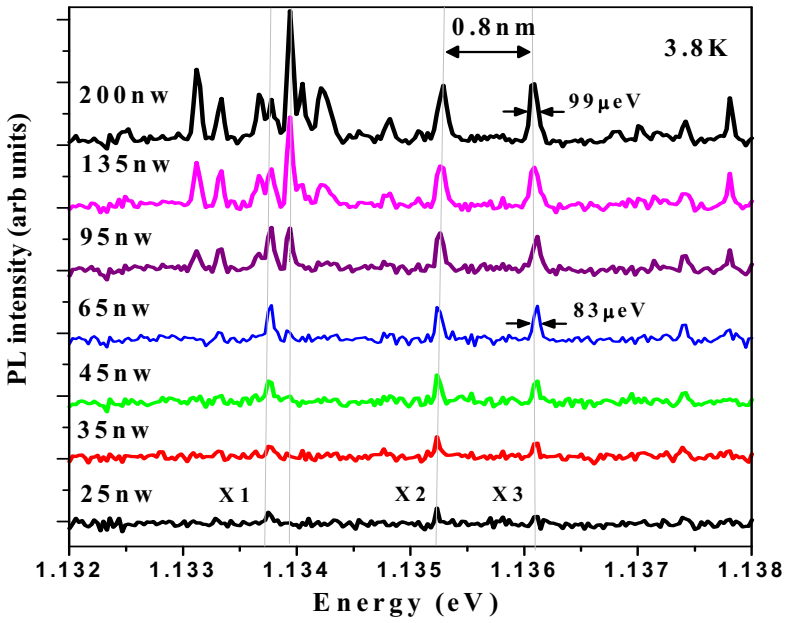

Figure 5.12 Excitation-power-dependent single-dot spectroscopy of the bi-QD system; the excitation power ranges from 25 nW to 200 nW, and the temperature was held at 3.8 K. At 25 nW, three distinct peaks were observed, and when the excitation power was increased, many peaks appeared.

The PL intensity as a function of excitation power is shown in Fig. 5.13. While the fundamental peak X1, X2 and X3 increases linearly with increasing excitation power, the additional peak XX shows a quadratic power dependence. This suggests the assignment of peaks X and XX to the excitonic ground state and the bi-exciton, respectively [87-88]. As shown in Fig. 5.13, the linewidth of a single InAs QD is around 1 meV and this value is very similar to another report [89]. The sample was measured at several points at a low excitation power, and about 20 spectra were observed. The narrowest observed spectral linewidth is about 60 μeV (FWHM). State filling effect easily occurs when the excitation power is increased, since only the small number of excitons can be accommodated in the small dot structure, resulting in broader PL spectra obtained at higher excitation powers [90]. Broadening caused by phonons is expected to be negligible in that case, since the population of phonons is very low at 3.8 K [91].

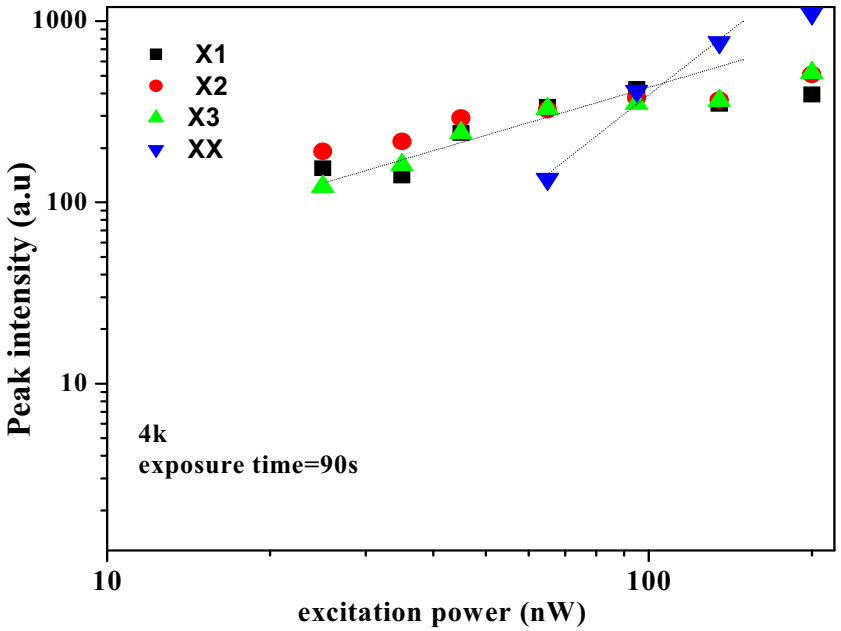

Figure 5.13 Excitation-power-dependent single-dot spectroscopy of exciton state and bi-exciton state from single-dot spectroscopy measured at 4 K. The exposure time to measure the optical signal the sample was 90 s.

The polarization-resolved PL measurements were made with a linear polarizer and a λ/2-waveplate inserted between the microscope and the spectrometer. The polarizer was rotated to maximize the grating efficiency of the spectrometer. The waveplate was then rotated in steps of 10° each. The two peaks are thus polarized in orthogonal directions. The energy split between 27 μeV and linear polarization is around 16%, as seen in Fig. 5.14. Theoretical results and some experimental results showed that the fine structure splitting and the linear polarization characteristic come from the elongation of the individual QDs(in the bi-QDMs) [92-94].

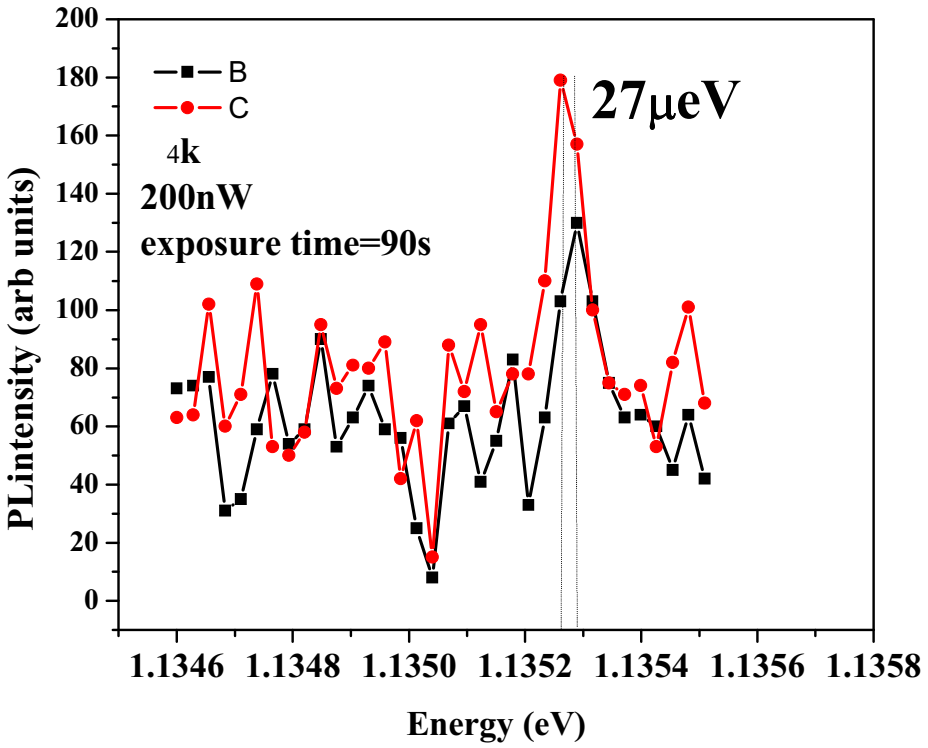

Figure 5.14 Polarization spectroscopy of single QDs in bi-QDMs. Fine structure splitting and the polarization characteristic were observed at 1.1352 eV.

5.2.3 Linearly Aligned Quantum Dots

5.2.3.1 Sample 0434 (Sample A)

This sample was used for our first optical characterization of linearly aligned quantum dots [95] . This sample has quantum dots aligned along the $[1\bar{1}0]$ direction (the alignment on average is about 500 nm long). The dots were grown by molecular-beam epitaxy on a [001] GaAs semi-insulating substrate using the thin-capping-and-regrowth process. After growing InAs QDs at 500°C, the substrate temperature was ramped down to 470°C and partially-capped with GaAs for 6 ML and then regrown with InAs QDs for 0.6 ML at the same temperature. After repeating the thin-capping-and-regrowth process for 3 cycles, 500 nm long aligned quantum dots were obtained on the nano-template as shown in Fig 5.15. For optical characterization, 100-nm capping was grown on the top of the sample.

In order to confirm the structure of the QDs, the surface morphology of the QD sample was observed under an atomic-force microscope (AFM). An AFM image of the nano-template is shown in Fig. 5.15, and that of linearly aligned quantum dots is shown in Fig. 5.16. The average size of the quantum dot is 60-80 nm and the height is about 3-4 nm.

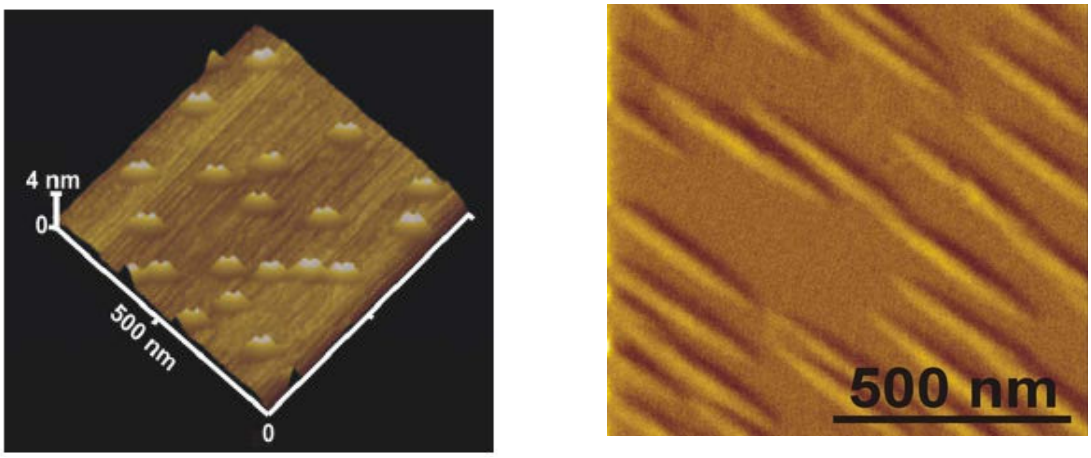

(a) (b)

Figure 5.15 AFM images of (a) a camel-like structure created as a result of thin-capping and regrowing over as-grown QDs, (b) nano-template for aligned quantum dots with an average length of 0.5 μm. (Suraprapapich *et al*., 2005)

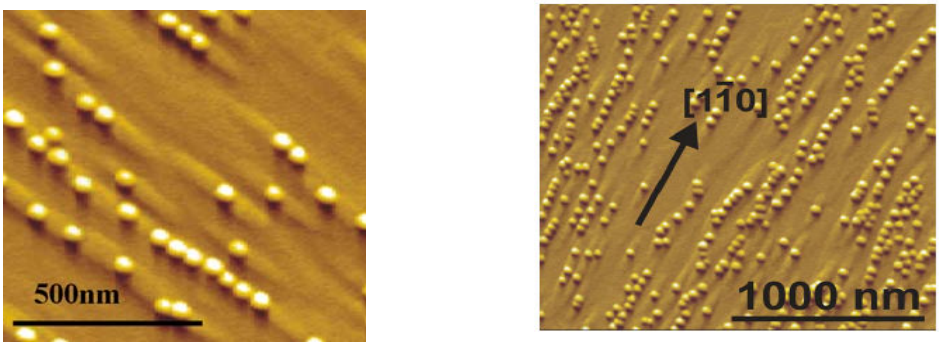

(a) (b)

Figure 5.16 AFM images of Sample A: (a) 500×500 nm^2, (b) 1×1 μm^2. (Suraprapapich et *al*., 2005)

According to the AFM images, it was found that all QDs aligned along the [1$\bar{1}$0] crystallographic direction, but the alignment of the chained QDs was not perfect. Some parts of the chained QDs were closely packed together. The lateral spacing between one dot and another depends on the position of the sample.

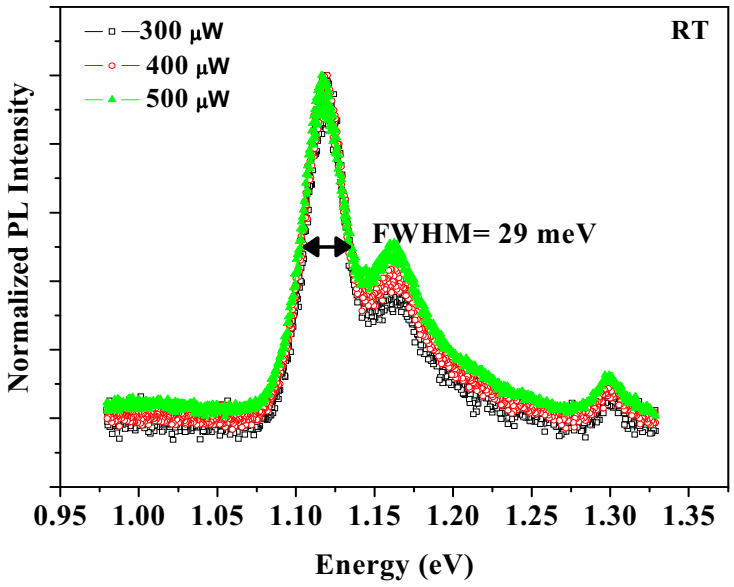

Figure 5.17 Room-temperature PL spectra of Sample A: Two peaks appeared and the third peak at 1.3 eV came from the wetting layer.

Figure 5.17 shows the room-temperature PL measurement. Two distinct emission features can be observed from the PL spectrum. The peak position difference between the main peak and shoulder peak in the figure is about 45 meV.

There are three possibilities to decide upon the origin of the lower peak at the higher energy side. It may come from the quantum dots with different sizes or the excited state of the quantum dots. Since the lower peak occurs in the higher energy level region, it may also come from the wetting layer. According to the AFM image, the size of the QD is almost uniform. To confirm the origin of the lower peak, the excitation-power-dependent photoluminescence was observed, as shown in Fig. 5.17. When the excitation power was increased, the peak height ratio between the lower peak and the main peak increased as well. If the lower peak came from the dots with different sizes, the peak intensity ratio would have been constant regardless of the excitation power [96]. Accordingly, the assumption that the lower peak corresponds to the transition between the second quantum levels can also account for the behavior of the excitation-power-dependent-PL intensity ratio change. From this result, it may be concluded that the lower peak comes from the first excited state of the quantum dots, and the smaller peak at 1.30 eV comes from the wetting layer of quantum dots.

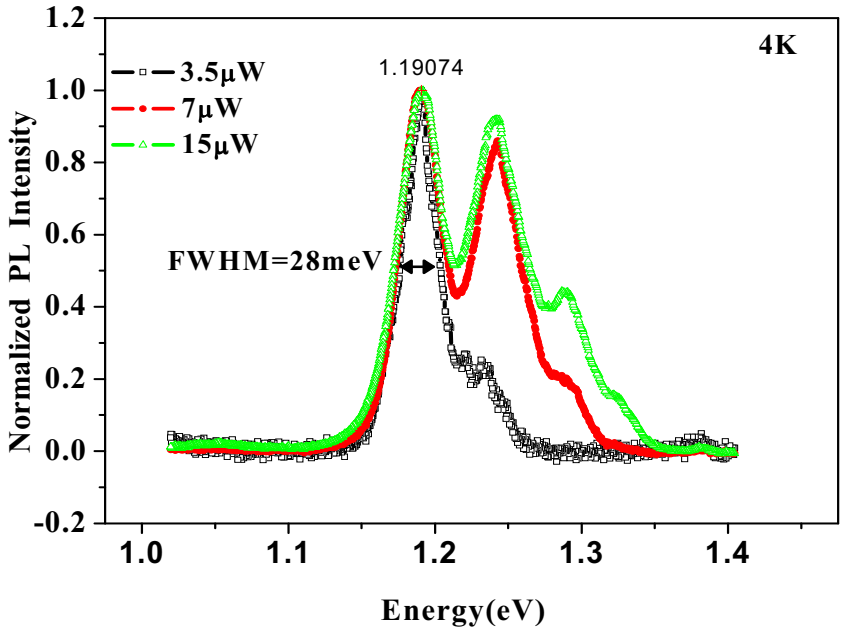

Figure 5.18 Low-temperature PL spectra of Sample A (4 K).

Figure 5.18 shows the low-temperature (4 K) PL measurement. The peak is shifted to the higher energy side with respect to the room-temperature PL spectra. The full width at half maximum at low-temperature measurement of 28 meV is not different from the room-temperature measurement. The quality of sample was good, and the linewidth broadening did not come from the defect or other effects, like the thermal effect, but comes from the intrinsic property of the dot-size inhomogeneity.

5.2.3.2 Sample 070081(Sample C)

On this sample, the length of alignment of quantum dots is about 1 μm. The dots were grown by molecular-beam epitaxy on a [001] GaAs substrate using the thin-capping-and-regrowth process, similar to Sample A, but the capping thickness was modified in the second cycle. After growing InAs QDs at 500 °C, the substrate temperature was ramped down to 470 °C and partially capped with GaAs for 6 ML and regrown with InAs QDs for 0.6 ML at the same temperature. After that 35 ML of GaAs capping was deposited on the QDs, and 0.6 ML of QDs was grown on it. Then, 6ML of GaAs was capped on top, and as a final step, 0.6 ML of QDs was finally grown on it.

In order to confirm the structure of the QDs, the surface morphology of the QD sample was observed under an AFM. From the AFM image of the Sample C, shown in Fig. 5.19(a), it was found that these QDs align in the [1$\bar{1}$0] crystallographic direction. The average size of the quantum dots is 60-80 nm and the height is about 3-4 nm.

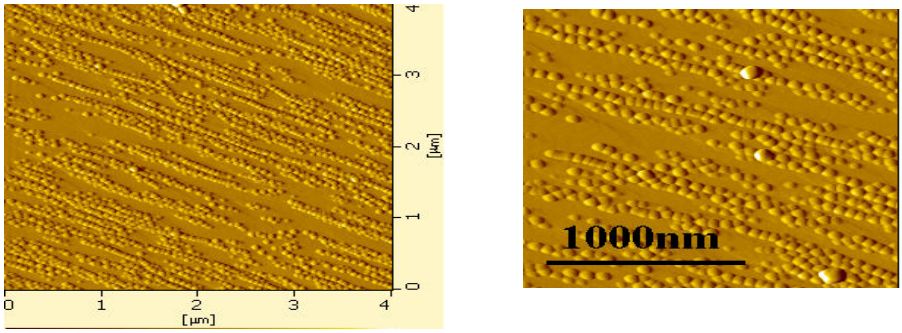

(a) (b)

Figure 5.19 AFM images of Sample C: (a) 4×4 μm^2, (b) 1×1 μm^2. The average alignment length is 1 μm. (Suraprapapich *et al*., 2007)

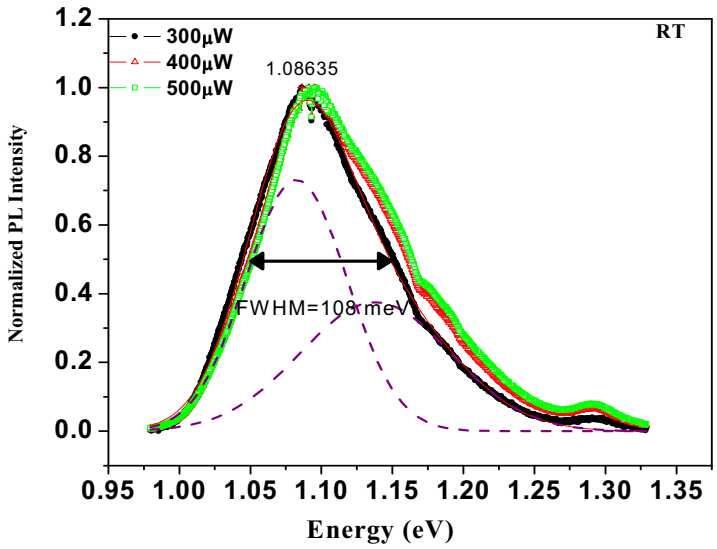

Figure 5.20 Room-temperature PL spectra of Sample C.

Figure 5.20 shows the room-temperature PL measurement. Broad PL emission features were observed with a peak at 1.08 eV in the PL spectrum. The full width at half maximum was about 108 meV.

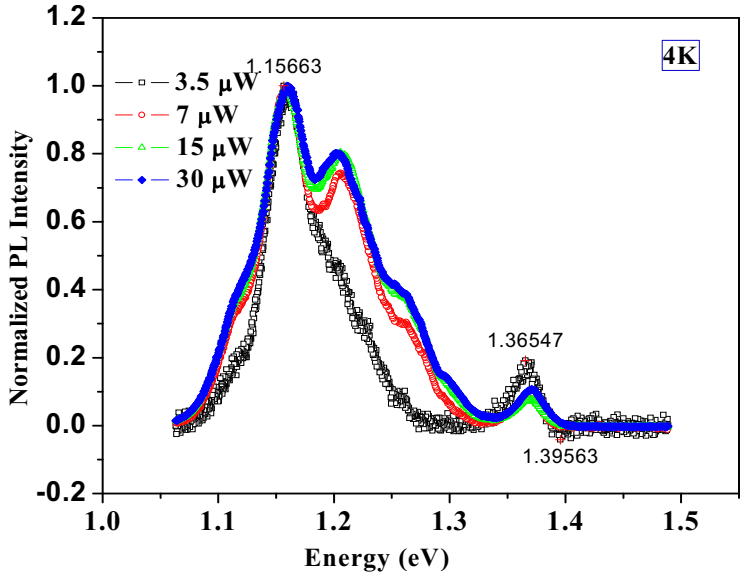

Figure 5.21 Low-temperature micro-PL spectra of Sample C.

For a low-temperature measurement, the shape of the spectrum is different from that obtained at the room-temperature. The full width half maximum was reduced to 58 meV, compared with 108 meV at room temperature. Larger linewidths at room-temperature may be attributed to some defects in the sample.

5.2.3.3 Sample 070080 (Sample B)

The length of alignment of quantum dots on this sample is around 1μm. The dots were grown by molecular-beam epitaxy on a [001] GaAs substrate using the thin-capping-and-regrowth process similar to the two previous samples. After growing InAs QDs at 500°C, the substrate temperature was ramped down to 470°C and partially-capped with GaAs for 6 ML and regrown with InAs QDs for 0.6 ML at the same temperature. After that 6 ML of GaAs capping was deposited on the QDs at 500°C and then 0.6 ML of QDs was grown on it at 470 °C. The thin-capping-and-regrowth process was repeated for only two cycles and the capping temperature modification was done in first cycle.

Like the previous samples, the alignments of the dots are directed along the $[1\bar{1}0]$ direction. The average size of the quantum dots is around 60-80 nm and the height is about 3-4 nm.

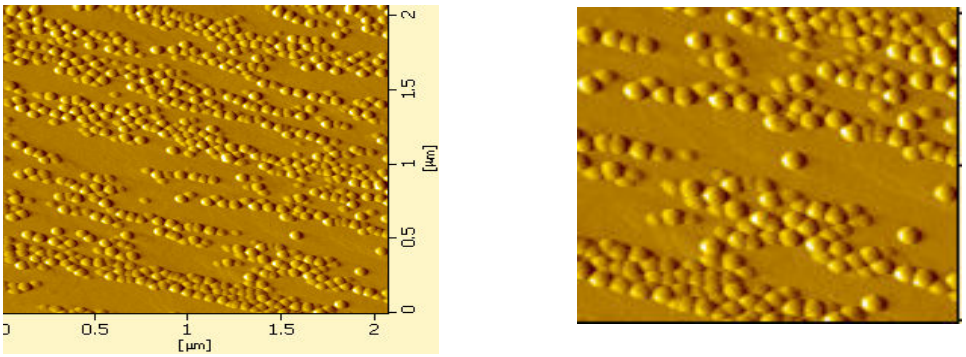

Figure 5.22 AFM images of Sample B: (a) 2 × 2 μm^2 (b) 1 × 1 μm^2 for aligned quantum dots. The average length is 1 μm. (Suraprapapich *et al*., 2007)

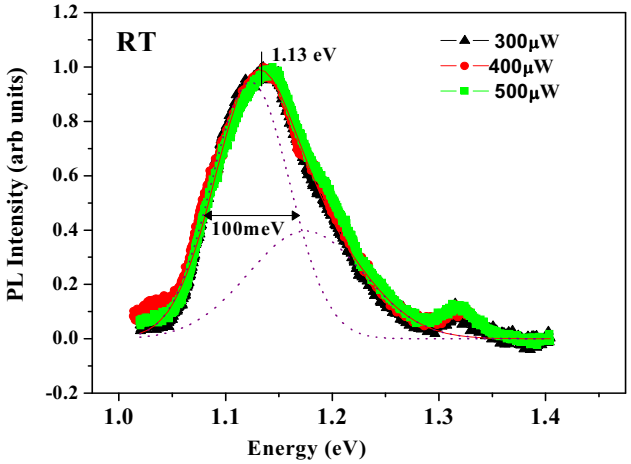

Figure 5.23 Room-temperature micro-PL spectra of Sample B.

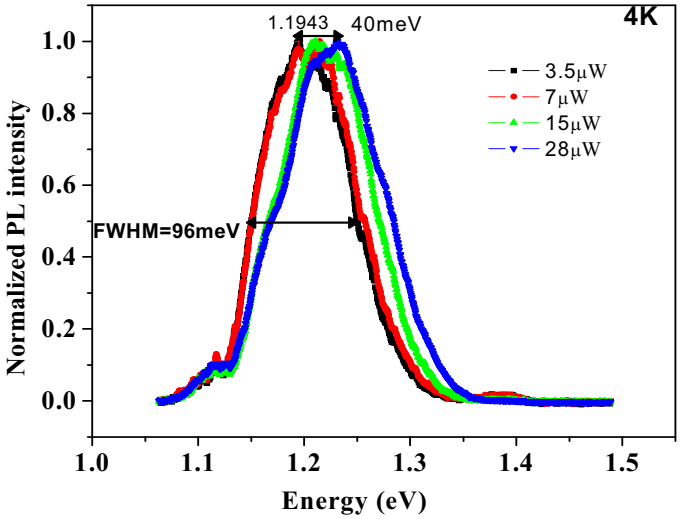

Figure 5.24 Low-temperature micro-PL spectra of Sample B (4K).

Figure 5.23 shows the room-temperature PL measurement. Broad PL emission features were observed with a peak at 1.13 eV in the PL spectrum. The full width at half maximum was about 100 meV. For a low-temperature measurement as shown in Fig. 5.24, the shapes of the spectra are not different from that obtained at the room-temperature. The full width half maximum was reduced to 96 meV compared with 100 meV at room temperature. Lager linewidths at room temperature may not be attributed to some defects in the sample but may come from the size inhomogeneity of QDs. Clear blue shifts were observed both for at room- and low-temperature measurements when the excitation power was increased.

5.2.3.4 Comparison of Three Laterally Aligned QD Structures and the Effects of Growth Parameters on Their Optical Properties

Table 5.2: Summary of growth parameters for three laterally aligned QD samples.

Structure	**Sample A**		**Sample B**		**Sample C**	
	Thick:	**Temp:**	**Thick:**	**Temp:**	**Thick:**	**Temp:**
GaAs (001) substrate	-	-	-	-	-	-
GaAs buffer layer	400 nm	580 °C	400 nm	580 °C	400 nm	580 °C
InAs as-grown QDs	1.8 ML	500 °C	1.8 ML	500 °C	1.8 ML	500 °C
First-cycle GaAs thin capping	6 ML	470 °C	6 ML	470 °C	6 ML	470 °C
Regrown InAs QDs	0.6 ML	500 °C	0.6 ML	470 °C	0.6 ML	500 °C
Second-cycle GaAs thin capping	6 ML	470 °C	6 ML	470 °C	35 ML	500 °C
Regrown InAs QDs	0.6 ML	500 °C	0.6 ML	500 °C	0.6 ML	500 °C
Third-cycle GaAs thin capping	6 ML	470 °C			6 ML	580 °C
Regrown InAs QDs	0.6 ML	500 °C			0.6 ML	500 °C

Table 5.3: Summary of PL of three laterally aligned QD Samples measured at room and low temperatures.

Parameters	Peak Energy (eV)		FWHM (meV)	
Temperatures	RT	4 K	RT	4 K
Sample A	1.12	1.19	29	28
Sample B	1.13	1.19	100	96
Sample C	1.08	1.16	90	58

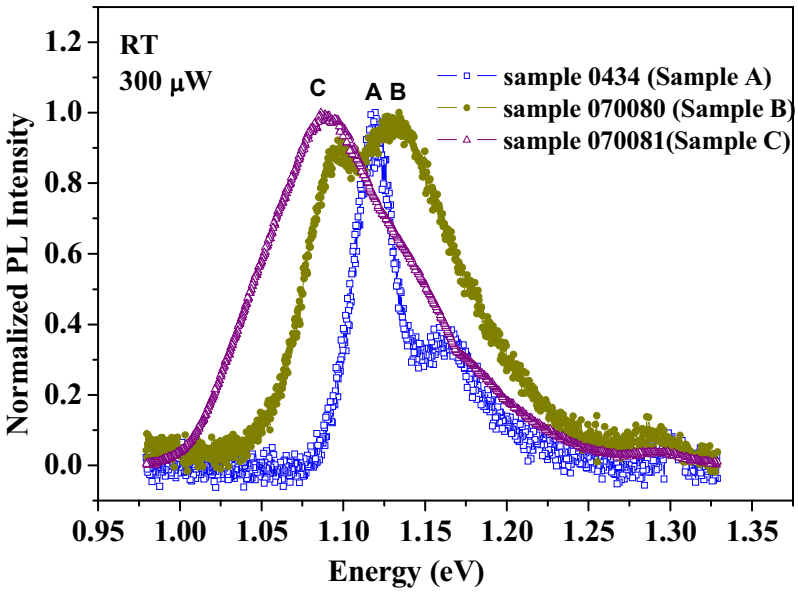

Figure 5.25 Comparison between room-temperature micro-PL spectra of Sample A, Sample B, and Sample C. The excitation power was held at 300 μW.

Room-temperature PL emissions from the three samples were observed around 1.1 eV and intense PL emissions imply improved confinement of InAs exciton and low defect density. These structures have good optical quality and can be utilized as a light emitting source at room temperature. PL emission from wetting layer was also observed around 1.3 eV in the three samples. All spectra are normalized to their maximum intensity value. Among these samples, the dot size homogeneity is the best in Sample A as seen from the narrowest linewidth out of the three samples of 29 meV (full width at half maximum). Also the emission intensity of Sample A was four times higher than that of the other two samples. Some modification of the growth process results in the dot size fluctuation for Samples B and C. Broader linewidth of 120 eV for Sample B and 110 meV for Sample C were observed. The PL spectra were broader in the higher energy side when the excitation power was increased. Each spectrum may be deconvoluted into two Gaussian peaks and the linewidth of the first peak is around 100 meV for Sample B and 90 meV for Sample C. The broader linewidth for higher excitation power indicates that state filling effect involves in this mechanism [96]. The distinct peak shift to the lower energy side occurs for the sample C; this is probably caused by the size of the QDs on this sample being larger than those on the other two samples due to some modification of the thin-capping-and-

regrowth process. Those changes may cause the chain of the QDs longer as well as more dot size inhomogeneity. Evidence for the dot size inhomogeneity and longer alignments were observed from the AFM images of Sample B and C.

For comparing the power-dependent PL of the three samples at low temperature (4 K), the samples were excited with the same source of laser excitation as the room temperature measurement. Concentrating initially on the shape of the three samples, different power dependence was observed. The PL peak was shifted into the higher energy level (shorter wavelength) compared with the room temperature measurements, as expected. But the linewidth and shape of the PL spectra for three samples were not strongly sensitive to the measurement temperature. In particular, they are almost the same as those obtained from the room temperature measurements. The broadening behavior of the PL spectra originally came from the size fluctuation of QDs on the samples. For sample A, the inter-dot coupling between the aligned QDs is not strong. There is no inter-dot carrier transport between one dot and another. Carriers are only captured and recombine in the QDs which give rise to the photoluminescence. Because of the random carrier capturing and recombination process, all the QDs contribute equally to the PL. When the ground states are fully occupied, the emission from the first excited state occurs [97]. This behavior was clearly observed in room and low-temperature measurements of the Sample A when the excitation power was increased.

As can be seen from Fig. 5.18 and 5.21, almost no change in the emission peak energy for Sample A and C occur. Distinct blue shift and broadening to the higher energy side for Sample B were observed when the laser excitation power was increased in room-temperature and low-temperature measurements as shown in Fig. 5.23 and Fig. 5.24. A possible reason is that optical transition with higher energy levels takes part in this peak shift. Dot size inhomogeneity means there are many sizes of QDs along the chain. At low excitation power, the photoexcited carriers are distributed in the barrier and try to find the lowest energy minimum (which is in larger QDs), recombine there, and emit photoluminescence. When the excitation power is increased, larger quantum dots are filled with carriers. This situation prevents the transferring of carriers from smaller to larger dots, and luminescence from the smaller QDs starts to appear. The whole emission came from all QDs and, as a result, PL

emission with shift to the higher energy (blue shift) and broadening in the higher energy side was observed [98].

The PL peak for Sample C which was observed at the lower energy side both at room temperature and at low temperature (4 K) reveals that not only the larger dot size but also the coupling effect involve in this peak shift compared with the other two samples. Due to interaction of closely packed QDs in the alignment, the ground state energy levels split into bonding and anti-bonding states. The PL emission may come from the ground bonding state [99]. This effect probably caused Sample C to radiate luminescence at a lower energy compared with Sample A and B. However, the population of the lower-energy dots and higher-energy dots are probably not much different, and so the blue shift could not be seen clearly at the low temperature. But for room-temperature measurement, a slight shift to the higher energy side and a broadening behavior could be seen. Therefore, coupling effect in Sample C was not obvious from the excitation-power-dependent PL measurement. The linewidth of 58 meV and the peak shift to the lower energy side for Sample C reveals that the average dot size is larger and more homogeneous compared with Sample B.

5.2.3.5 Polarization-Resolved PL Measurements of Linearly Aligned QDs

The polarization-resolved PL spectra at room temperature and low temperature were measured for the three samples. The results are shown in Fig. 5.26. At RT, the PD of the Sample A was 12%. The anisotropy was almost constant over the QD region (around 1.1 eV), indicating that the QDs in the Sample A have uniform shape, homogeneous size and constant strain distributions. At 4K, the PD was almost 14%. The results for the room temperature and 4 K measurement are not much different, which is within the error of the setup. Polarization property of Sample A does not depend on the measurement temperature, and thus PD for this sample may come from intrinsic (size and shape) properties of QDs.

For Sample B and C, the PD at room increased to about 15% which was probably caused by the longer alignment and the shape anisotropy of QDs. The PD was not constant throughout the whole energy spectrum, however. It decreased into the higher energy side because of the size fluctuation of the QDs on the sample. Larger quantum dots with lower energy levels exhibit higher polarization degrees.